Measurement of Exclusive J/ψ Electroproduction in High-Energy ep Collisions at HERA

Tetsuo Abe

Department of Physics, University of Tokyo
7-3-1 Hongo, Bunkyo-ku, Tokyo 113-8654, Japan

Revised version 1.0

A thesis submitted in partial fulfillment
of the requirements
for the doctoral degree of science

March 30, 2001

Abstract

Exclusive electroproduction of J/ψ mesons in ep collisions, $ep \to eJ/\psi\, p$, at $\sqrt{s} \sim 310\,\mathrm{GeV}$ has been studied with the ZEUS detector using an integrated luminosity of $90\,\mathrm{pb}^{-1}$. The J/ψ state is identified via its dilepton decay channels ($J/\psi \to e^+e^-$, $\mu^+\mu^-$). The exclusive $\gamma^* p$ total cross section, $\sigma_{tot}^{\gamma^* p \to J/\psi\, p}$, has been measured as functions of Q^2 and W. The helicity state of J/ψ mesons has also been measured from the angular distribution of the decay leptons, and the ratio of $R = \sigma_L/\sigma_T$ is extracted as a function of Q^2. These results are compared with the theoretical predictions from the Regge phenomenology and from the perturbative QCD.

Contents

Chapter 1

Introduction

Many historic discoveries have been made in scattering experiments where a particle collides on other particle(s). Experimentalists investigate structure of matters and nature of interactions by measuring energies, angles, types and multiplicity of particles produced in the final state of the interaction. Much knowledge was accumulated, starting from the first example of the Rutherford scattering to the recent collider experiments. Those results have been essential inputs for the foundation of *the Standard Model* (SM) in particle physics. It includes six types of quarks and of leptons as fundamental particles, and four gauge bosons as vehicles of the electromagnetic, weak and strong interactions. The description of these interactions is based on the quantum field theory and the gauge principle. No phenomena which are inconsistent with the SM have been observed so far.

When the coupling constant of the interaction is small, theoretical predictions can be made based on the perturbative method. This is the case for the electromagnetic and weak interactions, where cross sections are calculated with small uncertainties. Those predictions have been verified precisely in a huge number of experimental measurements, for example, in e^+e^- collisions with a leptonic final state.

A different situation is seen on the strong interaction. Although it is described based on the quantum chromodynamics (QCD), perturbative calculations give large uncertainties due to its large coupling constant. Physics processes studied with the perturbative QCD (pQCD) are mostly accompanied by non-perturbative subprocesses, like hadronization, which lead to both theoretical and experimental uncertainties.

Soft hadron-hadron collisions cannot be calculated with the pQCD. They have

been, however, successfully described with the Regge phenomenology in a non-perturbative approach. The photon-proton interaction (photoproduction) is also regarded as such kind of process from the vector-meson dominance [1]. The center-of-mass energy dependences of the total cross section for hadron-hadron and photon-hadron collisions at high energies have been comprehensively understood with the soft Pomeron exchange over a wide energy range from the fixed-target to the collider experiments.

Experiments at the electron-proton collider HERA have provided cross-section measurements on the photoproductions of the neutral light vector mesons, $\gamma p \to Vp$ where $V = \rho, \omega$ or ϕ, at sufficiently high energies compared with those meson masses. The measured energy dependences showed a common slow-rising behavior among the light vector mesons, and are also explained with the soft Pomeron exchange.

Results with an impact have appeared in the measurement of J/ψ photoproduction at HERA [2]. The cross section rises more rapidly with energy. Similarly, a steep rising-behavior has been observed in exclusive electroproduction of ρ^0 mesons [3, 4], where the process is treated as a scattering between the virtual photon and the proton: $\gamma^* p \to \rho^0 p$. The energy dependence becomes steeper as the photon virtuality increases. Those two phenomena are inconsistent with the soft production mechanism, and show signs of a hard process though quark-partons are confined in a shell of the hadron state.

In this thesis, exclusive electroproduction of J/ψ mesons, $ep \to eJ/\psi\, p$, is studied. This process is regarded as a more fundamental process of $\gamma^* p \to J/\psi\, p$. The J/ψ state is identified via its dilepton decay channels ($J/\psi \to e^+e^-$, $\mu^+\mu^-$). This study is an extension of J/ψ photoproduction [2] to the higher photon virtuality. Cross sections are measured as a function of not only energy but also the photon virtuality. The virtuality and/or the mass of the J/ψ can be used in perturbative calculations as a hard scale. The results of this study are compared with the pQCD-based predictions as well as the phenomenological model based on the Regge theory and the vector-meson dominance. Those two different approaches show significantly different energy and photon-virtuality dependences of the cross section. This measurement provides an interplay between soft and hard physics, and a new and unique object for the QCD study with a clean signal of the leptonic final state.

The organization of this thesis is as follows. In the chapter 2, the formalism to

describe the neutral-current ep scattering is reviewed. In the chapter 3, theoretical aspects on exclusive production of neutral vector mesons are explained. The experimental apparatus on the HERA collider and the ZEUS detector is described in the chapter 4. In the chapter 5, descriptions on the tools in the Monte Carlo method are given. In the chapter 6, event characteristics of the signal J/ψ events at the detector level and reconstruction methods of the kinematical variables are explained. The event samples are selected in the chapter 7. From those samples, cross sections are calculated with the method described in the chapter 8, and the final results and discussions are shown in the chapter 9. At last the summary and conclusions are presented in the chapter 10.

Chapter 2

Neutral-current ep Scattering and the $\gamma^* p$ Total Cross Section

2.1 Kinematical Variables

The general diagram for the neutral-current ep[1] scattering in the one-photon exchange approximation is shown in Figure 2.1. The Lorentz invariants used to describe this kinematics are

- $\sqrt{s} = \sqrt{(k+P)^2}$: the center-of-mass energy of the ep system,
- $Q^2 = -(k-k')^2$: the negative four-momentum transfer squared at the electron[2] vertex, or virtuality of the exchanged virtual photon (γ^*), and
- $W = \sqrt{(k-k'+P)^2}$: the center-of-mass energy of the $\gamma^* p$ system,

where $k = (k_0, \vec{k})$ and $k' = (k'_0, \vec{k'})$ are four-momenta of the initial and final electron, respectively. $P = (P_0, \vec{P})$ is a four-momentum of the incoming proton. X in Figure 2.1 represents any hadronic final state.

2.2 Cross-section Formulae

The differential cross section of the process, $ep \to eX$, is expressed as the contraction between the lepton tensor, $L_{\mu\nu}$, and the hadron tensor, $W_{\mu\nu}$,

$$d\sigma^{ep} = \frac{1}{2(s-M_p^2)} \left\{ \left(\frac{e}{Q^2}\right)^2 L^{\mu\nu} \right\} \left\{ \left(4\pi e_p^2 M_p\right) W_{\mu\nu} \right\} d\Gamma, \qquad (2.1)$$

[1]The symbol '*ep*' represents electron-proton ($e^- p$) or positron-proton ($e^+ p$) in this thesis.
[2]The word '*electron*' represents electron (e^-) or positron (e^+) in this thesis.

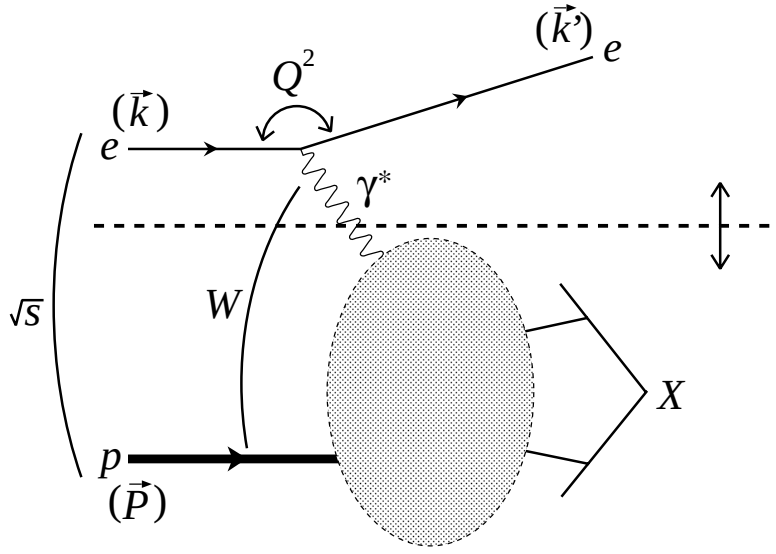

Figure 2.1: *A general diagram for the neutral-current ep scattering in the one-photon exchange approximation. X represents any hadronic final state.*

where e and e_p are electric charges of the electron and the proton, respectively, M_p is a mass of the proton, and $d\Gamma$ is a Lorentz invariant phase space. Since the electron is point-like at least in the kinematical region of this analysis, the lepton tensor is calculable with the quantum electrodynamics (QED) as

$$L_{\mu\nu} = 2\left[k'_\mu k_\nu + k'_\nu k_\mu - g_{\mu\nu}\frac{Q^2}{2}\right] \tag{2.2}$$

for unpolarized electron beams. On the other hand, the proton has a structure, so that the exact form of the hadron tensor is not known. It could be, however, parameterized in the following form on the assumption of the parity and current conservation,

$$\begin{aligned} W_{\mu\nu} = \quad & W_1\left(-g_{\mu\nu} - \frac{q_\mu q_\nu}{Q^2}\right) \\ + \quad & W_2\frac{1}{M_p^2}\left(P_\mu + \frac{P\cdot q}{Q^2}q_\mu\right)\left(P_\nu + \frac{P\cdot q}{Q^2}q_\nu\right), \end{aligned} \tag{2.3}$$

where $q_\mu = k_\mu - k'_\mu$ is a four-momentum of the virtual photon, and W_1, W_2 are functions of Q^2 and W and called *the electromagnetic proton structure functions*. The structure inside the shaded ellipse in Figure 2.1 is embodied in the functional forms of W_1 and W_2. From Eqs. (2.1), (2.2) and (2.3), the formula for the inclusive

ep cross section is written as

$$\begin{aligned}\frac{d^2\sigma^{ep}}{dxdQ^2} &= \frac{4\pi\alpha^2_{QED}}{xQ^4}\left[xy^2M_pW_1(x,Q^2)+\left\{(1-y)+\frac{xyM_p^2}{s}\right\}\frac{Q^2}{2xM_p}W_2(x,Q^2)\right] \\ &= \frac{4\pi\alpha^2_{QED}}{xQ^4}\left[xy^2F_1(x,Q^2)+\left\{(1-y)+\frac{xyM_p^2}{s}\right\}F_2(x,Q^2)\right], \qquad (2.4)\end{aligned}$$

where α_{QED} is the fine structure constant, x is so-called *the Bjorken scaling variable* defined as $x = Q^2/(2P\cdot q)$, y is so-called *the inelasticity of the lepton* defined as $y = (P\cdot q)/(P\cdot k)$, and F_1, F_2 are more commonly used structure functions defined as

$$F_1 = M_pW_1 \quad \text{and} \qquad (2.5)$$

$$F_2 = \frac{Q^2}{2xM_p}W_2. \qquad (2.6)$$

The formula for the ep cross section can be expressed also in terms of the transverse and longitudinal total cross sections defined as

$$\sigma_T^{\gamma^* p} = \sum_{\lambda=\pm1}\frac{4\pi^2\alpha_{QED}}{K}\varepsilon_\lambda^{\mu*}\varepsilon_\lambda^{\nu}W_{\mu\nu} \quad \text{and} \qquad (2.7)$$

$$\sigma_L^{\gamma^* p} = \frac{4\pi^2\alpha_{QED}}{K}\varepsilon_0^{\mu*}\varepsilon_0^{\nu}W_{\mu\nu}, \qquad (2.8)$$

respectively. In the above, ε_λ^μ is a polarization vector of the virtual photon indicating the helicity state λ, and K is chosen as $K = (W^2-M_p^2)/(2M_p)$ according to the Hand's convention to define the flux of the virtual photon. The differential cross section on Q^2 and y takes the following form,

$$\frac{d^2\sigma^{ep}}{dQ^2dy} = \Gamma_{\rm T}\cdot\sigma_T^{\gamma^* p} + \Gamma_{\rm L}\cdot\sigma_L^{\gamma^* p}, \qquad (2.9)$$

where $\Gamma_{\rm T}$ and $\Gamma_{\rm L}$ are the transverse and longitudinal photon fluxes, respectively. Those are defined as

$$\Gamma_{\rm T}(Q^2,y) = \frac{\alpha_{QED}}{2\pi Q^2}\frac{1}{y}\left[1+(1-y)^2-2(1-y)\frac{Q^2_{min}}{Q^2}\right] \qquad (2.10)$$

$$\text{where} \quad Q^2_{min} = m_e^2\frac{y^2}{1-y} \quad \text{and} \qquad (2.11)$$

$$\Gamma_{\rm L}(Q^2,y) = \frac{\alpha_{QED}}{2\pi Q^2}\frac{2(1-y)}{y}. \qquad (2.12)$$

In the above, m_e is the mass of the electron, and Q^2_{min} is a minimum value for Q^2. The formula (2.9) corresponds to a physical picture of a scattering between the virtual photon and the proton weighted by the photon flux separately on the transverse and longitudinal component. Introducing the inclusive $\gamma^* p$ total cross section, $\sigma^{\gamma^* p}_{TOT}$, defined as

$$\sigma^{\gamma^* p}_{TOT} = \sigma^{\gamma^* p}_T + \sigma^{\gamma^* p}_L, \tag{2.13}$$

the differential cross section is given in terms of $\sigma^{\gamma^* p}_{TOT}$ as

$$\frac{d^2\sigma^{ep}}{dQ^2 dy} = \Gamma_{\rm T} \cdot \left(\frac{1 + \epsilon\, R}{1 + R} \right) \cdot \sigma^{\gamma^* p}_{TOT}, \tag{2.14}$$

where R is a ratio of the longitudinal to transverse total cross section, and ϵ is a ratio of the longitudinal to transverse photon flux:

$$R = \frac{\sigma^{\gamma^* p}_L}{\sigma^{\gamma^* p}_T}, \tag{2.15}$$

$$\epsilon = \frac{\Gamma_{\rm L}}{\Gamma_{\rm T}}. \tag{2.16}$$

The above formula (2.14) holds also for exclusive processes, and is commonly used in studies of vector meson production:

$$\frac{d^2\sigma^{ep}}{dQ^2 dy} = \Gamma_{\rm T} \cdot \left(\frac{1 + \epsilon\, R}{1 + R} \right) \cdot \sigma^{\gamma^* p \to Vp}_{tot}, \tag{2.17}$$

where $\sigma^{\gamma^* p \to Vp}_{tot}$ indicates the exclusive $\gamma^* p$ total cross section, meaning the total production cross section of the vector meson V.

Chapter 3

Exclusive Production of Vector Mesons

In this chapter, theoretical aspects are presented on exclusive production of neutral vector mesons: $ep \to eVp$ where V is mainly the ρ, ω, ϕ, J/ψ or Υ. The general diagram is shown in Figure 3.1. The exclusive hadronic final state consists of the vector meson and the proton, which corresponds to X in the inclusive process: $ep \to eX$ (Figure 2.1). There is an additional Lorentz invariant variable, t, which is defined as a four-momentum transfer squared at the proton vertex.

In the following sections, two major classes of theoretical models are explained. One of them is a phenomenological model based on the vector-meson dominance and the Regge theory. The other model is based on the perturbative QCD. A formalism to describe the J/ψ decay is also explained for the helicity study. In the last section, the aim of this thesis is presented.

3.1 Model Based on the Vector-meson Dominance and the Regge Theory

3.1.1 The vector-meson dominance model

The physical photon, $\left|\gamma\right\rangle$, has hadronic components, $\left|h\right\rangle$, due to the quantum fluctuation,

$$\left|\gamma\right\rangle \;=\; \sqrt{Z_3}\left|\gamma_B\right\rangle + \sum_h \left|h\right\rangle, \tag{3.1}$$

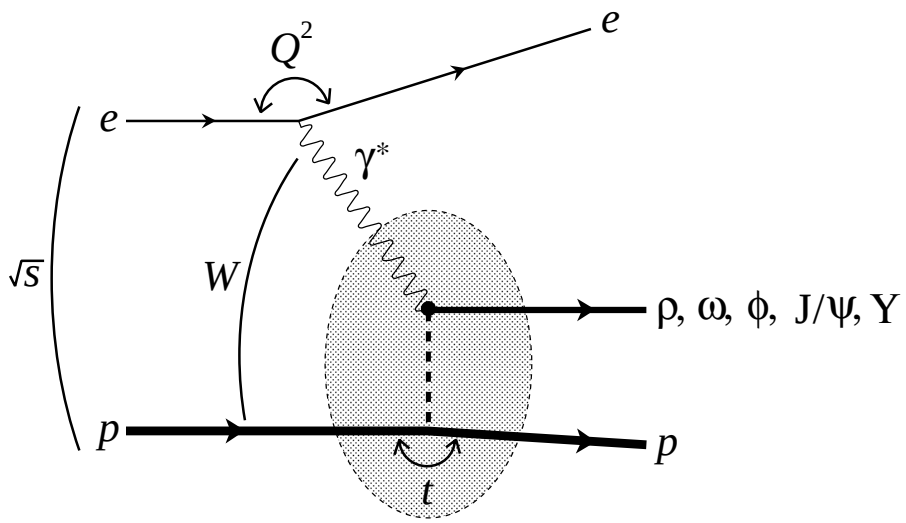

Figure 3.1: *A general diagram for exclusive production of vector mesons in the one-photon exchange approximation. Vector mesons are mainly ρ, ω, ϕ, J/ψ and Υ.*

where Z_3 is a normalization factor, $\left|\gamma_B\right\rangle$ indicates a bare photon, and the sum $\sum_h$ is done over all the possible hadronic states. In the Vector-meson Dominance Model (VDM) [1], it is assumed that only the components of the light vector mesons, which have the same internal quantum numbers as those of the photon, contribute to the reaction:

$$\left|\gamma\right\rangle \;=\; \sum_{V=\rho,\omega,\phi} \left(\frac{e M_V^2}{f_V}\right)\left(\frac{1}{Q^2+M_V^2}\right)\left|V\right\rangle, \tag{3.2}$$

where f_V is the coupling constant of the photon to the vector meson, M_V is the mass of the vector meson, and $\left|V\right\rangle$ denotes the vector-meson state. The factor of $1/(Q^2+M_V^2)$ indicates the propagator of the intermediate vector meson. If the summation is extended to the heavy mesons, $\sum_{V=\rho,\omega,\phi,J/\psi,\Upsilon}$, this model is called the Generalized Vector-meson Dominance Model (GVDM) [5]. In this thesis, GVDM is referred as VDM.

In the framework of the VDM, exclusive production of vector mesons is regarded as a more fundamental process of an elastic scattering between the vector meson and the proton, as shown in Figure 3.2. Therefore, the transverse and longitudinal

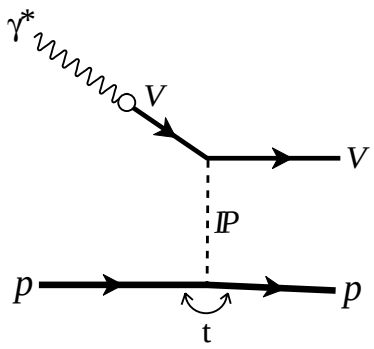

Figure 3.2: *A diagram for exclusive production of the vector meson V, based on the VDM and the Regge theory. IP indicates a Pomeron trajectory.*

cross sections are written as

$$\sigma_T^{\gamma^* p\to Vp}(Q^2,W) = \left(\frac{eM_V^2}{f_V}\right)^2\left(\frac{1}{Q^2+M_V^2}\right)^2\sigma_T^{Vp\to Vp}(W) \quad \text{and} \tag{3.3}$$

$$\sigma_L^{\gamma^* p\to Vp}(Q^2,W) = \left(\frac{eM_V^2}{f_V}\right)^2\left(\frac{1}{Q^2+M_V^2}\right)^2\left(\frac{Q^2}{M_V^2}\right)\sigma_L^{Vp\to Vp}(W), \tag{3.4}$$

where $\sigma_T^{Vp\to Vp}$ and $\sigma_L^{Vp\to Vp}$ are the elastic cross sections of a scattering between the proton and the transversely or longitudinally polarized vector meson, respectively. The VDM, therefore, gives the Q^2-dependence of the cross section, $\sigma_{tot}^{\gamma^* p\to Vp}(Q^2)$. However, an additional model is needed to describe the W-dependence. The ratio of the longitudinal to transverse cross section is written as

$$R = \frac{\sigma_L^{\gamma^* p\to Vp}}{\sigma_T^{\gamma^* p\to Vp}} = \xi(W)\cdot\frac{Q^2}{M_V^2}, \tag{3.5}$$

where the parameter ξ is defined as $\xi = \sigma_L^{Vp\to Vp}/\sigma_T^{Vp\to Vp}$.

3.1.2 The Regge theory

The Regge theory is a model to describe elastic scatterings in the non-perturbative method (for example see [6].). This theory considers a two-particle collision process: $A + B \to C + D$, as shown in Figure 3.3-(a). The scattering amplitude contains a sum of propagators from all the possible resonance particles which are exchanged in the t-channel, as seen in Figure 3.3-(b). Those particles were found to show a linear correlation between the mass squared and the spin as seen in Figure 3.4 (Chew-Frautschi plot), where the linearity is reflected by the field theory. The continuous

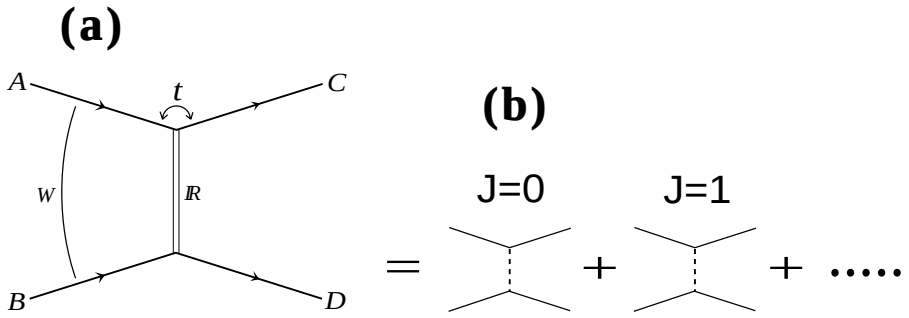

Figure 3.3: *Diagrams of the process:* $A + B \to C + D$. *(a) A scattering with a Regge trajectory* $I\!R$. *(b) Exchanges of resonance particles with spin* $J = 1, 2, \cdots$. *This summation corresponds to the expansion with respect to the t-channel partial wave series.*

line in Figure 3.4 which parameterizes the correlation is called *a Regge trajectory*. In the Regge theory, a size of spin J is regarded as a complex number, and the sum of the propagators from the resonance particles are replaced by the integration around the corresponding Regge pole, $1/(\alpha(t) - J)$, over the complex angular momentum space. The physics information in the scattering, therefore, is expressed in terms of the functional form of the corresponding Regge trajectory.

The Regge theory predicts, in the high energy limit of $W^2 \gg |t|$,

$$A(W,t) \;=\; f(t) \cdot W^{2\alpha(t)}, \tag{3.6}$$

where A indicates a scattering amplitude, $f(t)$ represents a certain function of t, and $\alpha(t)$ is a corresponding Regge trajectory. Thus, the elastic cross section takes the following form,

$$\frac{d\sigma^{Vp\to Vp}}{d|t|} \;\cong\; \frac{1}{W^4}|A(W,t)|^2 \tag{3.7}$$

$$\propto\; F(t) \cdot \left(\frac{W}{W_0}\right)^{4(\alpha(t)-1)}, \tag{3.8}$$

where W_0 is a constant with around 1 GeV in the hadron mass scale. Using an exponential fall nature on $|t|$ and a linear form of $\alpha(t) = \alpha(0) + \alpha' t$, the cross section is written as

$$\frac{d\sigma^{Vp\to Vp}}{d|t|} \;\propto\; e^{-b_0|t|}\left(\frac{W}{W_0}\right)^{4(\alpha(t)-1)}$$

$$=\; e^{-b|t|}\left(\frac{W}{W_0}\right)^{4(\alpha(0)-1)}, \tag{3.9}$$

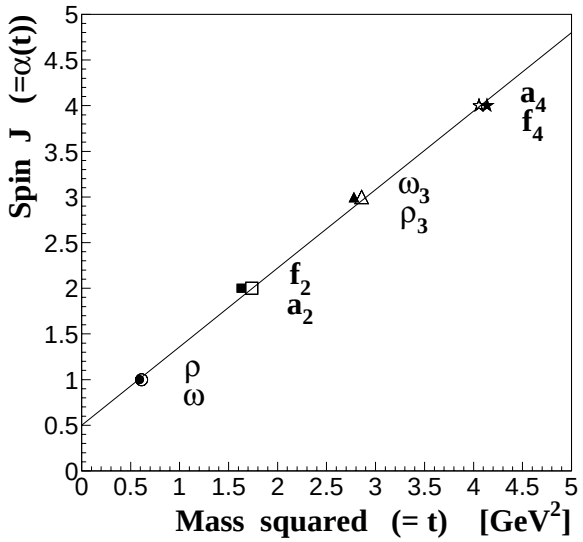

Figure 3.4: *An example of the Chew-Frautschi plot and the Regge trajectory (solid line).*

where b is the W-dependent slope parameter defined as

$$b = b_0 + 4\alpha' \ln\left(\frac{W}{W_0}\right). \tag{3.10}$$

Integrating over t, the total elastic cross section is calculated as

$$\sigma^{Vp\to Vp}(W) \;\propto\; \frac{W^{4(\alpha(0)-1)}}{b}, \tag{3.11}$$

which leads to the effective power for the W-dependence $\left(\sigma \propto W^{\delta}\right)$,

$$\delta \;\cong\; 4\left(\alpha(0) - \frac{\alpha'}{b} - 1\right). \tag{3.12}$$

The total cross section can be derived using the optical theorem,

$$\begin{aligned} \sigma^{Vp}_{TOT}(W) \;&\sim\; \frac{1}{W^2}\,\Im\big\{A(W, t=0)\big\} \\ &\propto\; W^{2(\alpha(0)-1)}. \end{aligned} \tag{3.13}$$

3.1.3 Phenomenology with the soft Pomeron exchange

All the known meson trajectories have an intercept $\alpha(0)$ less than one, so that the hadron-hadron total cross section should decrease as W increases according to the formula (3.13). However, the observed cross section showed a slow rise at

$W > 10\,\mathrm{GeV}$ as seen in Figure 3.5. This fact motivated introducing a hypothetical trajectory with an intercept $\alpha(0)$ larger than one, which is called *a Pomeron trajectory* ($\alpha_{IP}(t) = \alpha_{IP}(0) + \alpha'_{IP}\, t$). Donnachie and Landshoff [7] fitted the experimental data on the total cross section of hadron-hadron scatterings with the cross section form of

$$\sigma_{TOT}(W) \;=\; X \cdot W^{2\epsilon} \,+\, Y \cdot W^{-2\eta}. \tag{3.14}$$

The first term corresponds to the Pomeron exchange which is dominant at high W. The second term corresponds to the Reggeon exchange. The resulting values of the fit are $\epsilon = 0.0808$ and $\eta = 0.4525$. The corresponding Pomeron intercept is $\alpha_{IP}(0) = 1.08$. They also obtained, from elastic scattering data, a value of $\alpha'_{IP} = 0.25\ \mathrm{GeV}^{-2}$. The Pomeron with these values is called *the soft Pomeron*. The total photoproduction cross sections around $W \sim 200\,\mathrm{GeV}$ measured at HERA are consistent with the Regge prediction with the soft Pomeron exchange [8, 9].

The W-dependence, or energy dependence, of the cross section for exclusive photoproduction of light vector mesons is predicted with the soft Pomeron exchange using the formula (3.12),

$$\delta \;\cong\; 4\left(1.08 - \frac{0.25}{b} - 1\right) \;=\; 0.22, \tag{3.15}$$

where the typical value is used for the t-slope: $b = 10\,\mathrm{GeV}^{-2}$. This prediction is successful for all the light vector mesons as seen in Figure 3.5.

3.2 Models Based on the Perturbative QCD

The perturbative QCD (pQCD) is applicable for exclusive production of vector mesons when a hard scale is available. The basic ideas are

- an exchange of the two-gluon system in a color-singlet state, corresponding to a Pomeron exchange in the Regge theory, and
- the QCD factorization, illustrated in Figure 3.6. An amplitude of the process: $\gamma^* p \to Vp$ is factorized into the three parts related to the gluon density in the proton, the vector-meson state and the hard matrix elements.

The lowest-order Feynman diagrams of the gauge invariant set are shown in Figure 3.7. At high W like at HERA, the splitting of the virtual photon into the color dipole ($q\bar{q}$) occurs much before the interaction of the dipole with the proton,

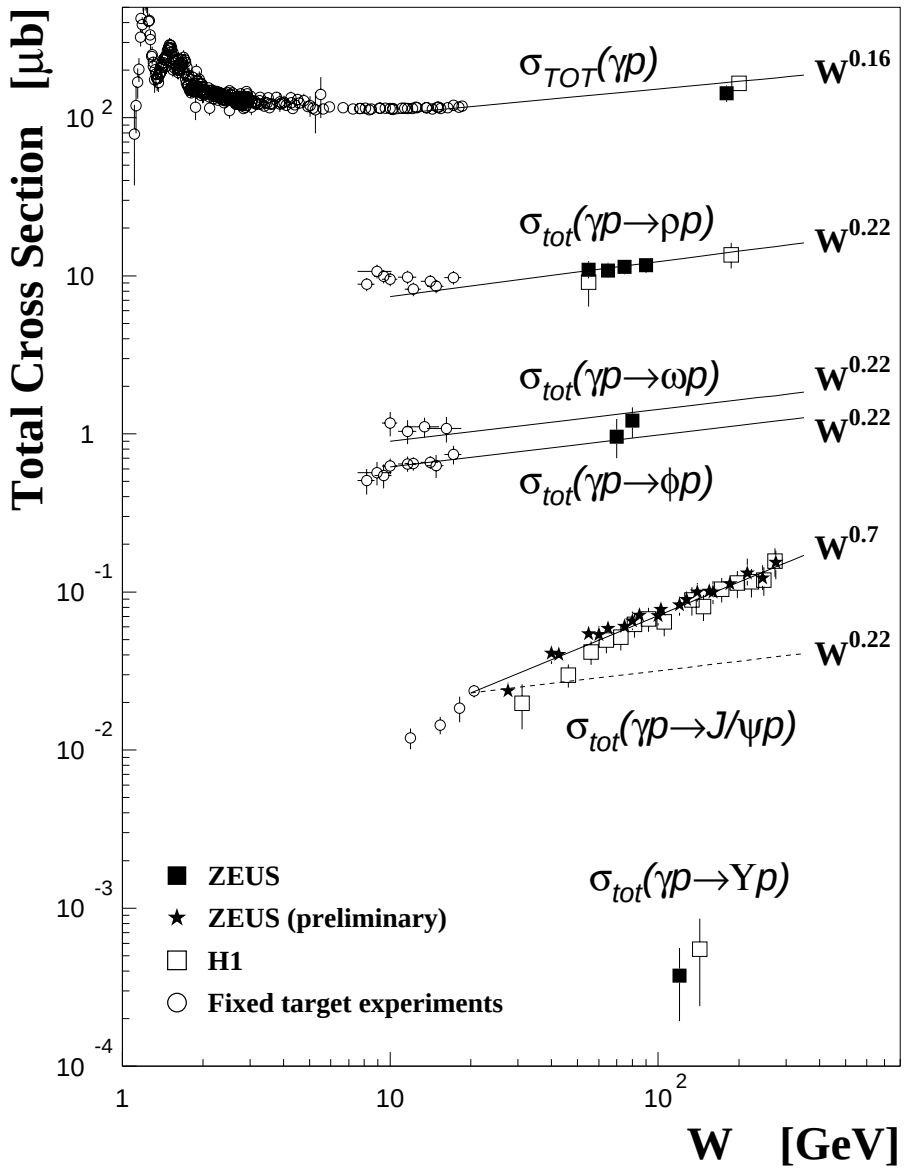

Figure 3.5: *The W-dependences of the inclusive (top) and exclusive (below the top) total cross sections in photoproduction.*

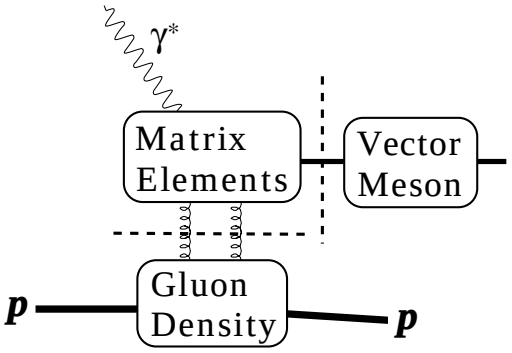

Figure 3.6: *The QCD factorization for vector meson production*

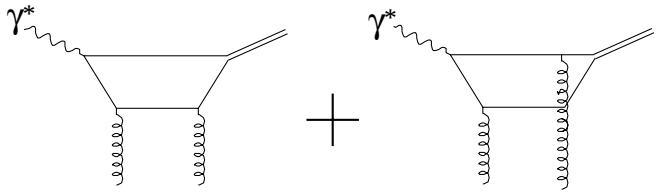

Figure 3.7: *The lowest-order Feynman diagrams for vector meson production in the pQCD*

and the vector meson state is formed long after the interaction in the proton rest frame. In other words, the scattering occurs for a much shorter time-scale than that of the whole process of $\gamma^* p \to Vp$. The pQCD-based description of vector-meson production indicates a high sensitivity of the process to the gluon density in the proton.

The pQCD-based models predict steeper Q^2-dependences: $\sigma_T^{\gamma^* p \to Vp}(Q^2) \sim Q^{-6}$ and $\sigma_L^{\gamma^* p \to Vp}(Q^2) \sim Q^{-4}$ than those from the VDM: $\sigma_T^{\gamma^* p \to Vp}(Q^2) \sim Q^{-4}$ and $\sigma_L^{\gamma^* p \to Vp}(Q^2) \sim Q^{-2}$ (Eq.(3.3), (3.4)). On the W-dependence, larger δ values are predicted: $\delta \simeq 0.8$-1.0 than that from the Regge phenomenology with the soft Pomeron exchange: $\delta \cong 0.22$ (Eq.(3.15)).

On the naive assumption in the pQCD, the cross section is proportional to the square of the gluon density in the proton: $\sigma_{tot}^{\gamma^* p \to Vp} \propto \left[\bar{x} g(\bar{x}, \mu^2)\right]^2$, where $\bar{x}$ is an average momentum fraction among the two gluons and μ is a QCD scale. In the Ryskin model [10], those variables are expressed as

$$\bar{x} = \frac{Q^2 + M_V^2 + |t|}{W^2} \quad \text{and} \tag{3.16}$$

$$\mu^2 = \frac{Q^2 + M_V^2 + |t|}{4}. \tag{3.17}$$

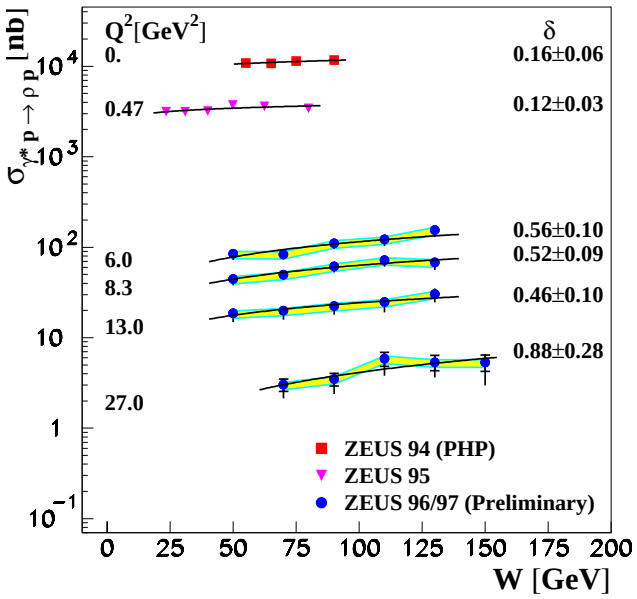

Figure 3.8: *W-dependence of the cross section for ρ^0 electroproduction at different Q^2 values, extracted from [4].*

Due to the facts that $\bar{x}$ is inversely proportional to W^2 : $\bar{x} \propto 1/W^2$ and that the F_2 measurements at HERA showed a steep rise of the gluon density toward low x, the vector meson cross section is expected to show a steep W-dependence. Since the gluon density shows a steeper rise toward low x as Q^2 increases, the W-slope of the vector meson cross sections is expected to be steeper as Q^2 increases, i.e., a Q^2-dependence of δ is expected: $\delta(Q^2)$. Such kind of phenomenon has been observed in exclusive ρ^0 electroproduction at HERA [4], as seen in Figure 3.8.

The pQCD-based calculations have the following uncertainties.

- **QCD scale**

  There are three Lorentz invariants which can be a candidate for the QCD scale: Q^2, M_V^2 and t. The QCD scale is expressed as functions of those variables : $\mu = f(Q^2, M_V^2, t)$. Ryskin proposed the scale as in Eq.(3.17). There are other possibilities in the choice of the scale.

- **NLO corrections**

  Some next-to-leading order (NLO) corrections are taken into account [11, 12]. However, the full corrections have not yet been calculated so far. Those unknown NLO corrections are expected to have an influence mainly on the normalization of the cross section as a $\mathcal{K}$-factor.

- **Vector meson modeling**
  Modeling the vector meson state was found to have a non-negligible influence on the W- and/or Q^2-dependence of the cross section.

Many calculations have been done by various authors. Here only the two major calculations (the FKS and MRT calculations), which are referred in this thesis, are explained below. On other calculations, for example see [13]. The main difference between the following two calculations is on the model to deal with the vector meson state. Some higher-order QCD corrections are also different.

3.2.1 The FKS calculation

Frankfurt, Koepf and Strikman (FKS) calculated the exclusive photo- and electroproduction cross sections of the J/ψ and Υ using the light-cone wave function for the vector meson state convoluted with the amplitude of the hard process [14]. The wave function is based on the non-relativistic potential model. The effects of the small transverse $q\bar{q}$ distance and the large transverse momentum are taken into account. The basic formula was deduced by S.J. Brodsky et al. [15]. The calculation of the transverse cross section using the wave function approach encounters an infrared divergence in the integration over the quark transverse momentum. Instead, the ratio of the longitudinal to transverse cross section, $R = \sigma_L/\sigma_T$, was constructed according to the QCD-inspired consideration.

The following corrections beyond the leading-log calculation are taken into account:

- The real part of the amplitude;
- The leading twist correction;
- Some NLO corrections are estimated with *the rescaling of hard process* [16]. The rescaled Q^2, which is used in the calculation of the strong coupling constant and of the gluon density, is significantly larger than that in the MRT calculation (Eq.(3.17)); and
- The correction for the Fermi motion of quarks in the produced vector meson.

3.2.2 The MRT calculation

Martin, Ryskin and Teubner (MRT) calculated the exclusive electroproduction of ρ^0 and J/ψ mesons [17, 18], where the parton-hadron duality [18] is used instead of the wave function to describe the vector meson state. The hard process is calculated

as an open $q\bar{q}$ production, and then the $q\bar{q}$ state is projected onto the vector meson state with $J = 1^-$ in the $q\bar{q}$ rest frame using the parton-hadron duality. The parton-hadron duality approach leads to the following two major benefits. One is that the approach provides a common mechanism for the description of all the vector meson production processes. The second one is that the infrared problem in the integration over the quark transverse momentum can be overcome, so that the convergent calculation is available also for the transverse cross section. The MRT prediction for R is expected to be different from the naive pQCD expectation, $R = Q^2/M_V^2$, and has the following form,

$$\frac{\sigma_L}{\sigma_T} = \frac{Q^2}{M_V^2}\left(\frac{\gamma}{\gamma+1}\right)^2, \tag{3.18}$$

where γ is the effective anomalous dimension of the gluon density.

The following corrections beyond the leading-log calculation are taken into account:

- The gluon-k_T is included using the gluon density unintegrated over k_T which satisfies the Balitskii-Fadin-Kuraev-Lipatov (BFKL) equation [19];
- The effects of the off-diagonal elements of the gluon density are included (*the skewed gluon density*). The gluon distribution becomes more skewed with increasing Q^2 and with a larger mass of the vector meson. The cross section is enhanced about 70 % in case of the J/ψ at a large Q^2 value ($\sim 50\,\mathrm{GeV}^2$);
- The $\mathcal{K}$-factor from some NLO corrections is estimated [12];
- The real part of the amplitude is taken into account using the dispersion relation. The cross section is enhanced about 20 % in case of the J/ψ. A larger effect appears at a larger Q^2 value.

3.2.3 Effects of different models

Figure 3.9-(a) and (b) show effects of the higher-order QCD corrections, which are implemented in the FKS calculation, on the W-slope parameter δ ($\sigma \propto W^\delta$), and on the Q^2-dependence normalized to the photoproduction cross section, respectively. Only the Q^2 rescaling has a sizable effect on the W-slope, on the other hand, the Fermi motion correction is significant for the Q^2-dependence. Figure 3.9-(c) and (d) show effects of the different potential functions for the J/ψ in the FKS calculation. No difference is seen both on the W- and Q^2-dependences. Figure 3.9-(e) and (f) show effects of the different gluon density parameterizations. The recent

parameterizations are used in the MRT calculation: CTEQ5M [20], GRV98HO [21] and MRST99 [22]. No difference is seen on the Q^2-dependence. There is a small difference between GRV98HO and CTEQ5M/MRST99 by $\Delta\delta \sim 0.2$ on the W-dependence. The difference between CTEQ5M and MRST99 is negligible in the kinematical region of this analysis.

3.3 Description of the J/ψ Decay

A formalism in the one-photon exchange approximation to study the polarization of produced vector mesons was developed [23]. In this section, the formulae for unpolarized lepton beams are reviewed.

Three planes are defined in the $\gamma^* p$ center-of-mass frame as shown in Figure 3.10-(a):

- a plane including the incoming and scattered electron, called *the scattering plane*,
- a plane including the virtual photon and the produced J/ψ meson, called *the production plane*, and
- a plane including the decay dilepton, called *the decay plane*.

An angle Φ is defined, in the $\gamma^* p$ center-of-mass frame, as an angle between the scattering and production plane. An angle ϕ_h is defined, also in the $\gamma^* p$ center-of-mass frame, as an angle between the decay and production plane. An angle θ_h is defined, in the J/ψ rest frame, as an angle between the positively-charged decay lepton and the negative direction of the scattered proton, as shown in Figure 3.10-(b). The negative direction of the scattered proton in the J/ψ rest frame corresponds to the direction of the J/ψ meson in the $\gamma^* p$ center-of-mass frame, and is used as a quantization axis.

The decay angular distribution, W_d, is expressed in the following form,

$$W_d(\cos\theta_h, \phi_h, \Phi) \;\propto\; \sum_{\lambda,\lambda'} D_\lambda(\cos\theta_h, \phi_h)^* \; \rho_{\lambda\lambda'}(\Phi) \; D_{\lambda'}(\cos\theta_h, \phi_h), \qquad (3.19)$$

where λ and λ' indicate the helicity state of the J/ψ meson (λ, $\lambda' = -1, 0, +1$), D_λ is the spin-one D-function, and $\rho_{\lambda\lambda'}(\Phi)$ is the density matrix. The exact form of the above D-function depends on the type of the decay product (fermions or bosons) and the type of the interaction contributing to the decay. The above density matrix contains the information of the polarizations both on the virtual photon and the

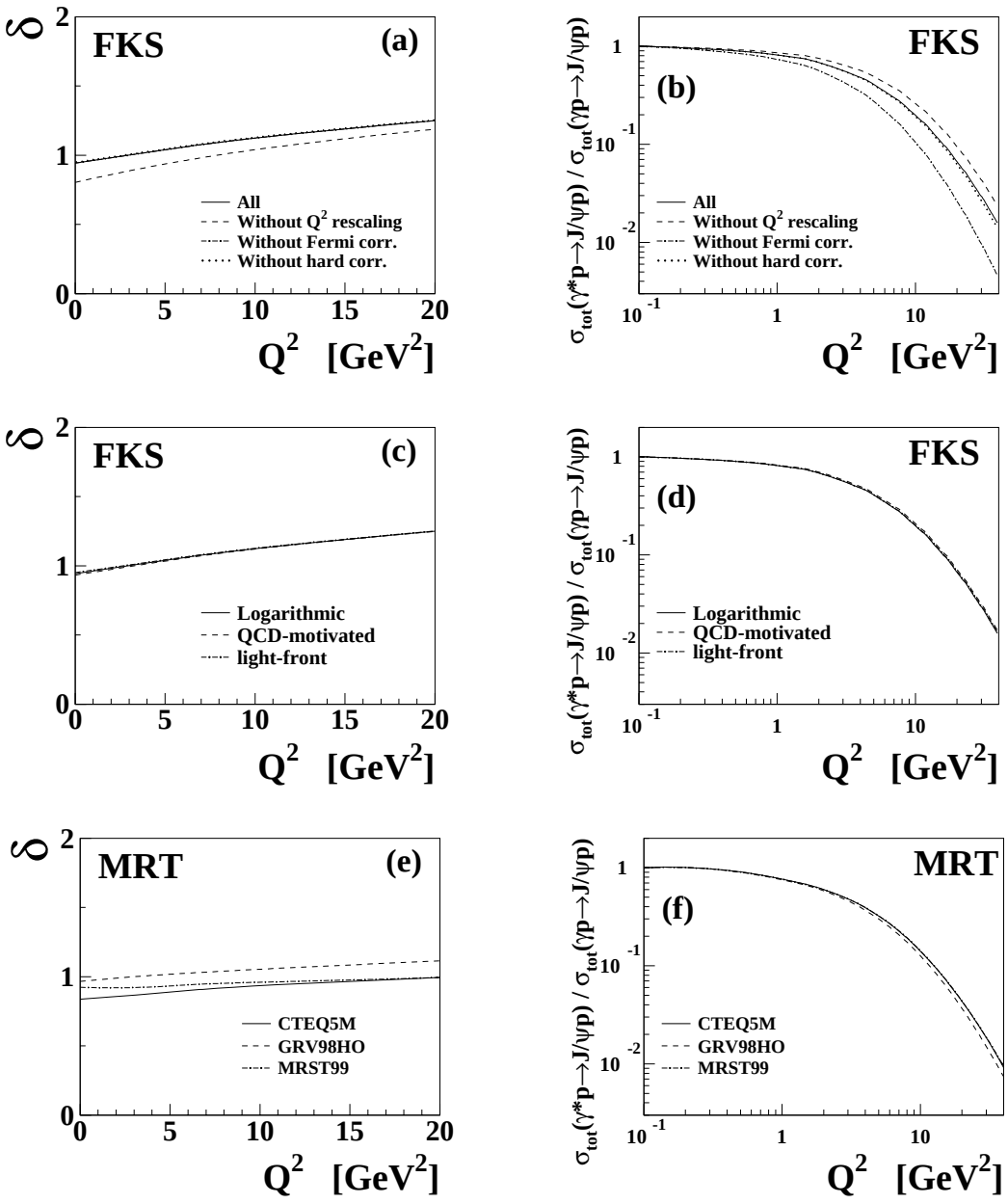

Figure 3.9: *The W-slope parameter δ and the Q^2-dependence of the cross section. (a),(b) With the different higher-order QCD corrections. (c),(d) With the different potential functions for the J/ψ. (e),(f) With the different gluon density parameterizations. The Q^2-dependence of the cross sections is calculated at $W = 90\ GeV$.*

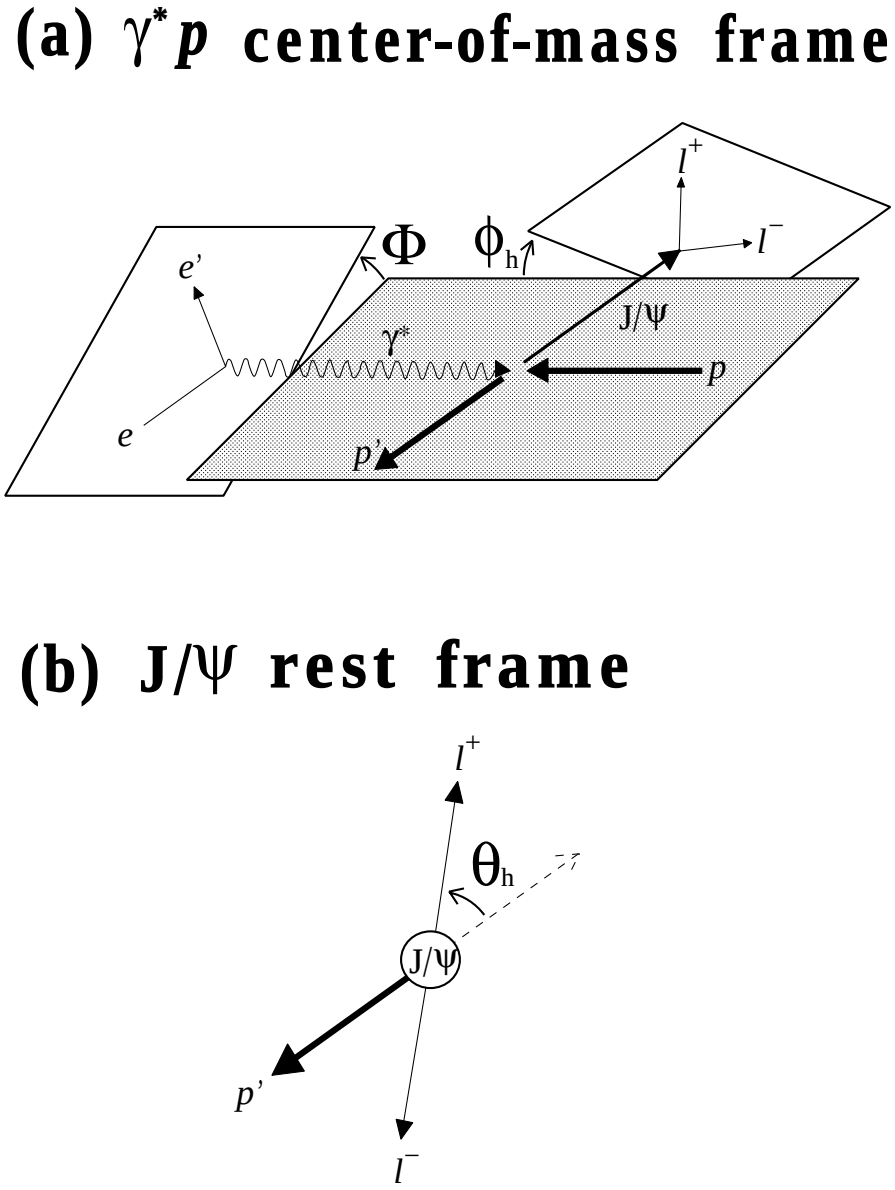

Figure 3.10: *The three planes and the decay angles in J/ψ production. e and p are the incoming electron and proton, respectively, and e′ and p′ are the corresponding outgoing particles. (a) The three planes in the γ*p center-of-mass frame and the angles, Φ and ϕ_h. (b) The decay angle θ_h. The negative direction of the outgoing proton (the dashed arrow) is used as a quantization axis.*

J/ψ meson as

$$\rho_{\lambda\lambda'}(\Phi) \;=\; \sum_{\alpha=0}^{8} \Pi_\alpha(\Phi)\; \rho^\alpha_{\lambda\lambda'}, \tag{3.20}$$

where the running suffix α is originated from the Lorentz suffix of the polarization vector of the virtual photon. Π_α indicates the photon density matrix elements, and $\rho^\alpha_{\lambda\lambda'}$ denotes the spin density matrix elements of the J/ψ meson. The terms with $\alpha = 0, 1, 2, 3$ correspond to the contribution from the transversely-polarized photon, $\alpha = 4$ for the longitudinally-polarized photon, and $\alpha = 5, 6, 7, 8$ for the interference terms. In case of unpolarized lepton beams, which is the case of this study, the following elements of the photon density matrix are zero:

$$\Pi_\alpha \;\equiv\; 0 \quad \text{for } \alpha = 3, 7, 8. \tag{3.21}$$

The more commonly-used spin density matrix is defined as

$$r^{04}_{\lambda\lambda'} \;=\; \frac{\rho^0_{\lambda\lambda'} + \epsilon R\, \rho^4_{\lambda\lambda'}}{1 + \epsilon R}, \tag{3.22}$$

$$r^{\alpha}_{\lambda\lambda'} \;=\; \frac{\rho^\alpha_{\lambda\lambda'}}{1 + \epsilon R} \qquad \text{for } \alpha = 1, 2 \quad \text{and} \tag{3.23}$$

$$r^{\alpha}_{\lambda\lambda'} \;=\; \frac{\sqrt{R}\rho^\alpha_{\lambda\lambda'}}{1 + \epsilon R} \qquad \text{for } \alpha = 5, 6, \tag{3.24}$$

where R and ϵ are defined in Eqs. (2.15) and (2.16) (p.8), respectively. The reason for combining $\rho^0_{\lambda\lambda'}$ and $\rho^4_{\lambda\lambda'}$ is that those two cannot be distinguished due to high values of ϵ ($\gtrsim 0.9$) in the kinematical region of this analysis.

The parity conservation and the hermitian nature of the density matrix reduce

the number of independent elements into 15, leading to

$$
\begin{aligned}
W_d(\cos\theta_h, \phi_h\, \Phi) \quad \propto \quad & \frac{1}{2}(1 + r^{04}_{00}) + \frac{1}{2}(1 - 3r^{04}_{00}) \cos^2\theta_h \\
& + \sqrt{2} Re\{r^{04}_{10}\} \sin(2\theta_h)\, \cos\phi_h + Re\{r^{04}_{1-1}\} \sin^2\theta_h\, \cos(2\phi_h) \\
& - \epsilon \cos(2\Phi) \Big[r^1_{11} + r^1_{00} \sin^2\theta_h + r^1_{11} \cos^2\theta_h \\
& \qquad + \sqrt{2} Re\{r^1_{10}\} \sin(2\theta_h) \cos\phi_h + r^1_{1-1} \sin^2\theta_h \cos(2\phi_h) \Big] \\
& - \epsilon \sin(2\Phi) \Big[\sqrt{2} Im\{r^2_{10}\} \sin(2\theta_h) \sin\phi_h + Im\{r^2_{1-1}\} \sin^2\theta_h \sin(2\phi_h) \Big] \\
& + \sqrt{2\epsilon(1+\epsilon)} \cos\Phi \Big[r^5_{11} + r^5_{00} \sin^2\theta_h + r^5_{11} \cos^2\theta_h \\
& \qquad + \sqrt{2} Re\{r^5_{10}\} \sin(2\theta_h) \cos\phi_h + r^5_{1-1} \sin^2\theta_h \cos(2\phi_h) \Big] \\
& + \sqrt{2\epsilon(1+\epsilon)} \sin\Phi \Big[\sqrt{2} Im\{r^6_{10}\} \sin(2\theta_h) \sin\phi_h \\
& \qquad + Im\{r^6_{1-1}\} \sin^2\theta_h \sin(2\phi_h) \Big].
\end{aligned}
$$

The hypothesis called *s-channel helicity conservation* (SCHC) denotes that the helicity state does not change, in the $\gamma^* p$ center-of-mass frame, between the virtual photon and the vector meson. The SCHC is experimentally found to be a good approximation in the small-$|t|$ region ($|t| \lesssim 1\,\mathrm{GeV}^2$).

Assuming the SCHC, the decay angular distribution is described in terms of $\cos\theta_h$ and Ψ only, where Ψ is defined as $\Psi = \phi_h - \Phi$,

$$
\begin{aligned}
W_d(\cos\theta_h, \Psi) \quad \propto \quad & \frac{1}{2}(1 + r^{04}_{00}) + \frac{1}{2}(1 - 3r^{04}_{00}) \cos^2\theta_h \\
& - \epsilon r^1_{1-1} \sin^2\theta_h \cos(2\Psi) \\
& + 2\sqrt{\epsilon(1+\epsilon)} Re\{r^5_{10}\} \sin(2\theta_h) \cos\Psi,
\end{aligned} \tag{3.25}
$$

and the following formula holds,

$$
R \quad = \quad \frac{1}{\epsilon} \frac{r^{04}_{00}}{1 - r^{04}_{00}}. \tag{3.26}
$$

The value of r^{04}_{00} corresponds to a probability to observe a longitudinally-polarized state of the J/ψ meson. In the formula (3.26), the polarization of the J/ψ meson is directly related to that of the virtual photon.

Assuming the natural parity exchange (NPE) hypothesis [23] in addition to the SCHC, the following relation holds,

$$r^{04}_{00} \;=\; 1 - 2r^{1}_{1\,-1}. \tag{3.27}$$

Substituting the above equation into Eq. (3.25) and integrating over $\cos\theta_h$, the following formula is obtained,

$$W_d(\Psi) \;\propto\; 1 - \epsilon\, r^{1}_{1\,-1}\cos(2\Psi). \tag{3.28}$$

The value of $r^{1}_{1\,-1}$ corresponds to a probability to observe a transversely-polarized state of the J/ψ meson. The formula (3.28) is used, in this analysis, to derive $r^{1}_{1\,-1}$ on the assumption of the SCHC and NPE.

3.4 J/ψ Production and the Aim of this Thesis

The most important aim of this thesis is to test pQCD-based predictions in J/ψ production. The J/ψ is a fit vector-meson state for the test from the following reasons.
In a theoretical point of view,

- there is a hard scale to be used in pQCD calculations from the heavy charm mass;
- the J/ψ state can be calculated based on the non-relativistic QCD,

and in an experimental point of view,

- J/ψ production is measured with a clean and simple final state in the leptonic decay channels ($J/\psi \to e^+e^-, \mu^+\mu^-$);
- the narrow resonance width (87 ± 5 keV) makes it easy to extract the signal.

The pQCD describes various aspects of J/ψ production. In this thesis, quantitative comparisons of the results with pQCD-based predictions are performed using the following quantities:

- the W-slope of the cross section as a function of Q^2, parameterized as $\sigma^{\gamma^* p \to J/\psi\, p}_{tot}(W;\, Q^2_0) \;\propto\; W^{\delta(Q^2_0)}$,
- the Q^2-slope at a fixed W value of $W = 90$ GeV where the experimental acceptance is at the highest, parameterized as $\sigma^{\gamma^* p \to J/\psi\, p}_{tot}(Q^2) \;\propto\; 1/(Q^2 + M^2_{J/\psi})^n$, and

- $R = \sigma_L/\sigma_T$ as a function of Q^2 at $W = 90$ GeV.

It should be emphasized that the above comparisons are free from uncertainties on the cross section normalization. Absolute sizes of the cross section from the pQCD-based models are tested at $W = 90$ GeV with the Q^2 dependence.

Chapter 4

ZEUS Experiment

In this thesis, data taken in the ZEUS experiment are used. The experiment has been performed at the Deutsches Elektronen-Synchrotron (DESY) in Hamburg, using an electron or a positron ($e^{\pm}$) and a proton beams supplied by the HERA collider. In this chapter, the experimental apparatus of this analysis is explained.

4.1 The HERA Collider

HERA (Hadron-Elektron Ring Anlage) is the first and the only lepton-proton collider in the world. The layout is shown in Figure 4.1. HERA consists of two rings. One is for the $e^{\pm}$ beam and the other for the proton beam. They overlap at the two interaction regions in the south and north halls. In the south hall, the ZEUS experiment has been carried out since 1992, and in the north hall, the H1 experiment has been done. The energy of the $e^{\pm}$ beam has been set to 27.5 GeV since 1994. The proton beam energies were set to 820 GeV in 1994-1997 and then increased to 920 GeV in 1998-2000. The corresponding center-of-mass energy of the two beam particles is 300 GeV in 1994-1997 and 318 GeV in 1998-2000, and the corresponding $e^{\pm}$ beam energy in the proton rest frame is 48 TeV in 1994-1997 and 54 TeV in 1998-2000.

HERA delivered e^{+} beams during the data-taking periods for this analysis except the period from 1998 to April 1999. Figure 4.2 shows the integrated luminosities taken on-tape by ZEUS in the 1994-2000 data-taking periods. The total integrated luminosity is above 100 pb^{-1}, which makes it possible to access physics with a cross section below 1 pb.

The design parameters of HERA are listed in Table 4.1. Particles in the rings are

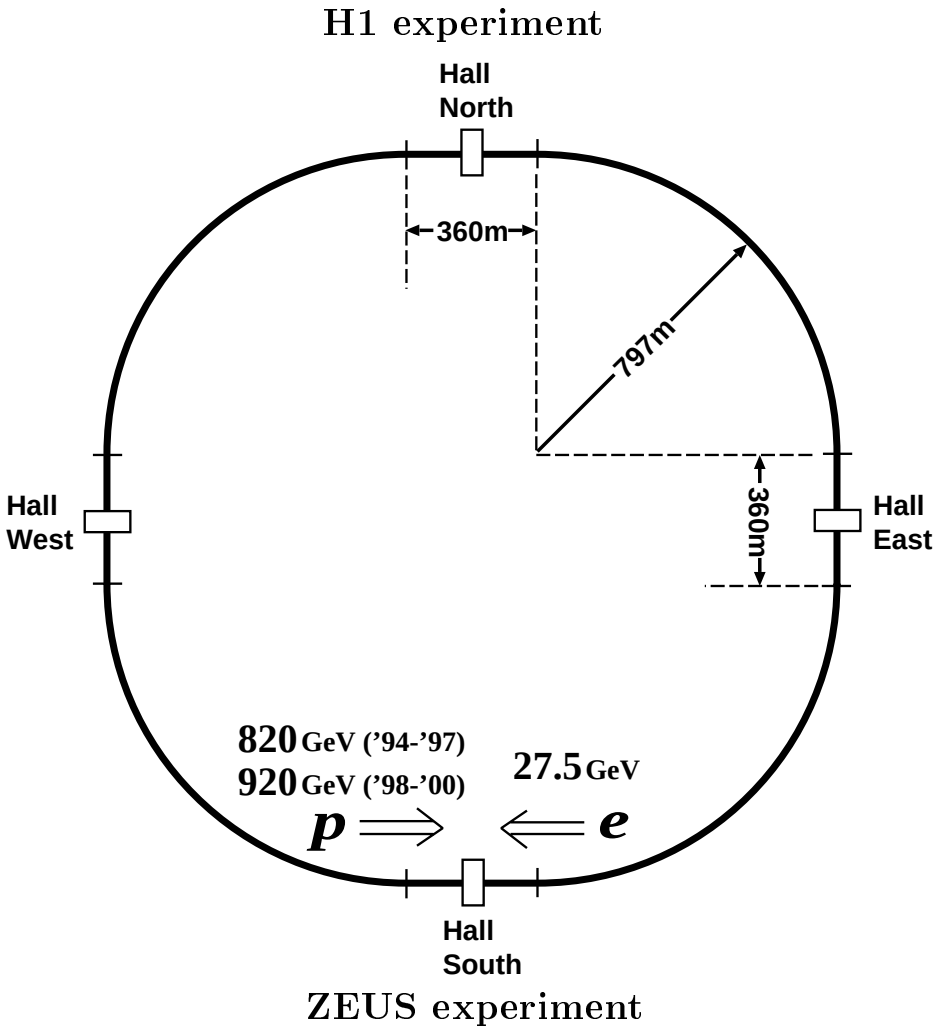

Figure 4.1: *A layout of the ep collider HERA*

	Proton ring		Electron ring	Units
Nominal energy	820		30	GeV
c.m.energy		314		GeV
Q^2_{max}		98400		GeV^2
Luminosity		1.5×10^{31}		$cm^{-2}s^{-1}$
Polarization time			27	min
Number of experimental halls		4		
Number of interaction points		2		
Crossing angle		0		mrad
Circumference		6336		m
Length of straight section		360		m
Bending radius	588		608	m
Magnetic field	4.68		0.16	T
Energy range	300-1000		10-33	GeV
Injection energy	40		14	GeV
Circulating current	160		60	mA
Number of particles per bunch	1.0×10^{11}		3.5×10^{10}	
Maximum number of bunches		220		
Time between crossings		96		ns
Beam size at crossing ($\sigma^*_x/\sigma^*_y/\sigma^*_z$)	0.300/0.095/440		0.264/0.017/30	mm
Total RF power	1		13.2	MW
RF frequency	52.033/208.13		499.667	MHz
Filling time	20		15	min

Table 4.1: *The design parameters of HERA*

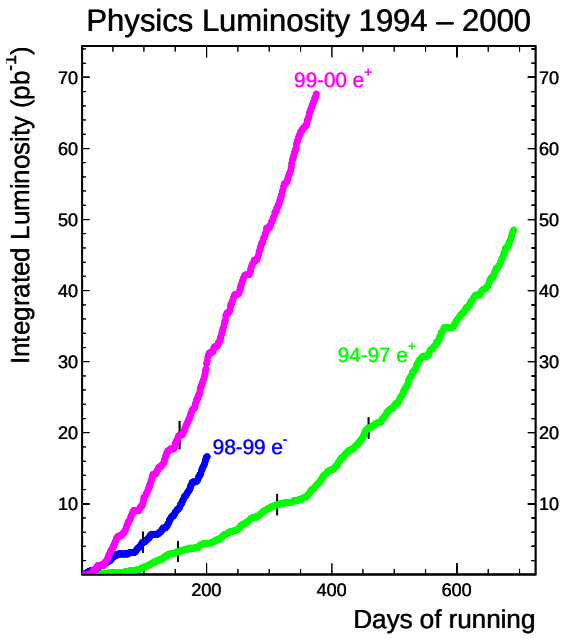

Figure 4.2: *The integrated luminosities taken on-tape by ZEUS in the 1994-2000 data-taking periods.*

stored in bunches. There are at maximum 220 bunches with a small bunch crossing interval of 96 ns. Some bunches are not filled with particles, which are used to study the background from interactions between the beam and residual gas particles in the beam pipe (the beam-gas background).

4.2 The ZEUS Detector

The ZEUS detector [24] is a multipurpose detector for HERA, which aims to detect almost all the particles produced from ep collisions. A schematic view of the detector is shown in Figure 4.3. As the center of mass system of the two beam particles is moving toward the proton beam direction in the laboratory frame, the ZEUS detector has an asymmetric structure with respect to the plane perpendicular to the beam line. The components related to this analysis are, from the interaction region toward outside, the central tracking detector (CTD), the magnetic solenoid giving a magnetic field to the CTD, the uranium-scintillator calorimeter (CAL), the inner barrel and rear muon chambers, the magnetized iron yoke, and the outer barrel and rear muon chambers. Special components related to the detection of the scattered electron are implemented. They are the small angle rear tracking detector

(SRTD) and the hadron-electron separator (HES). The forward plug calorimeter (FPC) is used to reduce events with proton dissociation by requiring no significant energy deposits. These components are explained in the next section.

The ZEUS coordinate system is defined as the right-handed Cartesian system with the Z-axis taken to be parallel to the HERA beam line and pointing the proton beam direction which is referred to as *the forward direction*. The X-axis is taken to be in the horizontal direction, pointing the center of the HERA rings, as shown in Figure 4.3. The polar angle θ is measured in the laboratory frame with respect to the positive direction of the Z-axis.

4.2.1 The central tracking detector

The central tracking detector (CTD) [25] is a cylindrical drift chamber with an inner radius of 18.2 cm, outer radius of 79.4 cm and a length of 105 cm. The CTD consists of nine superlayers (SLs), each of which has a cell structure, and each cell has eight sense wires. The nine SLs are called SL1-9 from the inner to the outer side. Five of the SLs have wires parallel to the beam line and four have a small stereo angle (Figure 4.4). The CTD is filled with a gas mixture of argon, CO_2 and ethane. The polar angle coverage is $15^\circ < \theta < 164^\circ$, which corresponds to the polar angle with which particles pass through SL3. The CTD is located in the 1.43 T magnetic field supplied by the superconducting solenoid coil with a radius of 86 cm in order to measure momenta of charged particles.

The angular resolution is around 1 mrad on both polar and azimuthal angles in the fiducial region. The momentum resolution for full length tracks [26] is

$$\frac{\sigma(p_T)}{p_T} \;=\; 0.0058\,p_T \;\oplus\; 0.0065 \;\oplus\; \frac{0.0014}{p_T}, \tag{4.1}$$

where p_T is a transverse momentum in GeV.

4.2.2 The uranium-scintillator calorimeter

The ZEUS calorimeter (CAL) [27] is a sandwitch-type calorimeter consisting of depleted uranium (DU) plates as an absorber and plastic scintillators as an active material. The geometrical coverage is 99.8 % of the whole solid angle. The CAL has a good resolution especially for measurements of hadronic particles due to the equal responses to electrons and hadrons: $e/h \sim 1$. This ratio has been achieved by tuning the thickness of the scintillator and of the absorber (DU). From the results

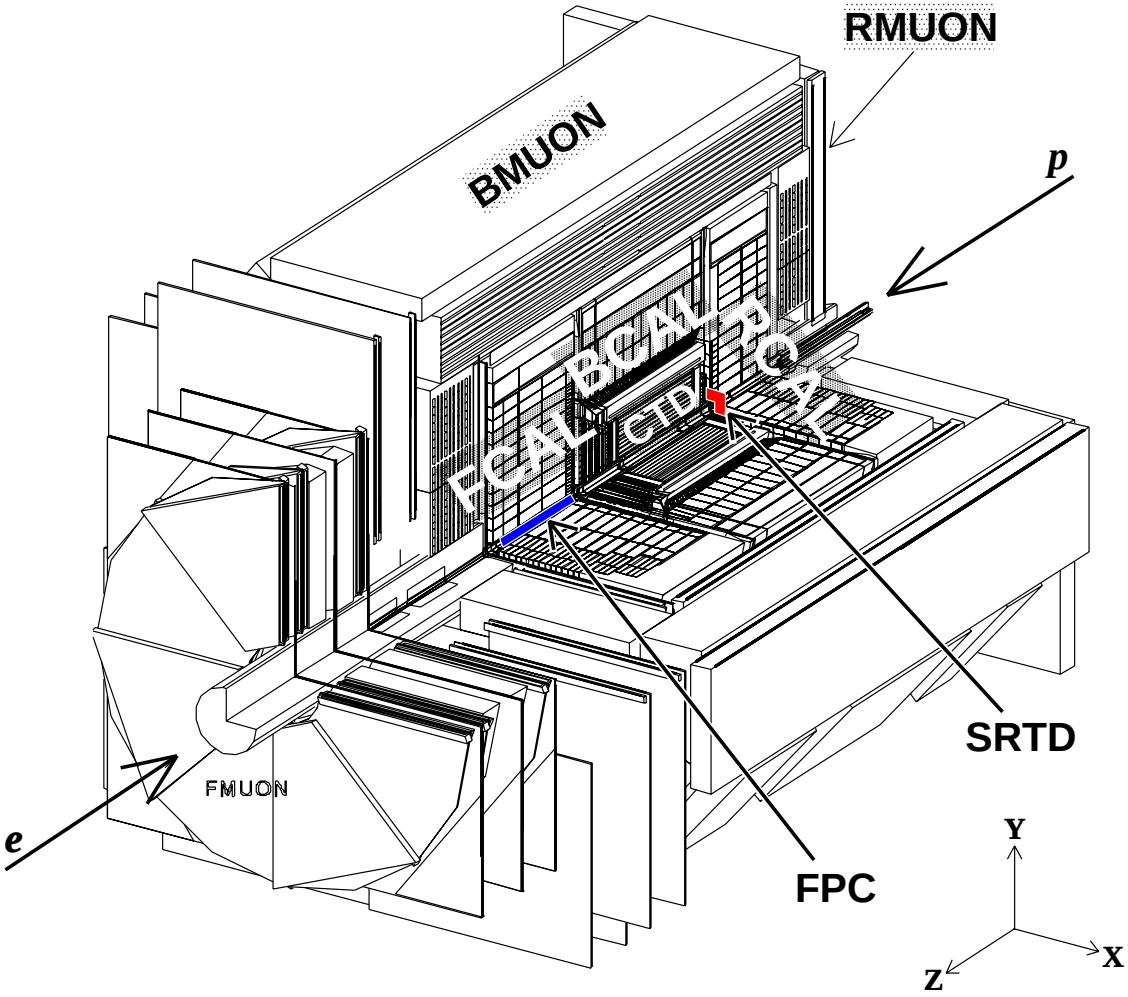

Figure 4.3: *A schematic view of the ZEUS detector.*

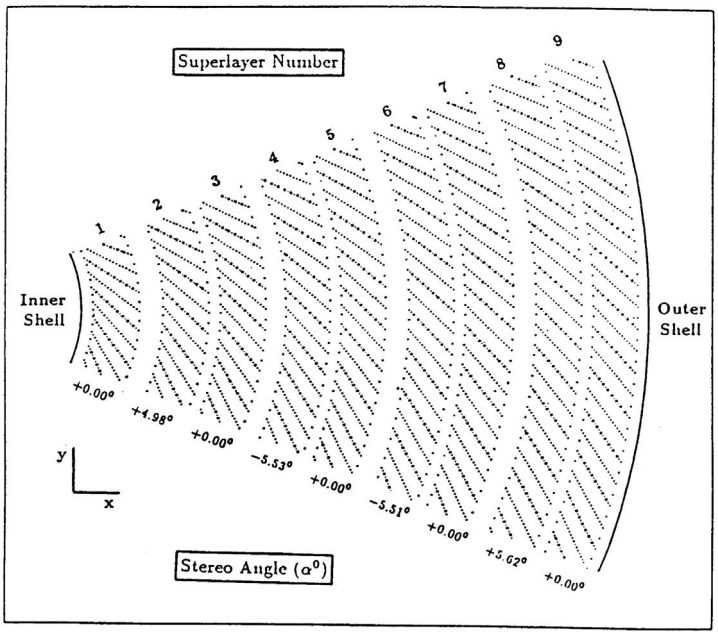

Figure 4.4: *A layout of the wires in the CTD*

of the beam tests [27], the following ratio was obtained,

$$e/h = 1.00 \pm 0.03 \tag{4.2}$$

for energies above 3 GeV. The energy resolutions, also from the beam tests, are

$$\frac{\sigma(E)}{E} = \frac{18\,\%}{\sqrt{E}} \oplus 1\,\% \quad \text{for electrons} \quad \text{and} \tag{4.3}$$

$$\frac{\sigma(E)}{E} = \frac{35\,\%}{\sqrt{E}} \oplus 2\,\% \quad \text{for hadrons,} \tag{4.4}$$

where E is an energy in GeV.

The CAL consists of the three parts: the FCAL, BCAL and RCAL, which are located in the forward, barrel and rear region, respectively, as seen in Figure 4.5. A structural unit of the CAL is called *tower*. Its cross section is shown in Figure 4.6, where particles enter from the right side. The towers have a rectangular shape of a $20 \times 20\,\mathrm{cm}^2$ cross section and a length of 152.5 cm, 105.9 cm or 87 cm for the FCAL, BCAL or RCAL, respectively. Energy deposits are optically read out by photo-multiplier tubes (PMTs) through wavelength shifters attached on both sides. The tower is longitudinally divided into two sections: the electromagnetic section

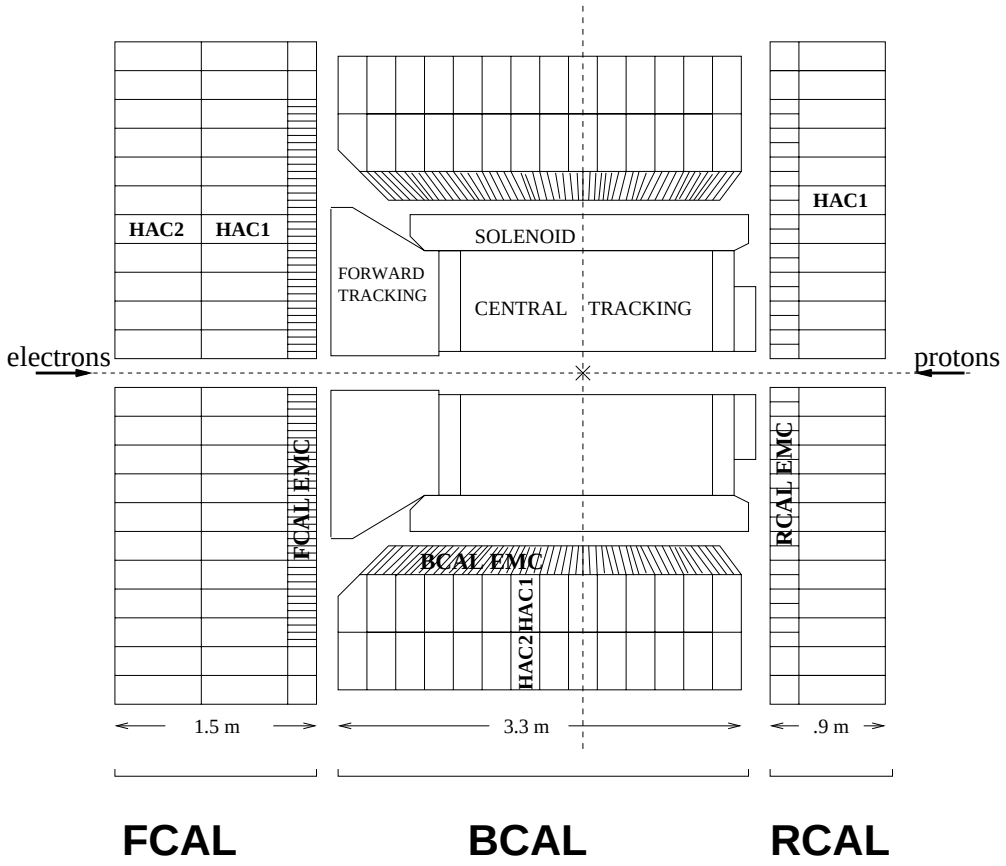

Figure 4.5: *A cross section of the CAL.*

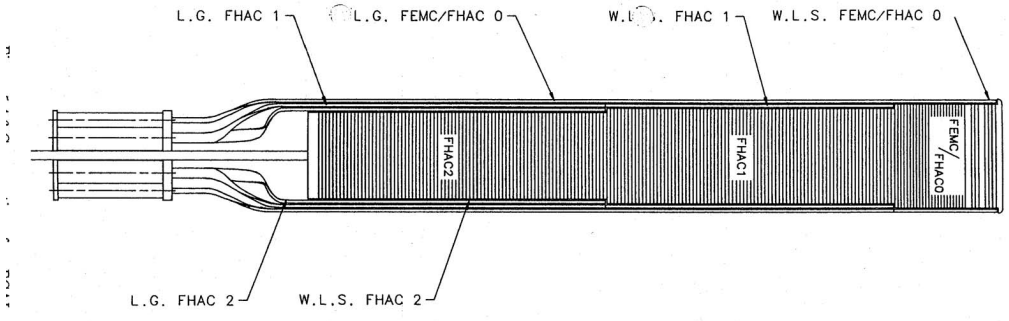

Figure 4.6: *An example of the towers in the FCAL. Particles enter from the right side.*

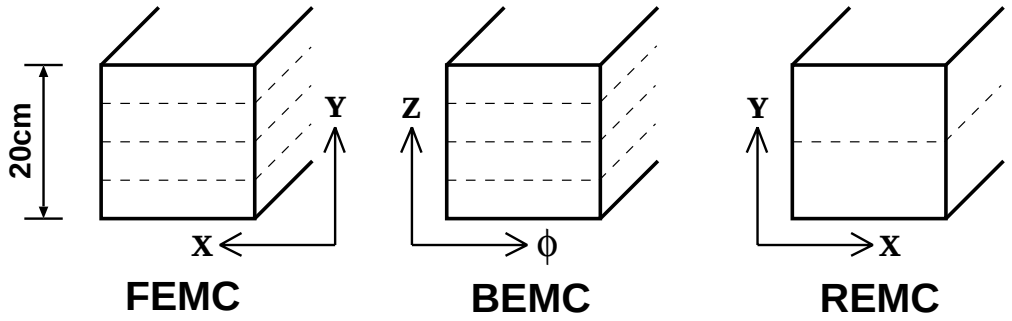

Figure 4.7: *Division of the EMC sections into cells. Examples of the EMC sections of the towers, the FEMC, BEMC and REMC, are shown from the FCAL, BCAL and RCAL, respectively.*

	FCAL			BCAL			RCAL	
	EMC	HAC1	HAC2	EMC	HAC1	HAC2	EMC	HAC1
Number of layers	25	80	80	21	49	49	25	80
Radiation length (X_0)	25.9	84.2	84.2	22.7	52.4	52.5	25.9	84.2
Absorption length (λ)	0.96	3.09	3.09	1.05	2.03	2.04	0.95	3.09
Thickness (cm)	25.1	64.0	64.4	21.3	42.2	42.4	23.6	64.4

Table 4.2: *The parameters of the CAL.*

(EMC) and the hadronic section (HAC). Both of the EMC and HAC have the same internal structure, i.e., a sandwich of the DU and scintillator. The EMC section is subdivided into four (FCAL and BCAL) or two (RCAL) *cells* as schematically shown in Figure 4.7. The cell is a unit of the energy measurement in the CAL. For the FCAL and BCAL, the HAC section is further divided longitudinally into two sections of the HAC1 and HAC2. The parameters of the CAL are summarized in Table 4.2 on the number of layers, radiation length, absorption length and the thickness.

The signal from the uranium radioactivity is used in the calibration to obtain a stable gain in the long period of the ZEUS experiment.

4.2.3 The barrel and rear muon chambers

The barrel (BMUON) and rear (RMUON) muon chambers (BRMUON) [28] are located outside the CAL. The chambers consist of limited streamer tubes placed both inside and outside the magnetized iron yoke. The polar angle coverages are

$34^\circ < \theta < 135^\circ$ and $134^\circ < \theta < 171^\circ$ for BMUON and RMUON, respectively.

This detector is used only in the study of systematical errors.

4.2.4 The small angle rear tracking detector

Positions of scattered electrons with low scattering angles can be measured using the small angle rear tracking detector (SRTD) [29]. This detector is a scintillator strip hodoscape located in front of the RCAL modules adjacent to the beam-pipe hole, as shown in Figure 4.3. The polar angle coverage is $162^\circ < \theta < 176^\circ$, which is outside the CTD coverage.

The SRTD consists of four $24 \times 44\,\mathrm{cm}^2$ quadrants with two layers of scintillator strips. The strips are 1 cm wide and 0.5 cm thick. The directions of the strips are orthogonal between the two layers: vertical and horizontal strips. Scintillation lights are read from one of the ends of the strip through an optical fiber by a PMT installed behind the RCAL.

The position resolution is about 0.3 cm for electrons with a pre-showering. This is better than the typical position resolution with the CAL (1.0 cm). The SRTD alignment is understood with the precision of 2 mm [30], which was estimated using matching tracks reconstructed in the rear tracking detector located behind the CTD and in front of the SRTD.

The SRTD can be used also as a presampler to correct an energy loss in the inactive materials in front of the RCAL.

4.2.5 The hadron-electron separator

The hadron-electron separator (HES) is a silicon-pad detector used for the separation between electrons and hadrons. Each silicon diode (silicon-pad) has a size of $3 \times 3\,\mathrm{cm}^2$ wide and $400\,\mu$m thick. They are laid at the $3\,X_0$ depth in the EMC sections of the FCAL (FHES) and RCAL (RHES) in order to measure a charged multiplicity of the shower in the CAL. At the $3\,X_0$ depth, lateral sizes of electromagnetic showers are expected to be maximum. About 10000 silicon-pads are used for each of the FHES and RHES.

This detector is used only in the study of systematical errors.

4.2.6 The forward plug calorimeter

The forward plug calorimeter (FPC) [31] is a shashlik lead-scintillator calorimeter with wave length shifter fiber readout. It has been installed in the beam-pipe hole of the FCAL since 1998 in order to extend the polar angle coverage of the calorimeter to the forward direction, from $\eta \lesssim 4.0$ to $\eta \lesssim 5.0$ where η stands for pseudo-rapidity $\left(\eta \stackrel{\text{def}}{\equiv} -\ln(\tan\frac{\theta}{2})\right)$.

The FPC is subdivided longitudinally into an electromagnetic and a hadronic sections. The electromagnetic section consists of 10 layers of lead and scintillator corresponding to $26.5\,X_0$ and $0.9\,\lambda$. The hadronic section consists of 50 layers of lead and scintillator corresponding to $5.4\,\lambda$.

The energy resolutions are, from the beam tests,

$$\frac{\sigma(E)}{E} = \frac{41\,\%}{\sqrt{E}} \oplus 6\,\% \quad \text{for electrons} \quad \text{and} \tag{4.5}$$

$$\frac{\sigma(E)}{E} = \frac{65\,\%}{\sqrt{E}} \oplus 6\,\% \quad \text{for hadrons,} \tag{4.6}$$

where E is an energy in GeV.

4.2.7 The luminosity monitor

Luminosities of ep collisions are measured using the bremsstrahlung process, $e\,p \rightarrow e\,p\,\gamma$, with the photon detected by the luminosity monitor (LUMI).

The luminosity monitor consists of two calorimeters: one of them is for the detection of scattered electrons (LUMI-e) and the other is for the detection of photons radiated colinearly from the electron line (LUMI-γ). The LUMI-e is located at $Z = -35\,\text{m}$ and the LUMI-γ is located at $Z = -104\,\text{m}$ as shown in Figure 4.8. Both of the detectors consist of lead-scintillator sandwiches with an energy resolution of $\sigma(E)/E = 18\,\%/\sqrt{E(\text{GeV})}$. In front of the LUMI-$\gamma$, a carbon filter with the thickness of $3\,X_0$ is equipped in order to absorb photons from the synchrotron radiation. The utilization of this filter degrades the resolution into $\sigma(E)/E = 24\,\%/\sqrt{E(\text{GeV})}$. The LUMI-$e$ is used for the systematical check of the luminosity measurement.

4.2.8 The pipeline trigger and the data acquisition system

At HERA, the beam-gas background rate is much higher than the expected rate from ep interactions of the beam particles. In addition, the bunch crossing interval is short (96 ns). Therefore, in order to avoid a long dead time and obtain a high

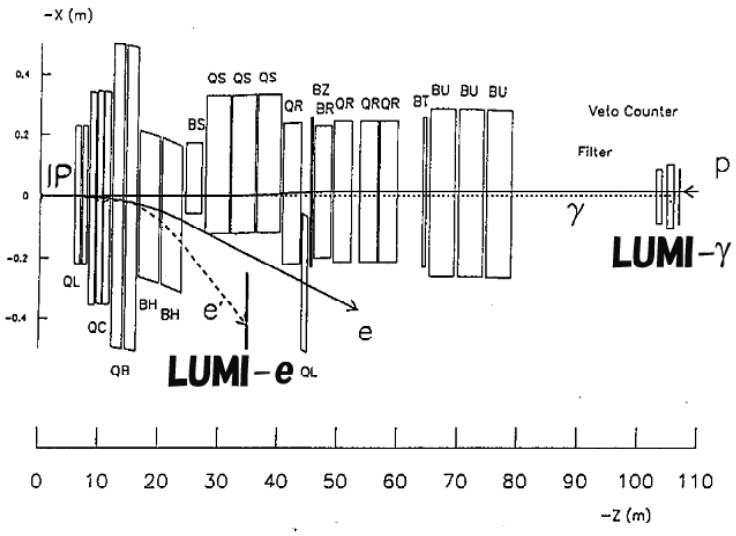

Figure 4.8: *Location of the two luminosity calorimeters: LUMI-e and LUMI-γ.*

luminosity, a three-level trigger system is adopted in the ZEUS experiment. The three levels are called the first level trigger (FLT), the second level trigger (SLT) and the third level trigger (TLT). Figure 4.9 shows a schematic diagram on the three-level trigger and the data acquisition system. The functions of the FLT, SLT and TLT are summarized below.

- The FLT consists of two parts: the component FLTs and the global FLT (GFLT). Each component FLT produces trigger quantities, which are sent to the GFLT. The GFLT makes a decision, from those quantities and the trigger logics, whether the event is accepted or not. While the FLT is processing, raw data are stored in the pipeline consisting of arrays of switched capacitors or digital memories. If a positive decision is made, an accept flag is sent to each component. Then the information in the pipeline corresponding to the bunch crossing of the *ep* interaction is taken out. Results are stored in the digitizer buffers and the GFLT does not make a next decision until all of the components have finished reading data from the pipelines. The typical output rate was 200 Hz for the 1996-2000 runs.

- The SLT also consists of two parts like the FLT: the component SLTs and the global SLT (GSLT). Each component SLT produces trigger quantities from the information stored in the digitizer buffers. GSLT processes the trigger logics using quantities sent from the component SLTs. If GSLT makes a positive

decision, data in the digitizer buffers are sent to the event builder which collects data from all of the components and constructs an event-data structure according to the format of the database. In the 1996-2000 runs, the typical output rate was 50 Hz.

- The TLT reduces the output rate from the SLT down to around 10 Hz with a large computing power of workstations. In order to process more complicated trigger logics, a distributed computing system is adopted. Information of an event which passed the TLT is sent to the mass storage. In the 1996-2000 runs, the typical output rate was about 10 Hz, which is acceptable for recording data onto tape.

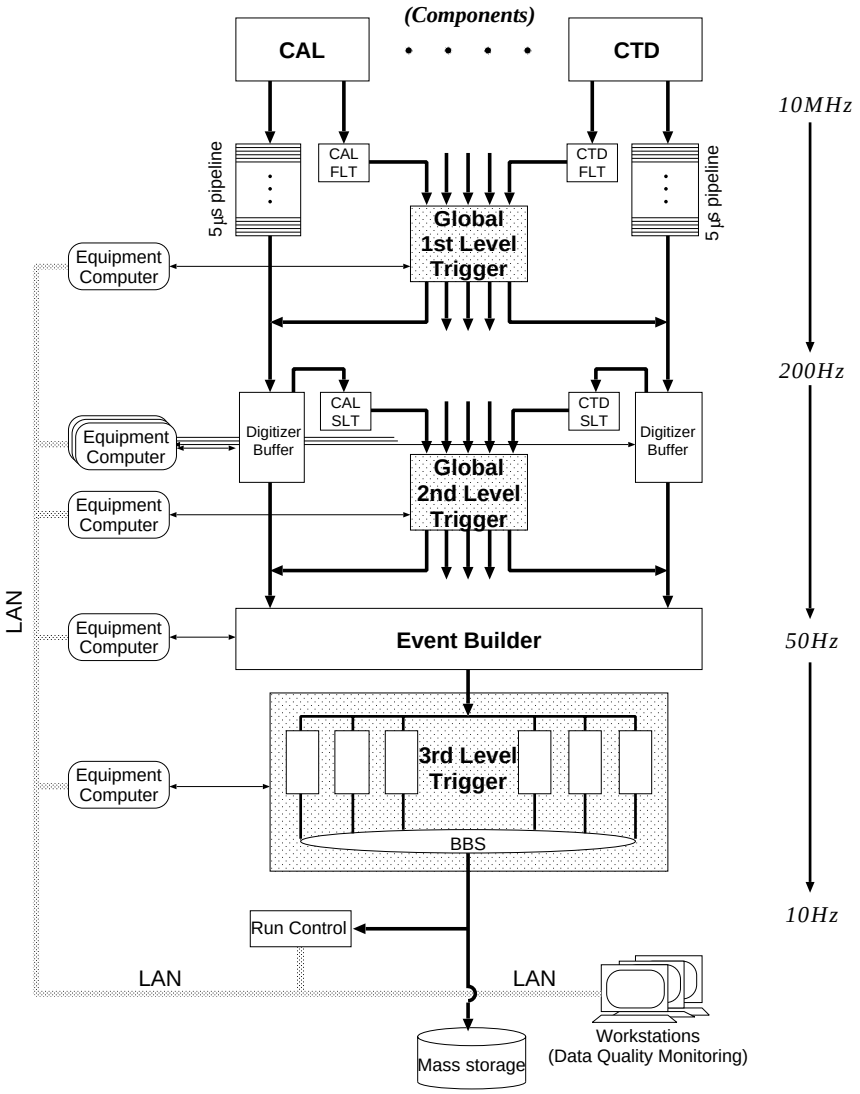

Figure 4.9: *A schematic diagram of the pipeline trigger and the data acquisition system.*

Chapter 5

Monte Carlo Simulations

In order to measure cross sections, it is necessary to correct detector effects: trigger efficiencies, geometrical acceptances, resolutions and migrations. A simulation using the Monte Carlo (MC) method is adopted in this analysis to estimate all the relevant detector effects. Relevant physics processes in ep interactions are requested to be correctly simulated for the comparison of the data with the simulation. In this chapter, descriptions on the MC event generators and the subsequent detector simulation are presented.

5.1 Event Generators

Two event generators have been developed in this study.

5.1.1 J/ψ electroproduction

The MC event generator ("J/ψ-MC") to simulate exclusive electroproduction of J/ψ mesons including the QED radiative effects, as shown in Figure 5.1, generates events according to the following four steps.

(1) A scattered electron is generated with a four-momentum which is determined according to the Q^2 and y distributions calculated based on the following parameterization:

$$\sigma_{tot}^{\gamma^* p \to J/\psi\, p}(Q^2, W) \quad \propto \quad \frac{W^\delta}{\left(Q^2 + M_{J/\psi}^2\right)^n}, \tag{5.1}$$

where n and δ are the Q^2 and W slope parameters, respectively. The above parameterization is motivated by the VDM (Eqs. (3.3), (3.4)) and the Regge

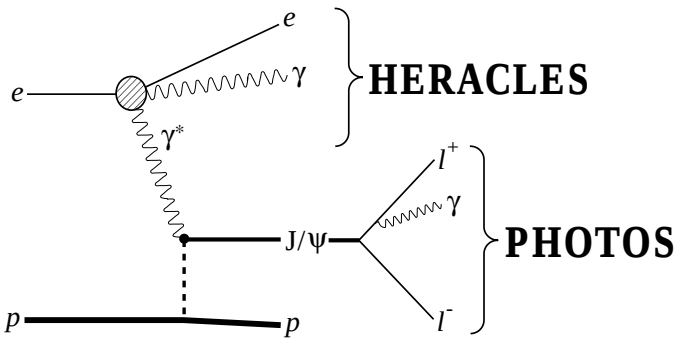

Figure 5.1: *Exclusive J/ψ electroproduction and the MC programs to simulate QED radiative effects: HERACLES [32] and PHOTOS [33]. e=$\{e^+, e^-\}$, $l^{\pm}$=$\{e^{\pm}, \mu^{\pm}\}$.*

theory (Eq. (3.11)). In this step, the cross section formula including the QED radiative corrections on the scattered electron line is used instead of the Born-level formula (Eq.(2.17) in p.8). The radiative effects are calculated using the MC generator `HERACLES 4.6.1` [32].

(2) After the generation of the scattered electron, four-momenta of a J/ψ meson and a scattered proton are generated according to the following distribution on t,

$$\frac{d\sigma_{tot}^{\gamma^* p \to J/\psi p}}{d|t|} \propto e^{-b|t|}, \tag{5.2}$$

where b is a slope-parameter.

(3) Then a decay of the J/ψ meson is made with flat distributions of the decay angles: $\cos\theta_h$, ϕ_h and Φ. These flat distributions will be changed later to reproduce observed distributions in data using the reweighting technique. This will be described in the chapter 7.

(4) The four-momenta of the decay leptons are changed to simulate the radiative decay of the J/ψ by calling the MC program `PHOTOS 2.0` [33]. Zero, one or two photons are generated with this correction.

In this simulation, all of the fermion masses are kept non-zero everywhere.

Figure 5.2-(b)-(e) show the QED radiative corrections of the order of α_{QED} simulated with `HERACLES`. The included corrections are the Initial State Radiation (ISR), the Final State Radiation (FSR), the vertex correction and the vacuum polarization. Including all of the diagrams in Figure 5.2 leads to physically meaningful results with the gauge invariance and a finite cross section.

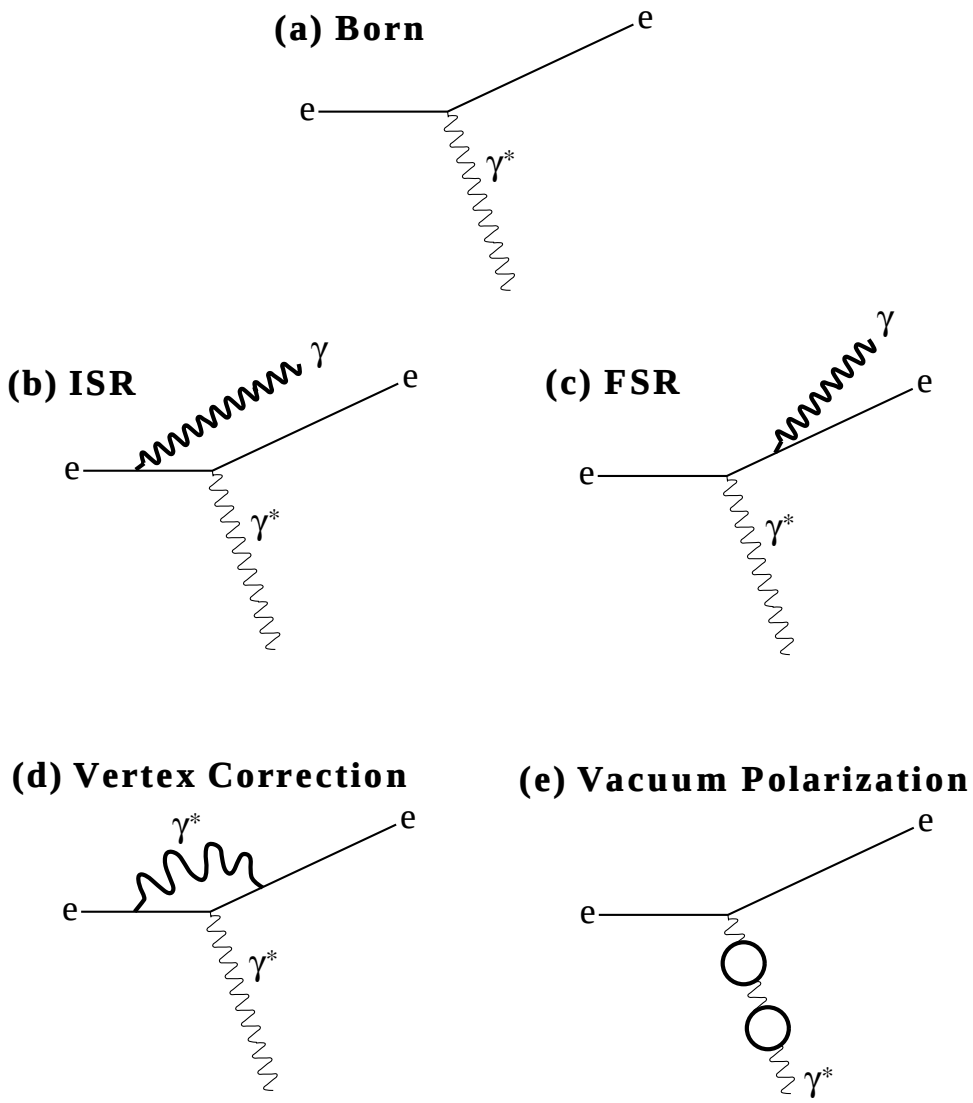

Figure 5.2: *QED radiative corrections on the scattered electron line: (b)-(e), included in the J/ψ-MC using HERACLES*

PHOTOS is a MC program which can simulate any radiative decay of any massive particle, producing unweighted events. PHOTOS gives radiative corrections based on the leading-logarithmic (collinear) approximation. The complete kinematics including radiated photon(s) is implemented. The proper soft photon behavior, the double bremsstrahlung and the interference effect between two photons are also reproduced. The photon radiation from the J/ψ meson itself is not included since PHOTOS is based on the factorization of the bremsstrahlung kernels. However, such a radiation is strongly suppressed due to the negative proper C-parity of the J/ψ.

870000 events of $J/\psi \to l^+l^-$ are generated and used, corresponding to a forty-times more statistics than that of the data.

5.1.2 Dilepton production in the QED

Dilepton production in the QED process is the only major background in this analysis. This process is simulated using the electroweak dilepton generator, named GRAPE-Dilepton [34]. The MC simulation with this generator is referred as "QED-MC" in this analysis.

Figure 5.3 shows Feynman diagrams included in the QED-MC: the two-photon Bethe-Heitler and the internal photon conversion. The exact matrix elements in the lowest-order QED processes are calculated in conjugation with the relevant four-body kinematics in which all of the singularities are regularized. In case of the di-electron channel, the interference effects between identical particles of e^-e^- or e^+e^+ in the final state are taken into account. Fermion masses are kept non-zero everywhere, both in the matrix elements and in the kinematics. The Fortran code to calculate the Feynman amplitudes and the basic kinematics was generated by the automatic calculation system GRACE [35].

For the process of $ep \to ep\,l^+l^-$ where the proton remains as the proton, the dipole-formfactor is used. For the process of $ep \to eN\,l^+l^-$ where the proton dissociates into a low invariant-mass system N, the electromagnetic structure functions are used. Those functions are calculated according to the parameterization from Brasse et al [36] for $M_N < 2\,\mathrm{GeV}$ (the proton resonance region) or from ALLM97 [37] for $M_N > 2\,\mathrm{GeV}$, where M_N is an invariant mass of the hadronic system N in Figure 5.3. These two parameterizations are based on fits to the experimental data on the inclusive measurement of the γ^*p total cross section. The exclusive hadronic final state is generated using the MC event generator SOPHIA [38], which includes resonance excitation and decay of nucleon, direct single pion production,

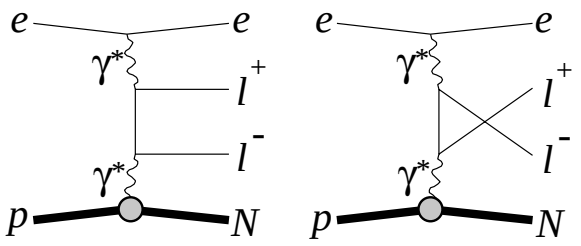

(a) Two-photon Bethe-Heitler

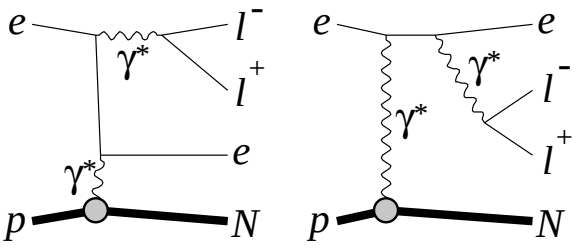

(b) Internal Photon Conversion

Figure 5.3: *Feynman diagrams included in the QED-MC. Exact matrix elements at tree level in the QED are calculated using GRAPE-Dilepton [34].* e=$\{e^+, e^-\}$, $l^{\pm}$=$\{e^{\pm}, \mu^{\pm}\}$. *N represents a (dissociated) proton or a nucleon resonance.*

light vector meson production, and diffractive and non-diffractive multi-pion production. The cross sections of those processes are based on experimental data, while the kinematics is determined by the underlying particle production process.

QED radiative corrections are done separately on ISR and FSR. ISR is implemented in the cross-section calculation using so-called the structure function method for the incoming electron, like parton density functions for the proton, with the formula in the leading-logarithmic approximation [39]. In this calculation, a four-momentum transfer squared on the scattered electron line is used as a QED scale. The correction for the photon self energy, or the vacuum polarization, is included according to the parameterization in [40] which is also a fit to the experimental data. FSR from any final state lepton is performed by `PYTHIA` [41] using the parton shower method.

1130000 events of the QED dilepton process are generated and used, corresponding to a twenty-times more statistics than that of the data.

5.2 The Detector Simulation

Four-momenta, particle ID codes and so on generated by event generators are input into the ZEUS detector simulation program MOZART [24] . MOZART is based on the multipurpose detector simulation tool GEANT [42], and simulates interactions of particles in the detector materials. The trigger decision is simulated by the program CZAR, and the offline event reconstruction, taking all of the calibration constants into account, by ZEPHYR. Therefore, the same condition is applied on both the data and MC events.

Chapter 6

Event Reconstruction

6.1 Event Characteristics

The event sample of this analysis is a subset of the inclusive neutral-current Deep Inelastic Scattering (DIS) sample with Q^2 values below $100\,\mathrm{GeV}^2$. In the Q^2 range, scattered electrons are detected in the RCAL, resulting in a typical characteristic of DIS events, that is a high-energy ($\gtrsim 10\,\mathrm{GeV}$) electromagnetic cluster in the RCAL. Another characteristic of DIS events is seen in the value of the total $E - P_Z$, where $E - P_Z$ is defined as a sum of the energy and the negative longitudinal momentum. From the energy-momentum conservation, the following formulae hold,

$$E_e + E_p = \sum_i E_i \quad \text{and} \tag{6.1}$$

$$P_Z^e + P_Z^p = \sum_i P_Z^i, \tag{6.2}$$

where E_e (P_Z^e) and E_p (P_Z^p) are energies (longitudinal momenta) of the electron and proton beam, respectively, and E_i and P_Z^i are an energy and longitudinal momentum of the final state particle:i. Substracting Eq.(6.2) from Eq.(6.1), the total $E - P_Z$ ($= \sum_i E_i - P_Z^i$) is written as

$$E - P_Z = \sum_i \left(E_i - P_Z^i \right) = 2E_e \tag{6.3}$$

since $E_e \cong -P_Z^e$ and $E_p \cong P_Z^p$. The value of $E_i - P_Z^i$ takes $E_i - P_Z^i \cong 0$ at $\theta \sim 0$ and $E_i - P_Z^i \cong 2E_i$ at $\theta \sim 180^\circ$, where θ_i denotes a polar angle of the particle:i.

Thus, measured values of the total $E - P_Z$ becomes smaller than $2E_e$ if the scattered electron escapes into the beam-pipe hole of the RCAL, and is not detected. Even if the scattered electron is detected, the value of the total $E - P_Z$ can be small in case of the large initial state radiation, where the photons are radiated at $\theta_\gamma \sim 180°$. In this analysis, a cut for the minimum value of the total $E - P_Z$ is applied to suppress radiative effects.

The J/ψ state is observed via its dilepton decay channels: $J/\psi \to l^+l^-$ ($l = e$ or μ), as a peak in the invariant mass spectrum of the dilepton around 3 GeV. Scattered protons escape into the beam-pipe hole of the FCAL with a small scattering angle, so that they are not detected with the detectors used in this analysis.

Figure 6.1-(a) shows an example of the J/ψ signal events from the J/ψ-MC for the di-electron decay channel. The scattered electron is detected in the RCAL. The decay electrons are detected with the CTD, both of which have a matching energy cluster in the BCAL. Those clusters have most of the energy deposits in the EMC section of the BCAL due to the characteristics of electromagnetic showers. Figure 6.1-(b) shows an example for the di-muon decay channel. The scattered electron is also detected in the RCAL. A CTD track is reconstructed for the scattered electron in case of a large scattering angle. The muons penetrate the CAL with the small energy deposits in it due to the characteristics of minimum ionizing particles. The important feature of exclusive production of vector mesons is that there are no other tracks in the CTD and no other significant energy deposits in the CAL.

The center-of-mass energy of the γ^*p system (W) has a strong correlation with the longitudinal momentum of the J/ψ meson, as shown in Figure 6.2, since the γ^*p system boosts in the forward (backward) direction with a lower (higher) W value, as shown in Figure 6.3-(c) (-(a)). Around $W \sim 90$ GeV, J/ψ mesons are produced almost at rest in the laboratory frame apart from the transverse momentum, like the event in Figure 6.3-(b).

In the following sections, the basic methods to reconstruct events with the above-mentioned characteristics are explained.

6.2 Calorimeter Clustering Algorithms

In order to make a correspondence between a final state particle and energy deposits in the CAL, a set of neighboring cells with energy deposits are merged into a cluster according to a certain algorithm. This procedure is called *clustering*. Three different clustering algorithms are used in this analysis: *condensate*, *tower-island* and

(a) $ep \to eJ/\psi\, p,\ J/\psi \to e^+e^-$

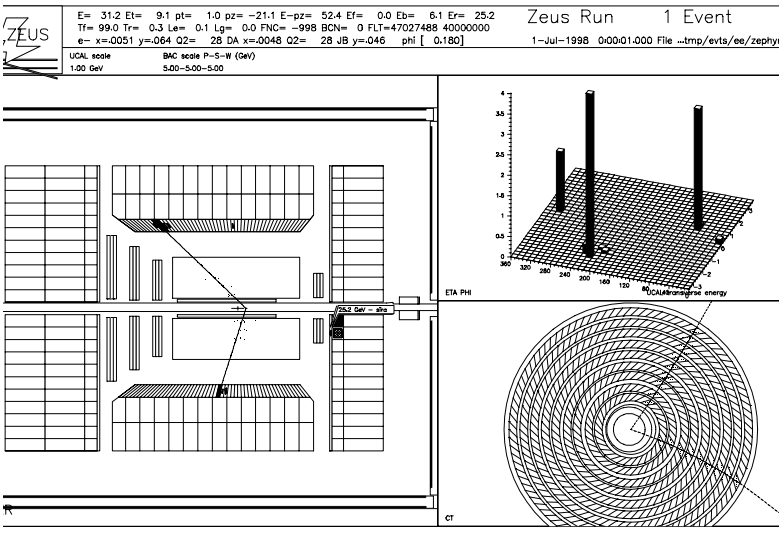

(b) $ep \to eJ/\psi\, p,\ J/\psi \to \mu^+\mu^-$

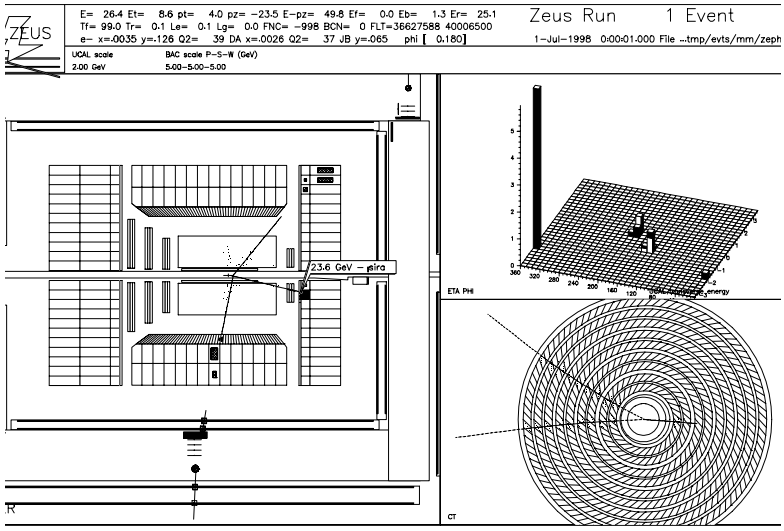

Figure 6.1: *Examples of the J/ψ signal events from the J/ψ-MC for the (a) di-electron and (b) di-muon decay channel.*

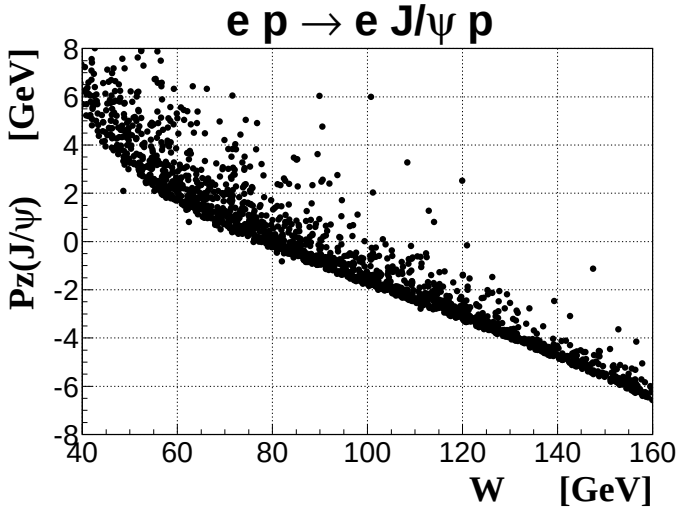

Figure 6.2: *Correlation between W and $Pz(J/\psi)$, where $Pz(J/\psi)$ is a longitudinal momentum of the J/ψ meson.*

cone-island. The detailed explanation is given in Appendix A.

6.3 Noise Suppression for the CAL

In the standard event reconstruction by `ZEPHYR`, energies of the CAL cells are set to zero if they are less than 60 MeV for the EMC cells or 110 MeV for the HAC cells. This is to eliminate a noise originated from the electronics, PMTs and/or the radioactivity of the uranium. The algorithm for further suppressing the remaining noise effects was studied based on data events which were taken randomly [43]. Performing the condensate clustering (Appendix A), isolated cells, which are surrounded by zero-energy cells, are removed if the energy is less than 80 MeV for the EMC cells and 140 MeV for the HAC cells. In order to remove run-by-run "*hot*" cells, the noise status of each cell was investigated for each run. CAL cells are removed if the cell gives a high rate with a certain height of the signal since this is a characteristic of the noise from the electronics. After these noise suppressions, the energy distribution of the cells in the randomly-taken data is well-reproduced by the uranium-noise simulation [43].

(a) $W = 160\,\mathrm{GeV}$

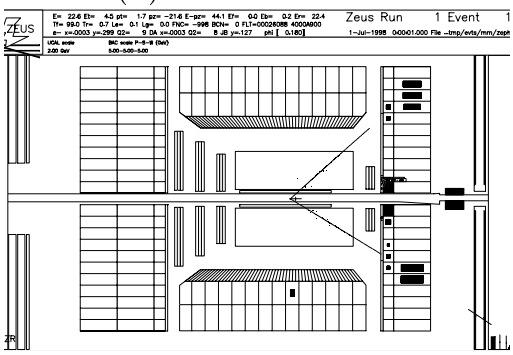

(b) $W = 79\,\mathrm{GeV}$

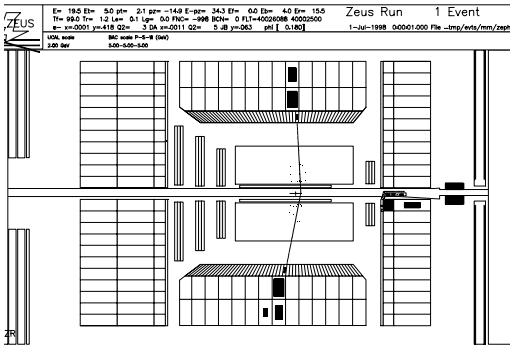

(c) $W = 53\,\mathrm{GeV}$

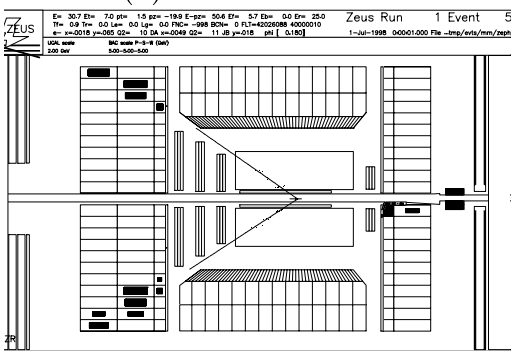

Figure 6.3: *Examples of the J/ψ signal events with the different W values.*

6.4 Finding and Reconstruction of Scattered Electrons

Scattered-electron candidates are searched for in the CAL using a neural-network electron finder which is based on the tower-island clustering [44]. The neural network outputs a probability of the tower-island to be a electromagnetic cluster originated from the incident electron. By setting the standard threshold ($Probability > 0.9$), the finding efficiency is above 99 % for both data and MC in case of the cluster energy larger than 10 GeV [45].

The position of the scattered-electron candidate is firstly reconstructed using the RCAL. The vertical position is determined with the amount of the energy leakage from the highest energy cell to the upper and lower adjacent ones using a logarithmic weight. The horizontal position is calculated from the imbalance between the energies recorded in the right and left PMTs according to the tuned parameterization [46]. Secondly, the corresponding cluster is searched for in the SRTD in order to obtain a better position resolution [47]. If it is found, the SRTD position is used.

The energy of the scattered-electron candidate is measured from the energy of the corresponding tower-island. The measured energy is corrected on the energy loss due to the dead material in front of the RCAL using the SRTD as a presampler if a matching SRTD cluster exists. If not, the dead material map of the detector simulation is used [45, 48]. Note that the energy of the scattered-electron candidate is used only for the total $E - P_Z$ reconstruction.

6.5 Momentum Determination of Decay Leptons

Angles and momenta of the decay leptons are primarily determined with the measured quantities from the CTD. However, for tracks with a low angle, the CTD momentum measurement has a large error as small number of CTD hits are used in the track reconstruction. For di-electron events, the CAL energy measurement could give a better resolution for the low-angle track. For di-muon events, an improvement is achieved by imposing a constraint that the dilepton mass should be the J/ψ mass. The details of the methods are described below.

6.5.1 Using the CAL information (di-electron)

If the CAL cluster, corresponding to the decay lepton, has a large energy (above 1 GeV), it could be used in the kinematics reconstruction. The track momentum of the CTD is compared with the CAL cluster energy which is corrected in the same way as for the scattered electron.

The CTD momentum resolution can be parameterized as functions of p_T, L and N [49, 26, 50] as

$$\frac{\sigma(p_T)}{p_T} = \alpha(L,N)\cdot p_T \oplus \beta \oplus \frac{\eta}{p_T} \tag{6.4}$$

and

$$\alpha(L,N) = \alpha' \cdot \left(\frac{L_0}{L}\right)^2 \cdot \sqrt{\frac{N_0}{N}}, \tag{6.5}$$

where p_T is a transverse momentum of the track. L is the projected length of the track onto the bending plane, L_0 is the projected length of the track penetrating all the SLs (a full length track) onto the bending plane, N is the number of hits used in the reconstruction of the track, and N_0 is the number of hits for the full length track. The values of the parameters: α', β and η for the CTD were derived with MC [26]. They were checked with the J/ψ photoproduction data and MC, and the results were found to be consistent with the former study [50].

The resolution of the CAL cluster is calculated based on Eq.(4.3).

When the resolution of the cluster energy is better than that of the CTD track, the cluster energy is used to estimate the electron momentum instead of the track momentum in case of the di-electron channel. The angles are measured with the CTD.

6.5.2 Using the $M_{J/\psi}$ constraint (di-muon)

In case that one of the two CTD tracks from the decay muons has a bad resolution, the momentum is derived from the other muon using the opening angle of the di-muon and the constraint of $M_{l^+l^-} \equiv M_{J/\psi}$. The following is the mathematical explanation on this method.

From the 4-momentum conservation, the following equation holds,

$$M^2_{J/\psi} = 2m^2_\mu + 2(\sqrt{P^2_{\mu^+} + m^2_\mu}\sqrt{P^2_{\mu^-} + m^2_\mu} - P_{\mu^+}P_{\mu^-}cos\Theta), \tag{6.6}$$

where Θ is the opening angle of the di-muon, P_{μ^+} and P_{μ^-} are momenta of μ^+ and μ^-, respectively, and m_μ is the mass of the muon. For the fixed Θ and P_{μ^-} values, Eq. (6.6) can be regarded as a quadratic equation on P_{μ^+}. The solution, which is used in this analysis, is

$$P_{\mu^+} = \frac{AB + \sqrt{m_\mu^2(A^2-1)+B^2}}{1-A^2} \quad \Big(\equiv m(P_{\mu^-})\Big), \tag{6.7}$$

where A and B are defined as

$$A = \frac{P_{\mu^-} cos\Theta}{\sqrt{P_{\mu^-}^2 + m_\mu^2}} \quad \text{and} \tag{6.8}$$

$$B = \frac{M_{J/\psi}^2 - 2m_\mu^2}{2\sqrt{P_{\mu^-}^2 + m_\mu^2}}. \tag{6.9}$$

For a kinematical variable F as a function of (P_{μ^+}, P_{μ^-}), the error of the measurement (ΔF) can be estimated according to the following formula,

$$\Delta F \cong \sqrt{\left(\frac{\partial f}{\partial P_{\mu^+}}\Delta P_{\mu^+}\right)^2 + \left(\frac{\partial f}{\partial P_{\mu^-}}\Delta P_{\mu^-}\right)^2}, \tag{6.10}$$

where contributions from other quantities are assumed to be zero or negligible.

Calculating P_{μ^+} from P_{μ^-} using Eq. (6.7), a formula to estimate the measurement error on the variable F as a function of P_{μ^-} is obtained,

$$\Delta F_- \cong \left|\frac{\partial f}{\partial P_{\mu^-}} + \frac{\partial f}{\partial P_{\mu^+}}\frac{dm(P_{\mu^-})}{dP_{\mu^-}}\right|\Delta P_{\mu^-}, \tag{6.11}$$

and in its inverse case, the formula takes the form of

$$\Delta F_+ \cong \left|\frac{\partial f}{\partial P_{\mu^+}} + \frac{\partial f}{\partial P_{\mu^-}}\frac{dm(P_{\mu^+})}{dP_{\mu^+}}\right|\Delta P_{\mu^+}, \tag{6.12}$$

where ΔF_- (ΔF_+) is the error estimate on F in case that P_{μ^-} (P_{μ^+}) is used in the calculation of F. Therefore, the momentum of P_{μ^-} (P_{μ^+}) is used if $\Delta F_- < \Delta F_+$ $(\Delta F_- > \Delta F_+)$ holds.

This method is applied after the cut for the J/ψ mass window. Figure 6.4 shows the resolution of the W reconstruction with and without this method. A significant improvement is seen. The method of the W reconstruction will be described in the next section.

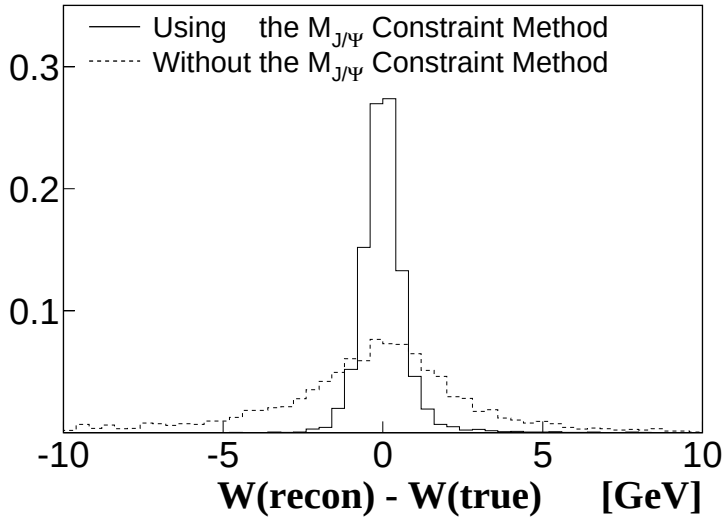

Figure 6.4: *Resolution on the W reconstruction with and without the $M_{J/\psi}$ constraint method, estimated with the $J/\psi \to \mu^+\mu^-$ MC events in the kinematical range of $10 < Q^2 < 40\ GeV^2$ and $140 < W < 160\ GeV$.*

6.6 Kinematics Reconstruction

There exist various methods in the reconstruction of the kinematical variables for ep scattering (for example, see [51].). Although those are equivalent at the Born level, reconstructed variables, in actual data analyses, are differently affected by the photon radiation and the detector resolutions and migrations.

In this analysis, a method using the kinematical constraint on the total $E - P_Z$ [52, 3] is used. The advantage of this method is not using the energy of the scattered electron except for $E - P_Z$ itself, which leads to good resolutions for the reconstructed kinematical variables.

The following is the derivation of the $E - P_Z$ constraint method on the process: $e\ p \ \to \ e\ N\ l\,l$, where ll indicates a dilepton. Using the total $E - P_Z$ conservation (Eq.(6.3)), the energy of the scattered electron ($E_{e'}$) is calculated from the polar angle ($\theta_{e'}$) and the $E - P_Z$ of the dilepton system $\left((E - P_Z)_{ll}\right)$ as

$$E_{e'} = \frac{2\,E_e^{beam} - (E - P_Z)_{ll} - (E - P_Z)_N}{1 - cos\theta_{e'}} \tag{6.13}$$

$$\cong \frac{2\,E_e^{beam} - (E - P_Z)_{ll}}{1 - cos\theta_{e'}}, \tag{6.14}$$

where E_e^{beam} indicates the energy of the electron beam, and $(E - P_Z)_N$ denotes the

$E - P_Z$ value for the system N. The maximum value of $(E - P_Z)_N$ is less than $4\,\mathrm{MeV}$ for $|t| \lesssim 1\,\mathrm{GeV}^2$ since $(E - P_Z)_N$ is expressed as

$$(E - P_Z)_N \cong \frac{|t| + M_N^2 + M_p^2}{2\,E_p^{beam}} \tag{6.15}$$

in case of $E_p^{beam} \gg M_p$. On the contrary, the minimum value is above $600\,\mathrm{MeV}$ for $(E - P_Z)_{l\,l}$ in the kinematical region of this analysis, so that $(E - P_Z)_N$ is negligible in Eq. (6.13). Q^2 is calcualted using the above $E_{e'}$ as

$$Q^2 = 2\,E_e^{beam}\,E_{e'}\,(1 + cos\theta_{e'}). \tag{6.16}$$

$|t|$ is also calculated using the above $E_{e'}$ as

$$\begin{aligned} |t| &= \left(P_N - P_p\right)^2 && (6.17)\\ &\cong \left(E_{e'}\sin\theta_{e'}\cos\phi_{e'} + P_X^{l\,l}\right)^2 + \left(E_{e'}\sin\theta_{e'}\sin\phi_{e'} + P_Y^{l\,l}\right)^2, && (6.18) \end{aligned}$$

where $\phi_{e'}$ indicates the azimuthal angle of the scattered electron, and $\vec{P}^{l\,l} = (P_X^{ll}, P_Y^{ll}, P_Z^{ll})$ is the 3-momentum vector of the dilepton system. The kinematical variables, y, W and x are calculated as

$$\begin{aligned} y &= \frac{P_p \cdot q_{\gamma^*}}{P_p \cdot k} = \frac{P_p \cdot (P_N + P_{l\,l} - P_p)}{P_p \cdot k} && (6.19)\\ &\cong \frac{(E - P_Z)_{l\,l}}{2\,E_e^{beam}}, && (6.20)\\ W^2 &= P_N^2 = \left(P_p + q_{\gamma^*}\right)^2 && (6.21)\\ &= M_p^2 + q_{\gamma^*}^2 + 2\,(P_p \cdot q_{\gamma^*}) && (6.22)\\ &\cong y \cdot s - Q^2 + M_p^2 \quad \text{and} && (6.23)\\ x &= \frac{Q^2}{y \cdot s}. && (6.24) \end{aligned}$$

The approximation as used in Eq. (6.14) is used also in Eqs. (6.20) and (6.23). In summary, the $E - P_Z$ constraint-method variables: Q_{ct}^2, $|t_{ct}|$, y_{ct}, W_{ct} and x_{ct} are defined as

$$\begin{aligned} Q_{ct}^2 &= 2\,E_e^{beam}\,E_{e'}^{ct}\,(1 + cos\theta_{e'}), && (6.25)\\ |t_{ct}| &= \left(E_{e'}\sin\theta_{e'}\cos\phi_{e'} + P_X^{l\,l}\right)^2 + \left(E_{e'}\sin\theta_{e'}\sin\phi_{e'} + P_Y^{l\,l}\right)^2, && (6.26)\\ y_{ct} &= \frac{(E - P_Z)_{l\,l}}{2\,E_e^{beam}}, && (6.27)\\ W_{ct}^2 &= y_{ct} \cdot s - Q_{ct}^2 + M_p^2, \quad \text{and} && (6.28)\\ x_{ct} &= \frac{Q_{ct}^2}{y_{ct} \cdot s} = \frac{Q_{ct}^2}{Q_{ct}^2 + W_{ct}^2 - M_p^2}, && (6.29) \end{aligned}$$

where

$$E_{e'}^{ct} = \frac{2\,E_e^{beam} - (E - P_Z)_{ll}}{1 - cos\theta_{e'}}. \tag{6.30}$$

The above kinematical variables are calculated from the polar angle of the scattered electron and the $E - P_Z$ of the dilepton system.

Chapter 7

Event Selection

This analysis is based on the ZEUS data with an integrated luminosity of $90.3\,\mathrm{pb}^{-1}$ taken in 1996-2000. The event sample is divided into two: "*the Medium-W sample*" and "*the High-W sample*". The medium-W sample consists of events with the W range of $50 \lesssim W \lesssim 150\,\mathrm{GeV}$, and is based on two CTD-tracks corresponding to the decay dilepton from the J/ψ meson. The high-W sample consists of di-electron events with the W range of $150 \lesssim W < 220\,\mathrm{GeV}$, and includes not only events based on two CTD tracks but also events with only one track corresponding to the decay electron. In this chapter, the detailed description of the event selection is presented.

7.1 Outline of the Event Selection

The offline event selection consists of the following four steps:

(1) the scattered-electron finding,

(2) the dilepton selection after removing objects related to the scattered-electron candidate,

(3) the elasticity requirement after removing objects related to the dilepton candidate, and

(4) the limitation of the kinematical region.

As a basic requirement, a primary vertex is always imposed to be reconstructed by the CTD in a reasonable region defined as $|Z_{VTX}| < 50\,\mathrm{cm}$ and $\sqrt{X_{VTX}^2 + Y_{VTX}^2} < 5\,\mathrm{cm}$ where $(X_{VTX}, Y_{VTX}, Z_{VTX})$ is a position of the reconstructed primary vertex.

The event selection is summarized in Table 7.1.

	Selection cuts		
(0) Trigger	$E_e > 5\,\mathrm{GeV}$ Simple box cut ($6\times12\,\mathrm{cm}^2$) $E - P_Z > 30\,\mathrm{GeV}$ $0 <$ (# of CTD tracks) < 6 Small energy around the FCAL beam-pipe hole etc.		
(1) Scattered electron finding	$E_e > 10\,\mathrm{GeV}$ H-shaped box cut etc.		
(2) Dilepton selection	Decay tracks with $19.72^\circ < \theta_{trk} < 160.28^\circ$ and $P_T^{trk} > 0.2\,\mathrm{GeV}$, etc.		
	e^+e^-: EMC-fraction > 0.9 (# of decay tracks) = 1 or 2 etc.	$\mu^+\mu^-$: EMC-fraction < 0.6 (# of decay tracks) = 2 etc.	
(3) Elasticity cuts	No CAL-cluster with $E_{clus} > 300\,\mathrm{MeV}$ At most one EMC-cluster with $E_{clus} > 150\,\mathrm{MeV}$		
(4) Kinematical cuts [GeV]	$50 \lesssim W_{ct} \lesssim 150$ (# of decay tracks)=2	$150 \lesssim W_{ct} < 220$	
Mass window [GeV]	2.6 - 3.4	2.6 - 3.5	2.8 - 3.4
	$2 < Q^2_{ct} < 100\,\mathrm{GeV}^2$ $\lvert t_{ct}\rvert < 1\,\mathrm{GeV}^2$ $E - P_Z > 45\,\mathrm{GeV}$		
			$50 \lesssim W_{ct} \lesssim 150\,\mathrm{GeV}$

Table 7.1: *Summary of the event selection. Only the major cuts are written in (0)-(2). In the above table, E_e denotes an energy of the scattered electron candidate, θ_{trk} and P_T^{trk} are the polar angle and transverse momentum of the CTD track, and E_{clus} indicates an energy of the calorimeter cluster.*

7.2 Trigger

The trigger is based on the following three requirements:

- electromagnetic energy deposits in the RCAL with the energy threshold of 5 GeV to catch the scattered electron,
- the low track-multiplicity in the CTD to select dilepton events, and
- no significant energy deposits around the beam-pipe hole of the FCAL to select exclusive processes.

In the following offline selection, the tighter cuts are applied than the trigger, so that the relative trigger efficiency of this trigger to the final events passing all the offline selection cuts is close to 100 %. The detailed description of the trigger logic is described in Appendix B

7.3 Scattered-electron Finding

A scattered electron candidate is searched for in the CAL using the method described in § 6.4 (p.52). If there are more than one candidates found, the most energetic one is selected. For the selected candidate, the energy is required to be larger than 10 GeV and to be in the RCAL.

The reconstructed position is required to be away from the beam-pipe hole of the RCAL. One of the reasons is to avoid a low efficiency of the electron finding due to the energy leakage to the beam-pipe hole. Another reason is that there is a region where MC cannot reproduce the amount of the pre-shower due to the large amount of the inactive materials before the RCAL which has not yet been correctly implemented in the detector simulation [45, 48]. In order to avoid such effects, an *H-shaped box cut*, as shown in Figure 7.1 as a hatched area, is applied for the cluster position reconstructed with the SRTD:

- $\{|X_e| > 14\,\mathrm{cm}$ or $|Y_e| > 11\,\mathrm{cm}\}$ or
- $\{-7 < X_e < 4\,\mathrm{cm}$ and $7 < Y_e < 11\,\mathrm{cm}\}$ or
- $\{-7 < X_e < 4\,\mathrm{cm}$ and $-11 < Y_e < -7\,\mathrm{cm}\}$ or
- $\{13 < X_e < 14\,\mathrm{cm}$ and $|Y_e| < 11\,\mathrm{cm}\}$,

where (X_e, Y_e) indicates the reconstructed position in the $X - Y$ plane. For the position reconstructed with the CAL, a larger simple box cut is applied due to the cell structure of the RCAL: $|X_e| > 14\,\mathrm{cm}$ or $|Y_e| > 11\,\mathrm{cm}$. The H-shaped box cut

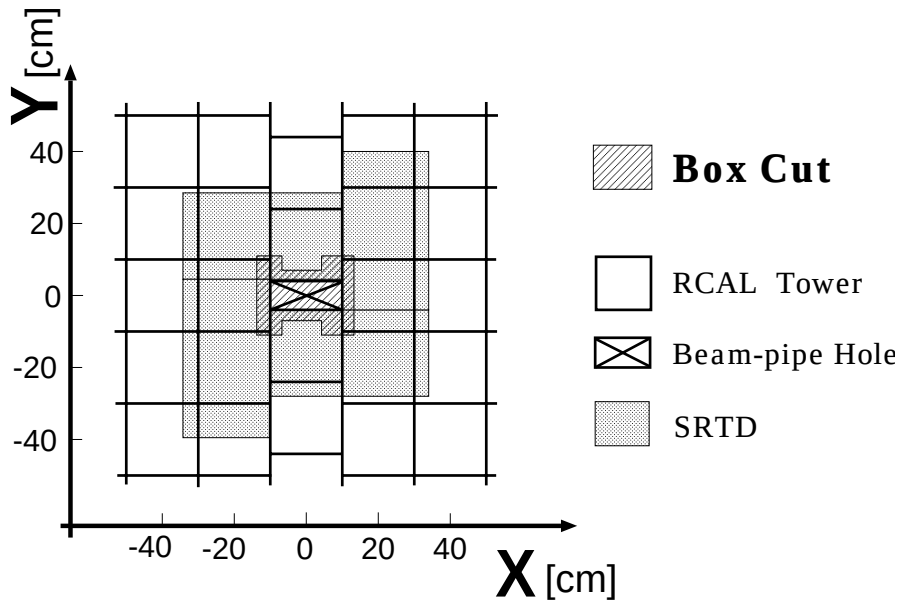

Figure 7.1: *A sketch of the box cut together with the RCAL towers, the beam-pipe hole and the SRTD.*

is referred simply as *the box cut* hereafter.

In case of a large scattering angle, a matching CTD track is reconstructed. Therefore, when the straight line from the primary vertex to the scattered electron position passes the center layer of the SL3, the scattered electron candidate is required to have a matching track with an transverse momentum larger than 0.3 GeV and a distance of the closest approach less than 15 cm. If more than one CTD tracks satisfy the criteria, the closest one is selected.

7.4 Dilepton Selection

7.4.1 Track selection for decay leptons

The dilepton selection starts with finding CTD tracks corresponding to the decay lepton from the J/ψ meson. The tracks should satisfy the following conditions.

- The track is not the matching track to the scattered electron candidate.
- (a) $|\phi_{trk} - \phi_e| > 11°$, where ϕ_{trk} and ϕ_e are azimuthal angles of the track and the scattered electron candidate, respectively, or (b) the track has CTD hits in the SL outside the scattered electron candidate in the radial direction.
- The track should not point the region defined as $|X| < 13\,\mathrm{cm}$ and $Y > 99\,\mathrm{cm}$

at the RCAL surface. In this region, the EMC sections are missing due to the liquid helium feed for the superconducting solenoid.

- The transverse momentum is larger than 0.2 GeV and the polar angle is in the range of $19.72^\circ < \theta < 160.28^\circ$. This condition corresponds to the requirement of the track to pass through the center layer of the SL3.
- The outermost SL with hits is SL3 or outer SL.
- The track is fitted to the primary vertex.

The number of CTD tracks satisfying the above conditions, referred as "*decay tracks*" hereafter , is required to be one or two. In case that the number of decay tracks is two, opposite charges are required. The remaining events are classified into

- **the ONE-track sample** and
- **the TWO-track sample**

according to the number of decay tracks. Those two samples are treated differently as described in the following sections.

7.4.2 Search for matching clusters in the calorimeter

After the scattered-electron finding, the CAL cells belonging to the tower-island of the scattered-electron candidate are removed. Then cone-island clustering is done with the remaining CAL cells.

For the decay track which reaches the CAL surface, matching cone-islands are searched for among those cone-islands by requiring a distance of the closest approach (DCA) less than 30 cm. All of the cone-islands with DCA < 30 cm forms a matching cluster for each decay track. Figure 7.2 shows DCA distributions, in unit of cm, for the data and MC. Samples are divided into 14 regions according to the polar angle of the decay track. For the events in Figure 7.2, the following cleaning cuts are imposed after the decay track selection: only two CTD tracks both of which are fitted to the primary vertex, an invariant mass reconstructed with the two tracks to be in the J/ψ mass range of $2.8 < M_{J/\psi} < 3.4$ GeV, and an energy in the FCAL towers neighboring to the beam-pipe hole to be less than 1 GeV.

For the two-track sample, a decay track with the higher momentum is required to have a matching cluster, as it will be used in the lepton identification. One or more matching cone-island(s) are merged into one matching cluster for each decay track.

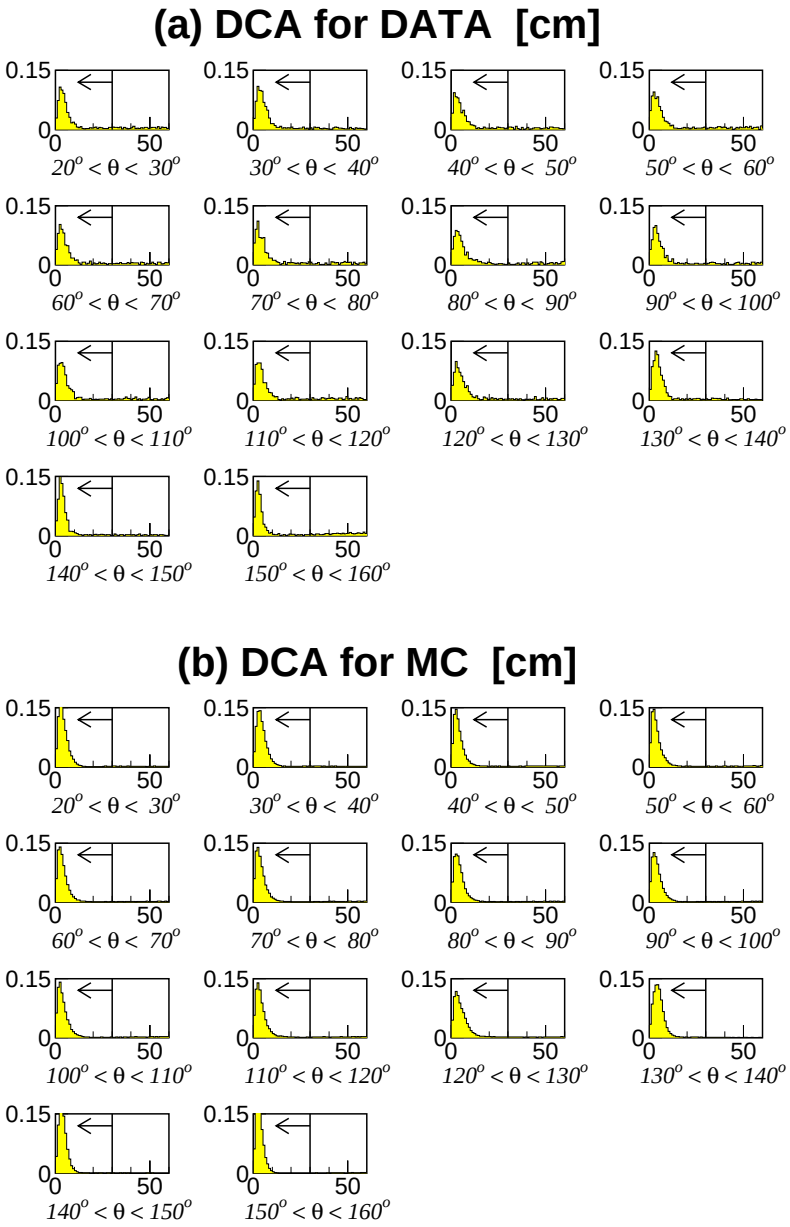

Figure 7.2: *Distributions of the distance of the closest approach (DCA) of decay tracks to cone-islands in unit of cm for (a) data and (b) MC. Samples are divided into 14 regions according to the polar angle of the decay track, specified below the histograms. Some cleaning cuts are imposed after the decay track selection described in the text.*

7.4.3 Lepton identification for the two-track sample

The lepton identification is performed in order to separate the di-electron and di-muon channels and to remove pion backgrounds. The lepton identification is based on the CAL only. Finally the lepton mass is assigned and used in the kinematics calculation.

The criterion is mainly based on the fraction of the energy in the EMC section to the total for the matching cluster with the higher-momentum decay track. The value is set to zero when the decay track does not have a matching cluster. The two-track events are classified into

- di-electron candidates for $\hat{F}_{EMC}^{clus} > 0.9$ and
- di-muon candidates for $\hat{F}_{EMC}^{clus} < 0.6$,

where $\hat{F}_{EMC}^{clus}$ is the abovementioned fraction. Events with $0.6 < \hat{F}_{EMC}^{clus} < 0.9$ are regarded as pion backgrounds, and are rejected. Figure 7.3 shows $\hat{F}_{EMC}^{clus}$ distributions for the data and MC after the decay track selection and the cleaning cuts as used in Figure 7.2. A distinct difference is observed on the peak positions of the di-electron and di-muon samples. The distribution for the $\pi^+\pi^-$ MC is relatively flat, which is the reason for rejecting events with $0.6 < \hat{F}_{EMC}^{clus} < 0.9$.

For the di-electron candidates with matching clusters for both decay tracks, the fraction of the energy in the EMC section to the total for the matching cluster with the lower-momentum decay track is required to be larger than 0.9 if the cluster has an energy greater than 0.2 GeV.

For the di-muon candidates, the following requirement is imposed to assure the MIP-like features:

- $\frac{E_{clus}^{CAL}}{\lambda_{CAL}} < 0.5\,\mathrm{GeV}$ and $\frac{E_{clus}^{EMC}}{\lambda_{EMC}} < 0.8\,\mathrm{GeV}$ for both of μ^+ and μ^- candidates, and
- $E_{clus}^{HAC2}(\mu^+) + E_{clus}^{HAC2}(\mu^-) > 0.2\,\mathrm{GeV}$,

where E_{clus}^{CAL}, E_{clus}^{EMC} and E_{clus}^{HAC2} are energies of the matching clusters in the CAL, EMC and HAC2+RHAC1 section, respectively, and λ_{CAL} (λ_{EMC}) is an interaction length of the CAL (EMC) along the muon direction.

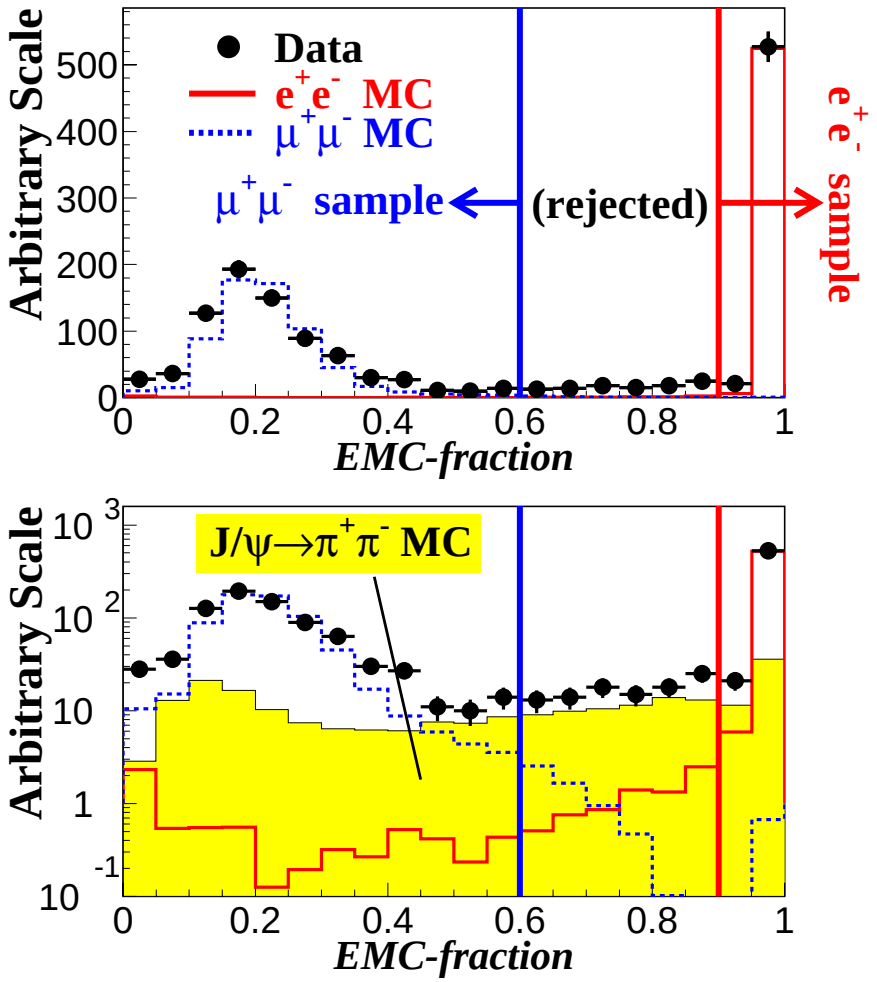

Figure 7.3: *Distributions of $\hat{F}^{clus}_{EMC}$ for the data and MC after the decay track selection and the cleaning cuts. Histograms are in the linear scale in the top and in the logarithmic scale in the bottom. The solid histogram indicates the $J/\psi \to e^+e^-$ MC and the dashed one for the $J/\psi \to \mu^+\mu^-$ MC. The $J/\psi \to \pi^+\pi^-$ MC is the $J/\psi \to \mu^+\mu^-$ MC with muons replaced by pions before the detector simulation. Individual normalizations of those histograms are taken arbitrarily.*

7.4.4 Selection of the second decay electron in the one-track sample

The one-track sample is used only for the di-electron channel because CTD track momenta of both decay leptons are necessary to calculate an invariant mass of the dilepton. The measurement with this sample is limited in the high-W region in this analysis. In that case, one of the decay electrons tends to enter the RCAL close to the beam-pipe hole, so that it might miss a matching CTD track. The decay electron, which is not measured as a decay track, is hereafter referred as "*the second decay electron*".

The second decay electron is searched for in the RCAL among the cone-islands except for ones matching to the decay track. The candidate is required to have

- an energy larger than 2 GeV in order to keep a reliable position measurement with the RCAL,
- the reconstructed position outside the box cut,
- the polar angle larger than 160.28°, i.e., outside the CTD acceptance region for decay tracks.
- a fraction of the energy in the EMC section to the total larger than 0.9 to select a di-electron event, and
- the number of CAL cells in the following range, as shown in Figure 7.4 with a bold line:
  - ▷ $N_{cells} \leq 4$ for $2 < E_{clus} < 4\,\mathrm{GeV}$,
  - ▷ $N_{cells} \leq 5$ for $4 < E_{clus} < 6\,\mathrm{GeV}$,
  - ▷ $N_{cells} \leq 6$ for $6 < E_{clus} < 8\,\mathrm{GeV}$,
  - ▷ $N_{cells} \leq 7$ for $8 < E_{clus} < 10\,\mathrm{GeV}$,
  - ▷ $N_{cells} \leq 8$ for $E_{clus} > 10\,\mathrm{GeV}$,

  where N_{cells} is the number of cells and E_{clus} is the energy of the cluster.

The last requirement on N_{cell} is for suppressing backgrounds accompanied by multi-pion. In case that more than one cone-islands satisfy the above criteria, the event is rejected.

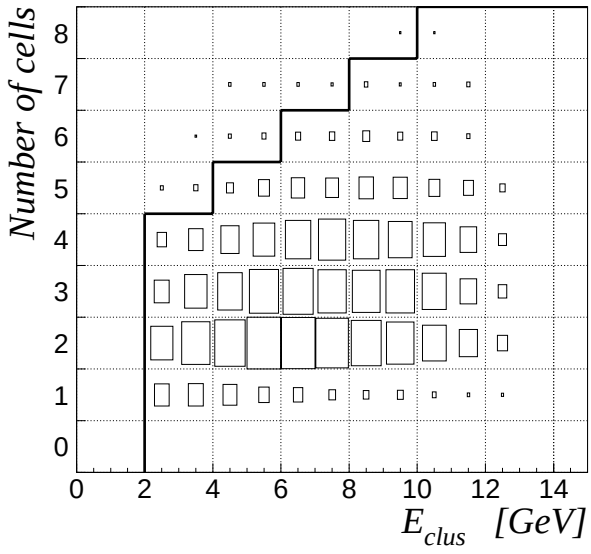

Figure 7.4: *A 2-dimensional histogram on the energy of the cluster (E_{clus}) and the number of constituent CAL cells for the one-track sample from the $J/\psi \to e^+e^-$ MC. The bold line indicates a cut on the number of cells described in the text. The cut of $E_{clus} > 2\,GeV$ was already applied.*

7.5 Elasticity Requirement

At this stage, there are various background events accompanied with additional particles even in the J/ψ mass range, especially the proton dissociative J/ψ production where the proton breaks up, and the excited state of J/ψ production like $J/\psi(2S) \to J/\psi\,\pi\pi$. In order to suppress such kind of events, it is required that events have neither additional vertex-fitted tracks in CTD nor additional energy deposits in the CAL. In the latter case, cone-islands with an energy above 300 MeV are regarded as an additional particle and events with at least one such a cone-island are rejected. Furthermore, in order to suppress events with soft multi-π^0 like $J/\psi(2S) \to J/\psi\,\pi^0\pi^0$ production, events with two or more cone-islands which have an energy above 150 MeV only in the EMC section larger than 0.9 are rejected.

It has been checked, using events taken randomly, that the fake rejection fraction due to the noise and/or the event overlap is less than 1% and almost constant throughout the data taking periods from 1996 to 2000.

As the FPC has been installed since 1998, so that the energy from the FPC is required to be less than 1 GeV for events taken in 1998-2000. This energy threshold was determined taking the effects of the noise and the pile-up into account [53].

7.6 Kinematical Acceptance

The measured kinematical region for Q^2_{ct} and W_{ct} is limited where the acceptance is high in order to avoid a large acceptance correction which leads to a large uncertainty in the cross-section measurement. The region is determined mainly from the geometrical acceptance of the ZEUS detector for the J/ψ electroproduction. In this section, the kinematical region of this measurement is defined by investigating the acceptance as functions of Q^2_{ct} and W_{ct}.

The acceptance is defined as

$$\frac{\textit{Number of events generated in the bin AND passing the event selection}}{\textit{Number of events generated in the bin}}. \quad (7.1)$$

Figure 7.5 shows the acceptance on the scattered-electron finding as a function of $Q^2_{ct}(true)$[1] estimated with the J/ψ MC. All other cuts are applied on the denominator in (7.1). The dip around $5\,\mathrm{GeV}^2$ corresponds to the four corners of the box cut (Figure 7.1). A cut for the minimum is applied close to the end of the first rising. The Q^2_{ct} region of this measurement is determined as

$$2 < Q^2_{ct} < 100\,\mathrm{GeV}^2. \quad (7.2)$$

The upper limit comes from the statistics of the data.

Figure 7.6 shows the acceptance on the dilepton selection for the two-track sample as functions of $Q^2_{ct}(true)$ and $W_{ct}(true)$ estimated with the J/ψ MC. The W_{ct} region with a high acceptance is shifted as Q^2_{ct} increases. This is due to the change of the J/ψ direction with respect to Q^2_{ct} at the same W_{ct}. The choice of the W_{ct} range is shown in Figure 7.6 as the area surrounded by the bold lines:

$$45 < W_{ct} < 140\,\mathrm{GeV} \quad \text{for} \quad 2 < Q^2_{ct} < 5\,\mathrm{GeV}^2, \quad (7.3)$$

$$50 < W_{ct} < 150\,\mathrm{GeV} \quad \text{for} \quad 5 < Q^2_{ct} < 10\,\mathrm{GeV}^2, \quad (7.4)$$

$$55 < W_{ct} < 160\,\mathrm{GeV} \quad \text{for} \quad 10 < Q^2_{ct} < 40\,\mathrm{GeV}^2, \quad (7.5)$$

$$60 < W_{ct} < 180\,\mathrm{GeV} \quad \text{for} \quad 40 < Q^2_{ct} < 100\,\mathrm{GeV}^2. \quad (7.6)$$

The above division with respect to Q^2_{ct} comes from the bin definition on Q^2_{ct} described in the next chapter. The acceptance in the above region is more than 50 % everywhere and at most around 90 % at $W \cong 90\,\mathrm{GeV}$.

The following kinematical cuts are further applied,

[1] The word '*true*' denotes a value at the generator level.

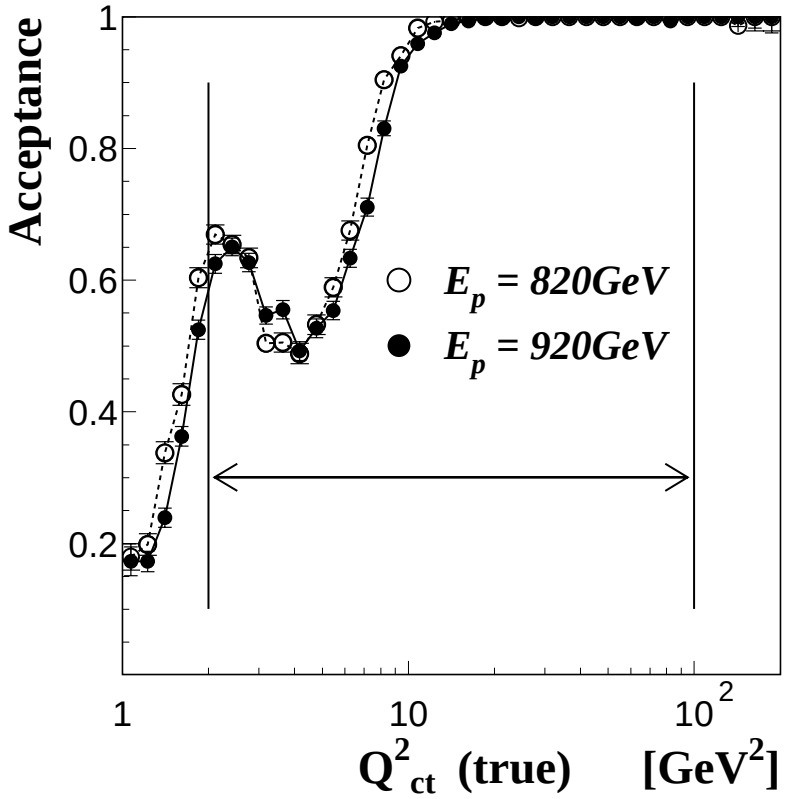

Figure 7.5: *Kinematical acceptance on the scattered-electron finding as a function of Q^2_{ct} estimated with the J/ψ MC. Two cases are shown with 820 GeV (open circles) and 920 GeV (closed circles) proton energies. The vertical lines indicate the Q^2_{ct} region of this measurement.*

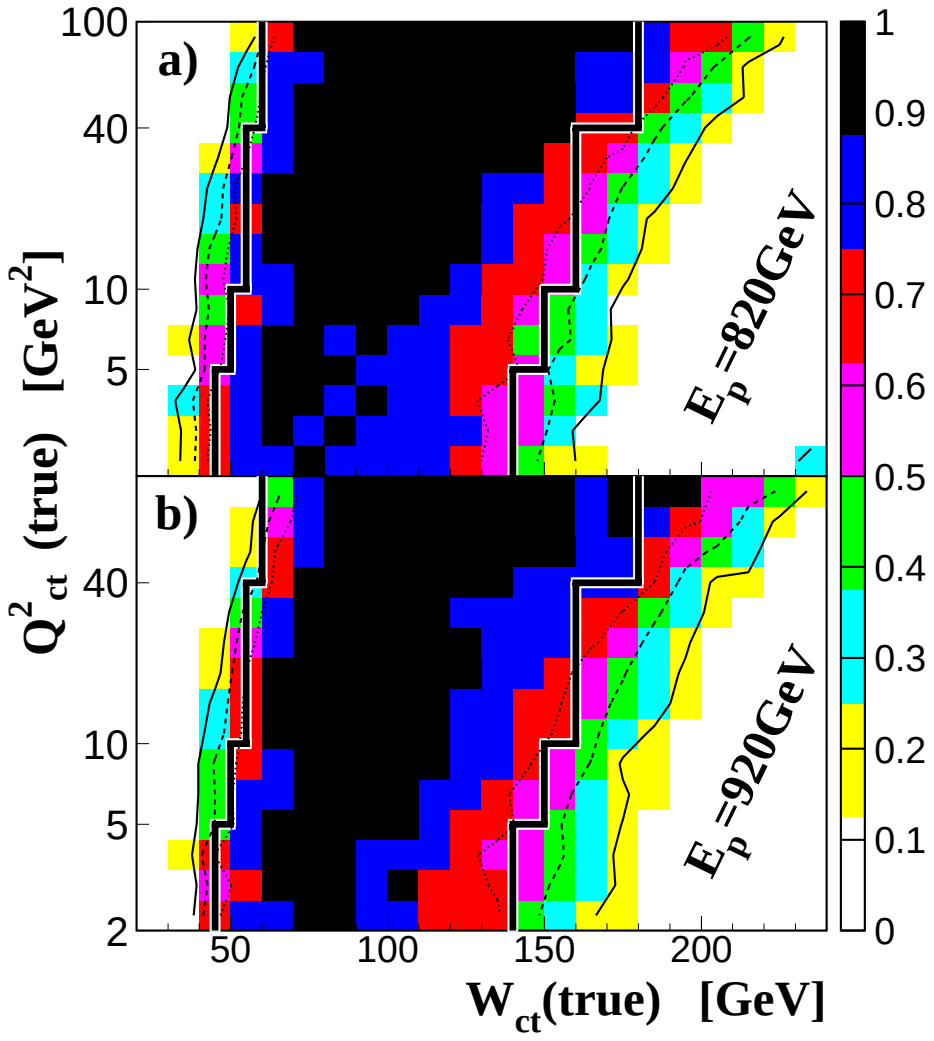

Figure 7.6: *Kinematical acceptance on the dilepton selection for the two-track sample as functions of Q^2_{ct} and W_{ct} with a) 820 GeV in 1996-97 or b) 920 GeV in 1998-00 proton-beam energy. The thin solid line indicates the contour of Acceptance = 0.2, and the dashed, dotted ones for 0.4, 0.6, respectively. The W_{ct} region of this measurement is shown as an area surrounded by the bold lines.*

- $|t_{ct}| < 1\,\mathrm{GeV}^2$ and
- $(E - P_z)_{e'} + (E - P_z)_{ll} > 45\,\mathrm{GeV}$.

The first cut in the above selection is to select a region where exclusive production is dominated. The second cut is to reduce radiative events.

The cuts of Ineqs.(7.3)–(7.6) defines the medium-W region. The high-W sample, which consists of the one- and two-track sample of di-electron candidates, is defined as events passing the following cuts,

$$140 < W_{ct} < 220\,\mathrm{GeV} \quad \text{for} \quad 2 < Q^2_{ct} < 5\,\mathrm{GeV}^2, \tag{7.7}$$

$$150 < W_{ct} < 220\,\mathrm{GeV} \quad \text{for} \quad 5 < Q^2_{ct} < 10\,\mathrm{GeV}^2, \tag{7.8}$$

$$160 < W_{ct} < 220\,\mathrm{GeV} \quad \text{for} \quad 10 < Q^2_{ct} < 40\,\mathrm{GeV}^2, \tag{7.9}$$

where the upper limit is set with the following consideration. Figure 7.7 shows the difference between the energy for the scattered electron and the energy for the decay electron. Energies of the decay electron are higher than those of the scattered electron at $W_{ct} \gtrsim 230\,\mathrm{GeV}$. Since the used algorithm in the scattered-electron finding is that the highest-energy tower-island is regarded as a scattered electron, measurements cannot be done in the region of $W_{ct} \gtrsim 240\,\mathrm{GeV}$.

7.7 The J/ψ Mass Windows

Figure 7.8-(a), (b) and (c) show invariant mass distributions of the di-electron and di-muon candidates in the medium-W region and of the di-electron candidate in the high-W region after all of the above cuts, respectively. The data are compared with the J/ψ-MC after tuning its parameters. The tuning procedure will be explained in § 7.8. The J/ψ mass windows are defined, as drawn in Figure 7.8 with the solid vertical lines,

$$2.6 < M_{e^+e^-} < 3.4\ \mathrm{GeV} \quad \text{for the medium−W sample,} \tag{7.10}$$

$$2.8 < M_{\mu^+\mu^-} < 3.4\ \mathrm{GeV} \quad \text{for the medium−W sample,} \tag{7.11}$$

$$2.6 < M_{e^+e^-} < 3.5\ \mathrm{GeV} \quad \text{for the high−W sample.} \tag{7.12}$$

where $M_{e^+e^-}$ and $M_{\mu^+\mu^-}$ are invariant masses of the di-electron and di-muon candidate, respectively.

The final data sample consists of the di-electron and di-muon candidates in the medium-W region with 615 and 776 events, respectively, and the di-electron candidates in the high-W region with 258 events.

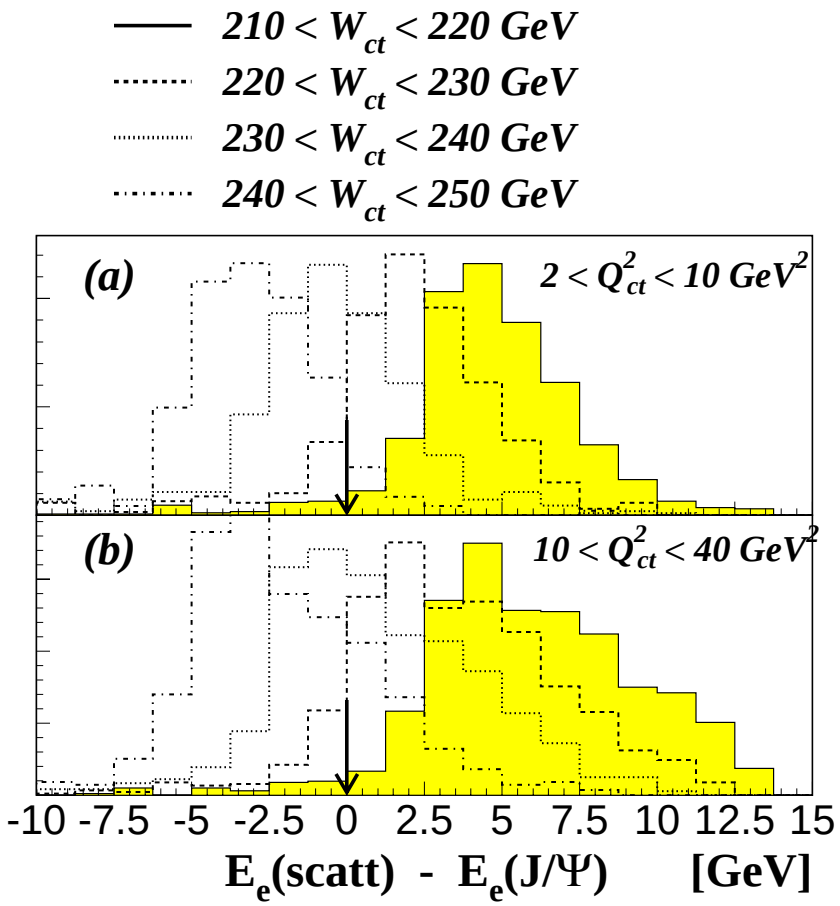

Figure 7.7: *The difference between the energy for the scattered electron and the energy for the decay electron at the generator level. The distribution for* $210 < W_{ct} < 220\ GeV$ *is shown with a shaded histogram.*

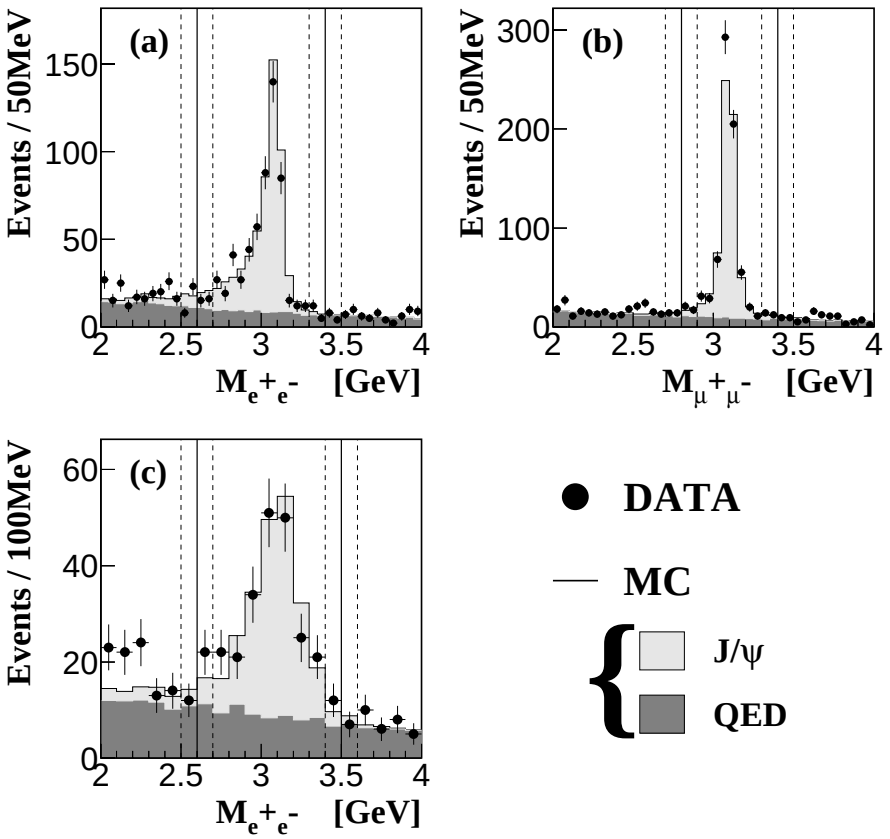

Figure 7.8: *Invariant mass distributions of the (a) di-electron and (b) di-muon in the medium-W region ($50 \lesssim W_{ct} \lesssim 150$ GeV), and of (c) di-electron in the high-W region ($150 \lesssim W_{ct} < 220$ GeV). The data are not corrected for the detector effects. The J/ψ-MC have been tuned as described in §7.8. The solid histograms indicate the total MC including the J/ψ (lightly-shaded) and QED (darkly-shaded) processes. The surrounded regions with the two vertical lines are the J/ψ mass windows; solid ones for the nominal cuts and dashed ones for the systematic check. The magnitude of the cross section of the J/ψ-MC is normalized to the sum of the data events in the mass windows on e^+e^- and $\mu^+\mu^-$ in (a), (b), and normalized to only e^+e^- in (c). On the other hand, the magnitude of the QED-MC is taken from the prediction from* `GRAPE` *which simulates both of the exclusive and proton-dissociative QED processes.*

7.8 Tuning of the Parameters in the J/ψ-MC

The J/ψ-MC is tuned to describe the data in order to obtain a correct estimate on the acceptance which will be used in the cross-section calculation (Chapter 8). The parameter values in the J/ψ-MC are determined to minimize the difference between the data and MC on the detector-level distributions. In the event generation phase, each event is unweighted, i.e., has a constant weight ($\equiv 1.0$). Then events are given an reweight depending on kinematical variables at the generator level. The reweighting function w consists of the three factors:

$$w = \mathcal{D} \cdot \mathcal{T} \cdot \mathcal{S}, \tag{7.13}$$

where $\mathcal{D}$, $\mathcal{T}$ and $\mathcal{S}$ are reweighting functions related to the J/ψ decay, the t-slope and the form of $\sigma_{tot}^{\gamma^* p \to J/\psi\, p}$. Those functions take the following form,

$$\mathcal{D} = W_d(\cos\theta_h, \phi_h, \Phi;\, \xi), \tag{7.14}$$

$$\mathcal{T} = \frac{\exp(-b\,t)}{\exp(-b_{gen} t)} \quad \text{and} \tag{7.15}$$

$$\mathcal{S} = \frac{\sigma_{tot}^{\gamma^* p \to J/\psi\, p}(Q^2_{had}, W_{had};\, n,\, \delta)}{\sigma_{tot}^{\gamma^* p \to J/\psi\, p}(Q^2_{had}, W_{had};\, n_{gen},\, \delta_{gen})}. \tag{7.16}$$

The parameter set of (ξ, b, n, δ) is determined from the fit to the data, and $(b_{gen}, n_{gen}, \delta_{gen})$ is the set used in the event generation. The decay-angle reweighting function $\mathcal{D}$ is parameterized with the formulae of Eq.(3.25)-(3.26) in p.24 and Eq.(3.5) in p.11. Here the decay angles: $\cos\theta_h$, ϕ_h and Φ are variables with no radiative effects, i.e., before applying `PHOTOS`. An exponentially falling behavior on $d\sigma_{tot}^{\gamma^* p \to J/\psi\, p}/dt$ is assumed in Eq. (7.15). In order to enrich MC statistics in the high-t region ($t \sim 1\,\mathrm{GeV}^2$), the value of $b_{gen} = 3\,\mathrm{GeV}^{-2}$ is emploied though $b \sim 4\,\mathrm{GeV}^{-2}$ is measured both in electroproduction [54] and in photoproduction [2] of J/ψ mesons. As for $\mathcal{S}$, the parameterization in Eq. (5.1) is used. Strictly speaking, obtained values for δ and n by this fit are not physical because the radiative correction depends on the form of $\sigma_{tot}^{\gamma^* p \to J/\psi\, p}$. However, the radiative effects on the scattered lepton line are factorized to a good approximation as,

$$\frac{d^2\sigma^{ep}_{Rad}}{dQ^2_{had} dy_{had}} = \Gamma_{\mathrm{T}} \cdot \left(\frac{1+\epsilon R}{1+R}\right) \cdot \sigma_{tot}^{\gamma^* p \to J/\psi\, p} \cdot (1+\delta_r), \tag{7.17}$$

where σ^{ep}_{Rad} is the radiative ep cross section, Q_{had} and y_{had} are hadronic variables[2], and δ_r is the radiative correction term which is independent of the form of the cross section $\sigma^{\gamma^* p \to J/\psi p}_{tot}$ [55]. As for δ_{gen} and n_{gen}, the best knowledge at present is used: $\delta_{gen} = 0.65$ [2] and $n_{gen} = 2.3$ [54] in order to satisfy the above assumption.

The fitting is performed for the whole final sample divided into sub-regions in $(Q^2_{ct},\, W_{ct},\, |t_{ct}|,\, \cos\theta_h)$ space. Since there is little correlation between distributions of the above variables except for Q^2 and the decay angle $\cos\theta_h$, the fitting can be performed for each variable separately. The fitting is applied upon

(A) the two-dimensional histogram on Q^2_{ct} versus $\cos\theta_h$ with only ξ set to be free and others fixed,

(B) the one-dimensional histogram on Q^2_{ct} with only n set to be free,

(C) the one-dimensional histogram on W_{ct} with only δ set to be free, and

(D) the one-dimensional histogram on $|t_{ct}|$ with only b set to be free.

Iterations of the above fits are done until fitting parameter values are converged.

The most probable values are determined so as to minimize a chisquare function χ^2 defined as

$$\chi^2(\xi,\, b,\, n\,, \delta) \;=\; \sum_{i:bin} \frac{\left\{ N_i^{DATA} - N_i^{MC}(\xi,\, b,\, n\,, \delta) \right\}^2}{\sigma_i^2}, \tag{7.18}$$

where N_i^{DATA} indicates the number of data events in the bin:i, N_i^{MC} is a sum of weights of MC events, i.e., the number of MC events including both the J/ψ and QED processes:

$$N_i^{MC} \;=\; \sum_{k=1}^{N_{bin:i}} w_i^k, \tag{7.19}$$

and σ_i is a combined statistical error of the data and MC:

$$\sigma_i \;=\; \sqrt{\left\{ \sigma\left(N_i^{DATA}\right) \right\}^2 + \left\{ \sigma\left(N_i^{MC}\right) \right\}^2}. \tag{7.20}$$

Minimization of χ^2 is performed using the package `MINUIT` [56].

The obtained parameter values and their error estimates will be used in the cross-section calculation in the next chapter.

[2]The hadronic Q^2 and y are defined as $Q^2_{had} = -q^2_{\gamma^*}$ and $y_{had} = (P_p \cdot q_{\gamma^*})/(P_p \cdot k)$, where q_{γ^*} is a 4-momentum of the virtual photon and P_p (k) is a 4-momentum of the proton (electron) beam particle.

7.9 Comparison of the Data with MC

The final data sample is compared with the sum of the J/ψ-MC and QED-MC on various distributions. As seen in Figure 7.8, the peak positions and their shapes on the J/ψ mass distribution are well-described by the MC (solid histograms). The J/ψ MC (lightly-shaded area) is tuned as described in § 7.8, and is normalized to the sum of the data events in the mass windows for the di-electron and di-muon in (a), (b), and normalized to only the di-electron in (c). The ratio of the number of di-electron events to the number of di-muon events is 0.80 ± 0.06 from the data, which is consistent with the MC prediction of 0.88. The normalization of the QED-MC is taken from the prediction of `GRAPE-Dilepton` with the exclusive and the proton dissociative processes. It is seen that the data and MC agree well outside the J/ψ mass window in Figure 7.8 except for the low-mass region of the di-electron.

Figure 7.9-(a-1,2) show comparisons on Z_{VTX} for (a-1) events in the medium-W region, and for (a-2) events in the high-W region. The di-electron and di-muon channels are combined in (a-1) and (b-1). The input vertex distributions for the MC are based on the measurement on Z_{VTX} in the region of $-100 < Z_{VTX} < 100\,\mathrm{cm}$ using the minimum-biased sample of the inclusive neutral-current DIS [57, 58]. Different distributions are used in different years with a weight proportional to an integrated luminosity of the data in the year.

Figure 7.9-(b-1,2) show comparisons on the total $E - P_Z$. MC describes the data not only on the peak positions which are sensitive to the energy scale of RCAL, but also the tail in the low $E - P_Z$ region, which comes from the radiations on the scattered lepton line and/or decay leptons.

Figure 7.10 shows comparisons on the various quantities related to the scattered electron for the whole final events. The irregular shapes in X_e, Y_e and ϕ_e are due to the box cut. They are well reproduced by the MC.

Figure 7.11 shows comparisons on the various quantities related to the dilepton. MC also describes the data well.

Figure 7.12 and 7.13 show comparisons on kinematical variables used in the cross-section calculation. The histograms in the left columns indicate comparisons of the data with the J/ψ-MC together with the QED-MC in the J/ψ mass window. The tuned J/ψ-MC successfully describes the data. The histograms in the right columns indicate comparisons of the data with the QED-MC only in the sideband which is defined as a mass region of $4 < M_{l^+l^-} < 8\,\mathrm{GeV}$. The QED-MC reproduces the data well. The number of data events in the sideband is 420. It is in good agreement

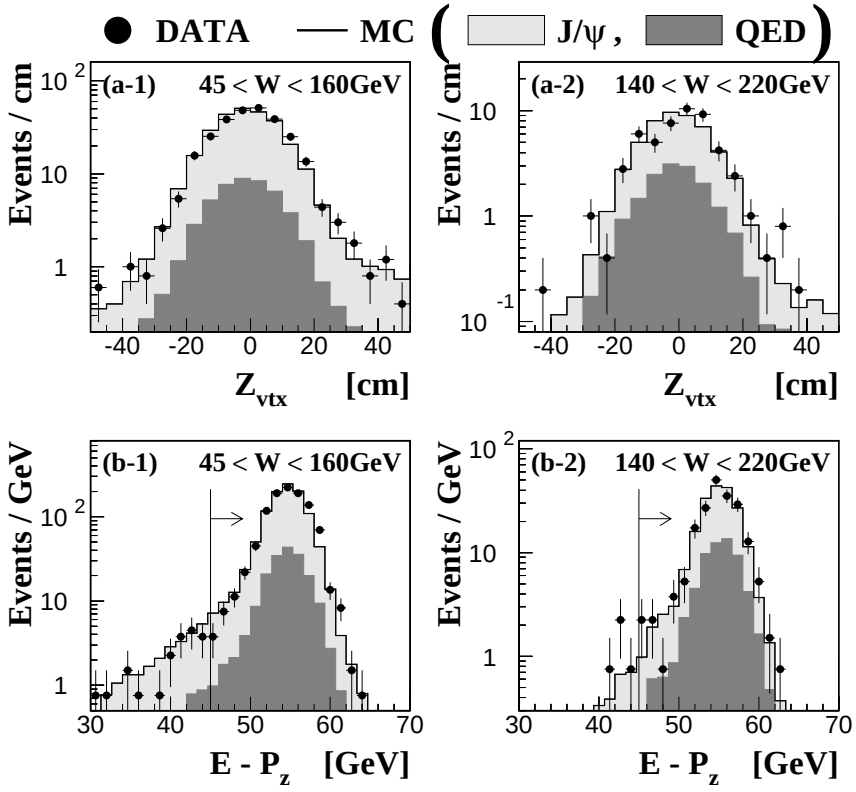

Figure 7.9: *Comparison between the data and MC on (a-1,2) the Z coordinate of the primary vertex (Z_{VTX}) and on (b-1,2) the total $E - P_Z$ of the scattered electron and the dilepton. The left two contain the medium-W sample and the right two contain the high-W one. The vertical lines in (b-1,2) indicate the $E - P_Z$ cut described in the final selection (§ 7.7).*

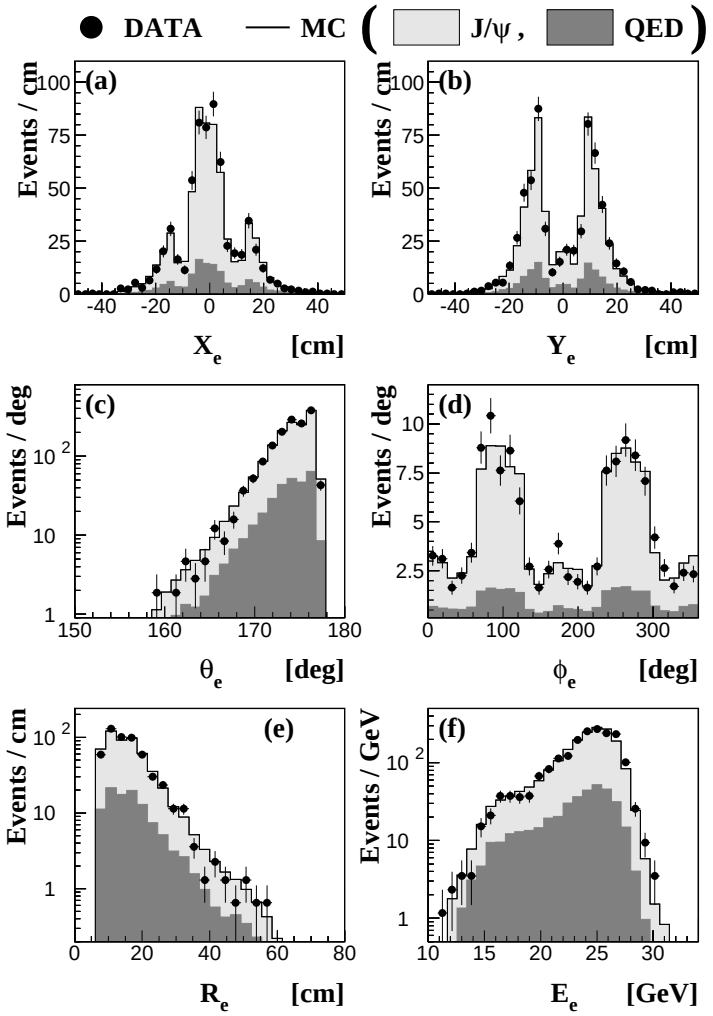

Figure 7.10: *Comparisons between the data and MC on various quantities related to the scattered electron. (a),(b) X and Y positions. (c),(d) Polar and azimuthal angles. (e) Radial radius in XY plane. (f) Energy corrected with SRTD or with the inactive material map of the detector simulation.*

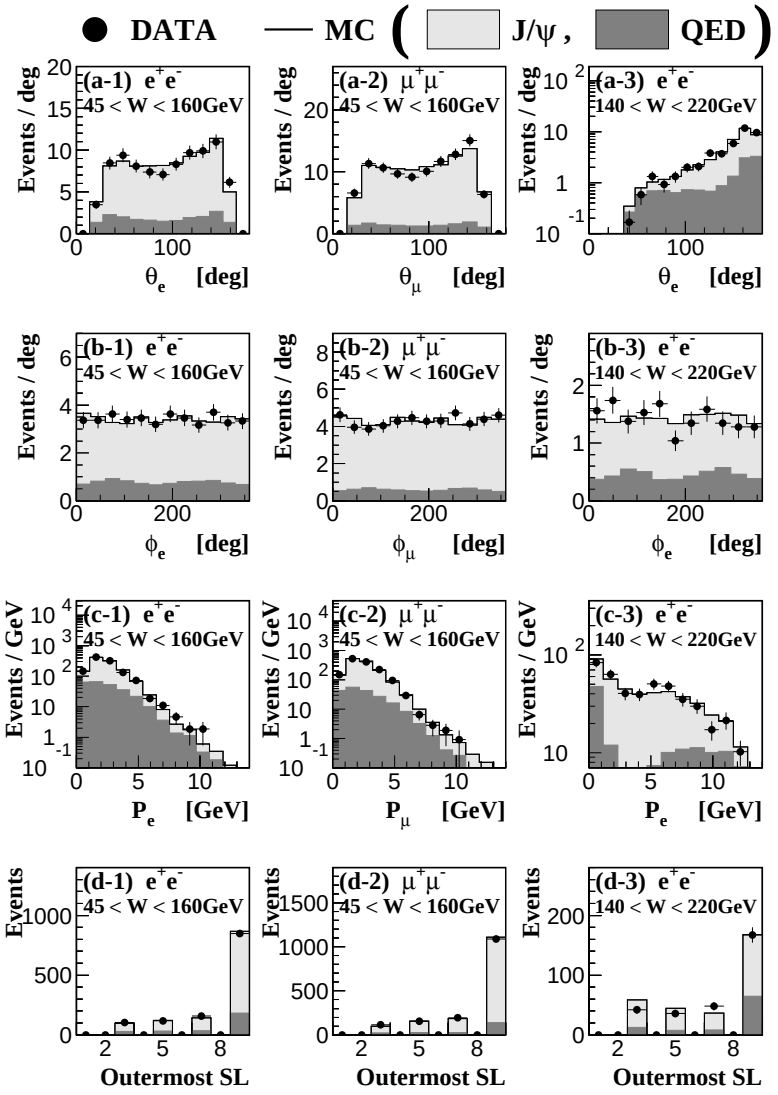

Figure 7.11: *Comparisons between the data and MC on various quantities related to the dilepton. The plots and histograms in the left column are for the di-electron events in the medium-W region, the middle column for the di-muon, and the right column for the di-electron events in the high-W region. (a-1,2,3) Polar angles. (b-1,2,3) Azimuthal angles. (c-1,2,3) Momenta. (d-1,2,3) Outermost SL numbers with hits of the decay tracks.*

with the prediction of the QED-MC: 447.0.

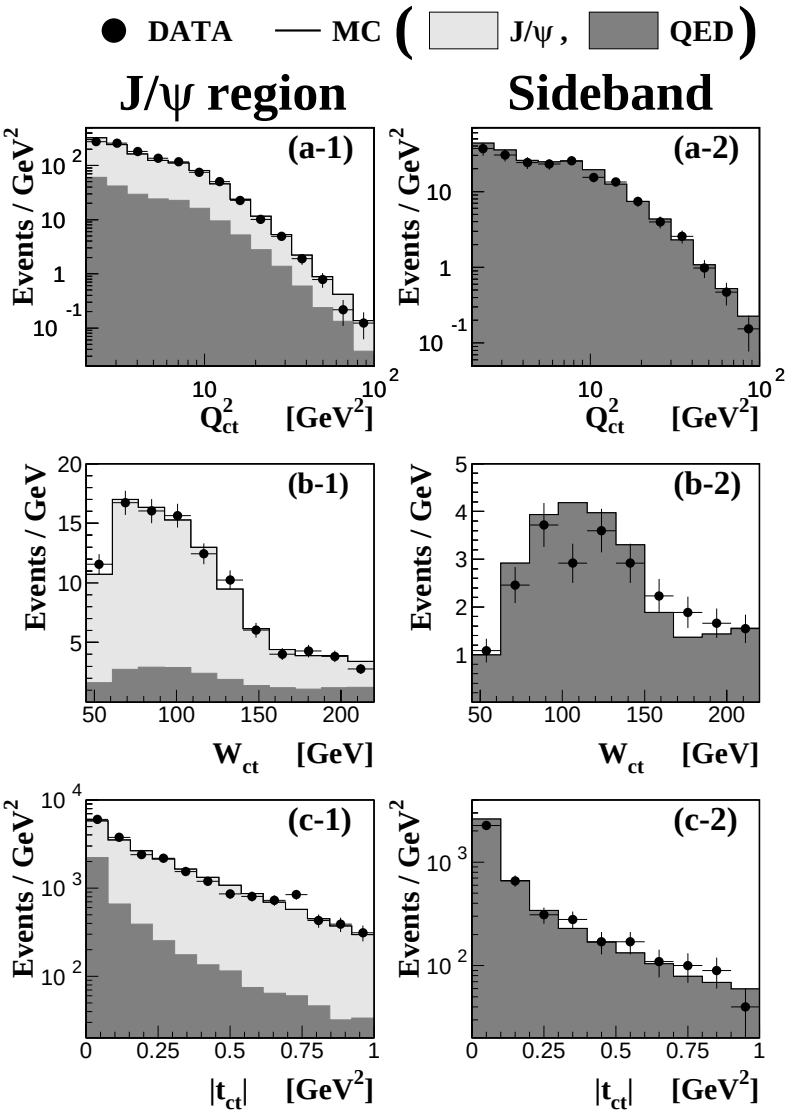

Figure 7.12: *Comparisons between the data and MC on kinematical variables (a,b,c-1) in the J/ψ mass window and (a,b,c-2) in the sideband ($4 < M_{l^+l^-} < 8$ GeV).*

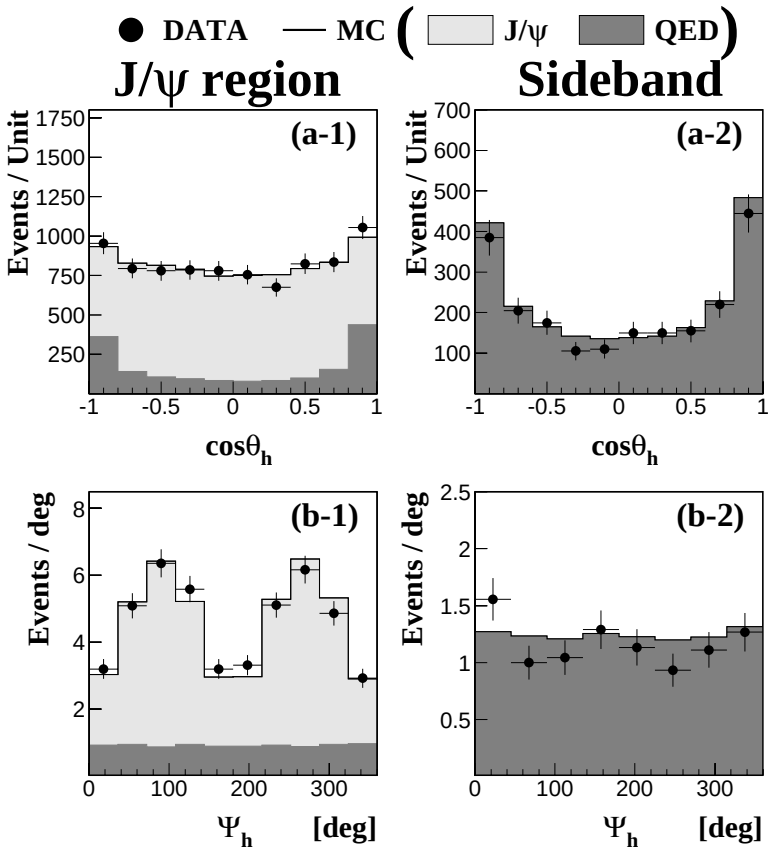

Figure 7.13: *Comparisons between the data and MC on kinematical variables (continued)*

Chapter 8

Extraction of Cross Sections

8.1 Bin Definition

In order to obtain more information from the data, it is better to divide the kinematical region as many subregions (bins) as possible. However, this is limited due to the statistics of the data and the resolutions and migrations in the kinematics reconstruction. In this analysis, bins are defined (binning) according to the following criteria.

- Each bin has an enough number of events so that the statistical error is around or smaller than 10 %, i.e., the number of events in each bin should be around or larger than 100, except for the highest-Q^2 bin and for the high-W region where the number of events is limited.
- Bin sizes are requested to be larger than three-sigma of the resolution in the kinematics reconstruction. Too fine binning compared with the resolution makes the analysis sensitive to the possible difference between the data and MC, and might lead to a large systematical uncertainty.

The binning for the medium-W sample is determined in order to make all the bins to have approximately equal number of events below $Q^2 < 40\,\mathrm{GeV}^2$. That is estimated using the J/ψ-MC with the W-dependence measured in photoproduction [2] and the Q^2-dependence from the electroproduction measurement [54]. For the measurement of the W-dependence of the cross section, the binning is chosen as

$$
\begin{aligned}
W = {} & 45{-}65,\ 65{-}84,\ 84{-}106,\ 106{-}140,\ 140{-}220\,\mathrm{GeV} && \text{for } 2 < Q^2 < 5\,\mathrm{GeV}^2,\\
W = {} & 50{-}72,\ 72{-}93,\ 93{-}116,\ 116{-}150,\ 150{-}220\,\mathrm{GeV} && \text{for } 5 < Q^2 < 10\,\mathrm{GeV}^2,\\
W = {} & 55{-}76,\ 76{-}98,\ 98{-}122,\ 122{-}160,\ 160{-}220\,\mathrm{GeV} && \text{for } 10 < Q^2 < 40\,\mathrm{GeV}^2,\\
W = {} & \qquad 60{-}110,\qquad\qquad 110{-}180 && \text{for } 40 < Q^2 < 100\,\mathrm{GeV}^2.
\end{aligned}
$$

For the measurement of the Q^2-dependence of the cross section the binning is chosen as

$$
\begin{aligned}
&Q^2 = 2.0{-}3.2,\ 3.2{-}5.0\ \mathrm{GeV}^2 \quad \text{with} \quad 53 < W < 140\,\mathrm{GeV}^2,\\
&Q^2 = 5.0{-}7.0,\ 7.0{-}10\ \ \mathrm{GeV}^2 \quad \text{with} \quad 50 < W < 150\,\mathrm{GeV}^2,\\
&Q^2 = 10{-}40\,\mathrm{GeV}^2 \quad \text{with} \quad 55 < W < 140\,\mathrm{GeV}^2,\\
&Q^2 = 40{-}100\,\mathrm{GeV}^2 \quad \text{with} \quad 60 < W < 140\,\mathrm{GeV}^2.
\end{aligned}
$$

The different W-ranges from those for the measurement of the W-dependence are motivated by fixing the reference point at $W = 90\,\mathrm{GeV}$ for all the bins. The details will be explained in § 8.4 (p.95). Figure 8.1 shows the binning with bold-solid lines in the (x_{ct}, Q^2_{ct}) space together with the data events which have passed all the cuts except for Q^2_{ct} and W_{ct}. The open (closed) circles indicate the $J/\psi \to e^+e^-$ candidates from the two-track (one-track) sample. The squares indicate the $J/\psi \to \mu^+\mu^-$ candidates.

8.2 Resolutions and Migrations

Figure 8.2 and 8.3 show the resolutions in the reconstruction of Q^2_{ct} and W_{ct}, respectively, estimated with the J/ψ-MC for each bin. Resolutions are estimated as

$$
\frac{Q^2_{ct}(recon) - Q^2_{ct}(true)}{Q^2_{ct}(true)} \quad \text{and}
$$
$$
\frac{W_{ct}(recon) - W_{ct}(true)}{W_{ct}(true)}.
$$

The Q^2_{ct} resolution is 7% in the lowest-Q^2 bins and better in the higher-Q^2_{ct} down to 3 % for both the di-electron and di-muon channels. The distributions in Figure 8.2 show a good Gaussian shape with no tail. The W_{ct} resolution for the di-electron is 1 % in the lowest-W bins, increasing toward higher W, up to 3 % as seen in Figure 8.3-(a). Tails in the lower side are seen, which are originated from the photon radiation from the decay leptons. They are, however, within 10 %. The W_{ct} resolution for the di-muon is much better than that for the di-electron, and approximately a constant of 0.3 % due to the benefit of the $M_{J/\psi}$ constraint method.

The absolute sizes of the resolutions and migrations are visualized in Figure 8.4 and Figure 8.5 for the final sample of the $J/\psi \to e^+e^-$ and $J/\psi \to \mu^+\mu^-$ MC, respectively. The arrows are drawn from the true (x_{ct}, Q^2_{ct}) point to the center of the reconstructed point, and the size of ellipses shows the one-sigma resolution on x_{ct} and Q^2_{ct} at the phase space point. As shown in Figure 8.4 and 8.5, the arrows are

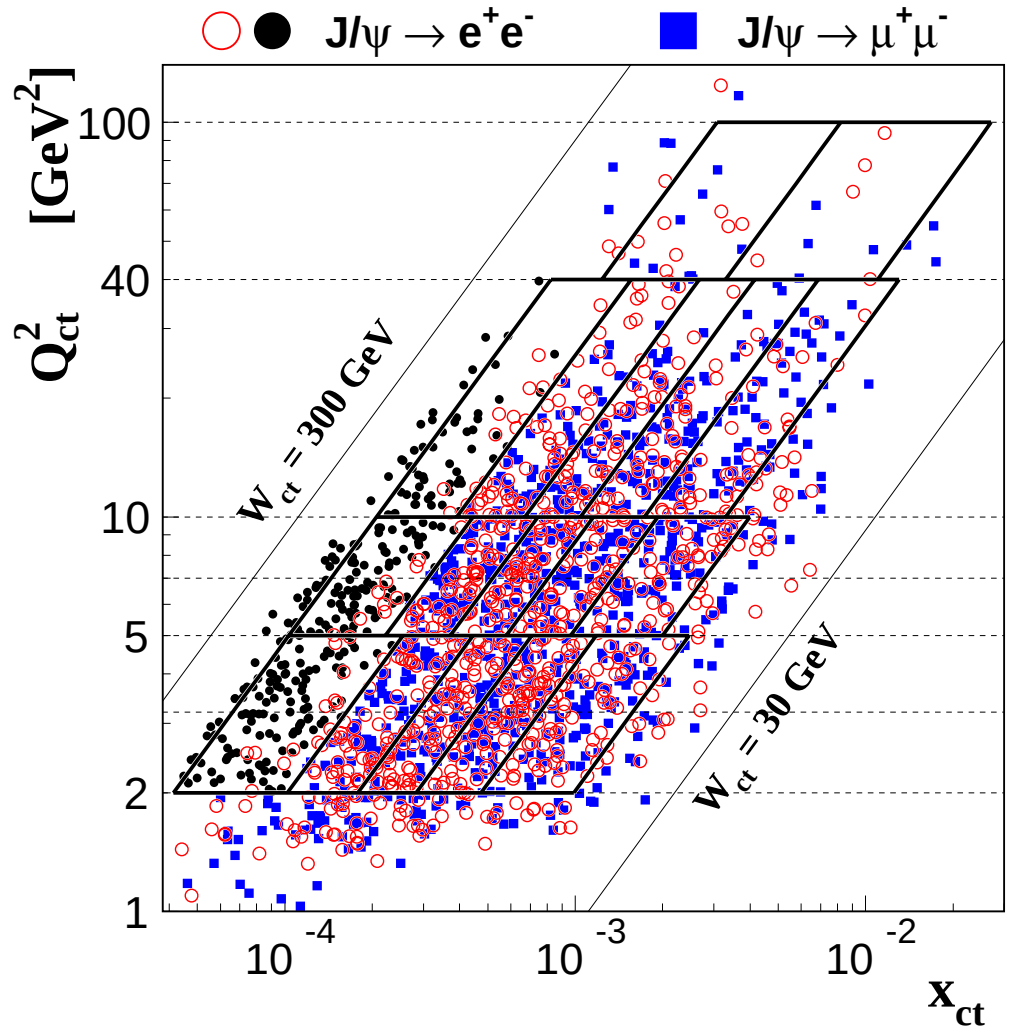

Figure 8.1: *Bin definition (bold-solid lines) and the final data events of the $J/\psi \to e^+e^-$ (circles) and $J/\psi \to \mu^+\mu^-$ (squares) candidates. The closed circles indicate the one-track sample.*

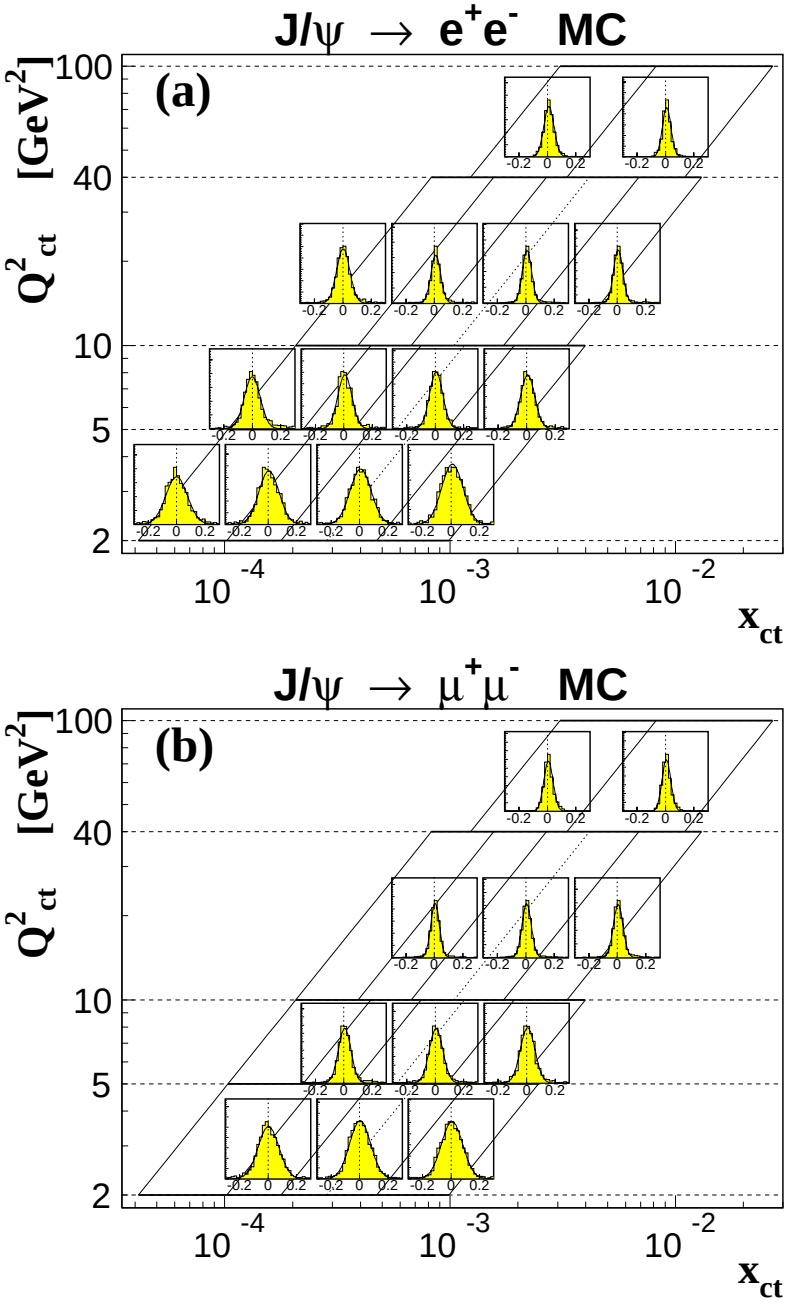

Figure 8.2: *Resolution on the Q^2_{ct} reconstruction in each bin estimated with the final MC events of the (a) $J/\psi \to e^+e^-$ and (b) $J/\psi \to \mu^+\mu^-$ channel. The horizontal axes in the insets indicate $\{Q^2_{ct}(recon) - Q^2_{ct}(true)\}/Q^2_{ct}(true)$ in the range [-0.3,+0.3].*

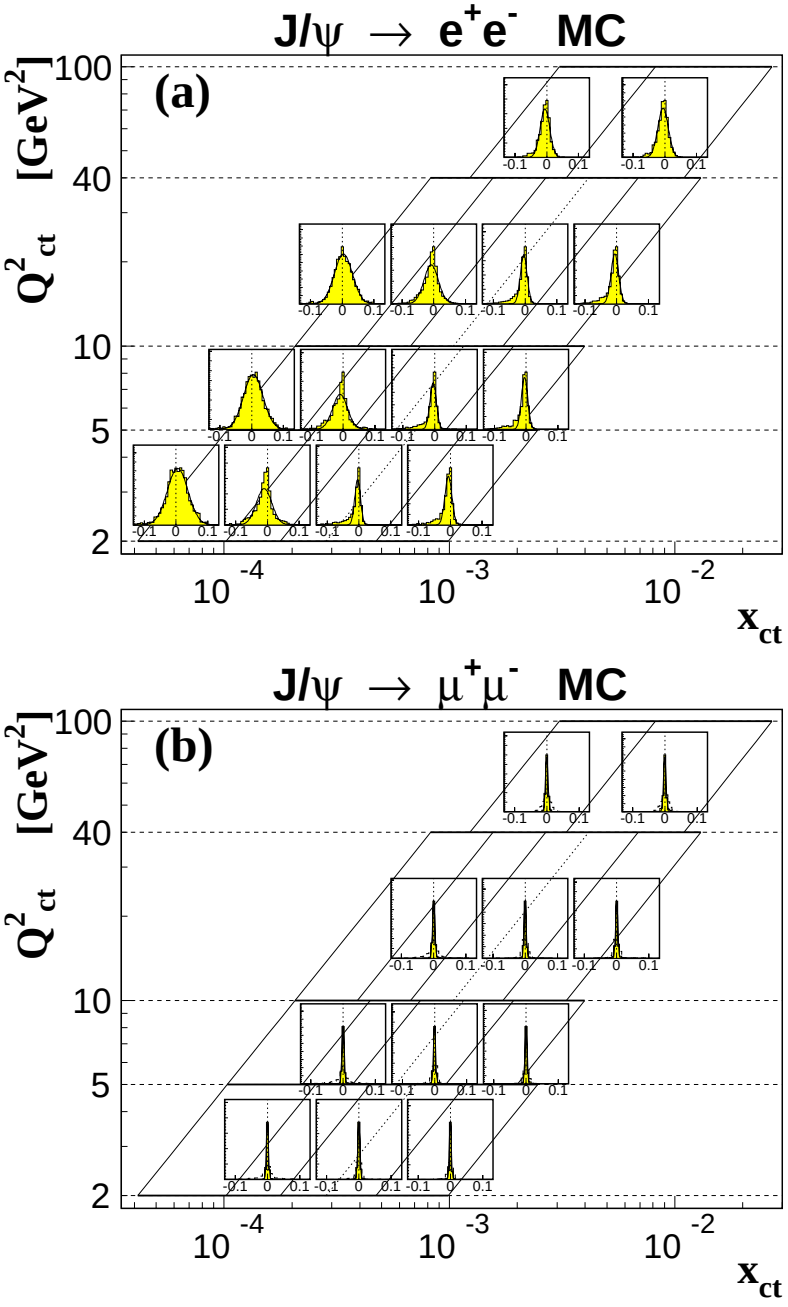

Figure 8.3: *Resolution on the W_{ct} reconstruction in each bin estimated with the final MC events of the (a) $J/\psi \to e^+e^-$ and (b) $J/\psi \to \mu^+\mu^-$ channel. The horizontal axes in the insets indicate $\{W_{ct}(recon) - W_{ct}(true)\}/W_{ct}(true)$ in the range [-0.13,+0.13].*

hardly seen in the plots, and the sizes of the ellipses are small compared with the bin sizes, so that it can be concluded that the bin sizes of the above binning are large enough to control the resolutions and migrations in the kinematics reconstruction.

8.3 Calculation of the $\gamma^* p$ Total Cross Section

The procedure to derive the $\gamma^* p$ total cross section consists of the following four steps in this analysis.

(1) Calculation of the radiative ep cross section, σ^{ep}_{Rad}, for the J/ψ total production from the background-subtracted number of observed events using the bin-by-bin unfolding method.

(2) Conversion of the radiative cross section to the corresponding born cross section, σ^{ep}_{Born}.

(3) Combining the results from the di-electron and di-muon channel, and results with the proton-beam energy of 820 GeV and of 920 GeV.

(4) Translation into the exclusive $\gamma^* p$ total cross section, $\sigma^{\gamma^* p \to J/\psi\, p}_{tot}$.

In the following sections, the above procedure is explained.

8.3.1 Radiative ep cross section

What is measured from the data is the radiative ep cross section integrated over the bin. Since the J/ψ-MC is well-tuned and the MC describes the data well, a simple bin-by-bin unfolding method is adopted. The cross section is calculated according to the following formula,

$$\iint_{Bin} dQ^2_{ct} dW_{ct} \frac{d^2\sigma^{ep}_{Rad}}{dQ^2_{ct} dW_{ct}} = \frac{\left(N^{DATA}_{obs} - N_{bg}\right)\left(1 - f_{pd}\right)\left(1 - f^{l^+l^-}_{\psi'}\right)}{L \cdot \mathcal{A}_{l^+l^-} \cdot \mathcal{B}_{l^+l^-}}, \tag{8.1}$$

where N^{DATA}_{obs} is the number of events observed in the bin, and N_{bg} is the number of non-J/ψ events in the bin. In this analysis, N_{bg} is assumed to be only the number of dilepton events in the QED process, which is estimated with the QED-MC. The pion background accompanied by multi-pion ($ep \to ep\,\pi\pi\cdots$) is neglected in the calculation of nominal cross sections since shapes and absolute normalizations of the invariant mass distributions of dilepton in the sidebands are well reproduced with the QED-MC (Figure 7.8 and § 7.9). The possible remaining pion background is included in the systematic error on the QED background normalization (p.99)

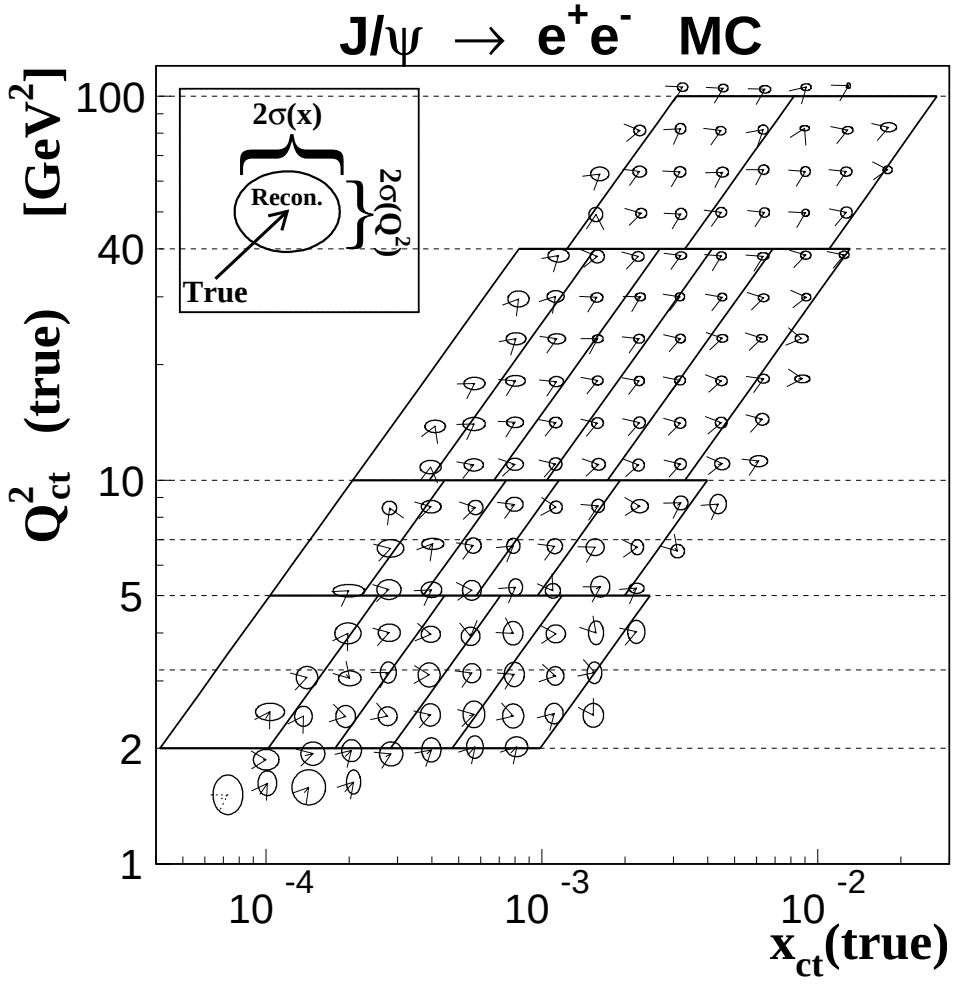

Figure 8.4: *Resolutions and migrations for the $J/\psi \to e^+e^-$ events from the two-track sample are shown using ellipses and arrows, respectively. The arrows indicate a bias on the kinematics reconstruction. See the text for more details.*

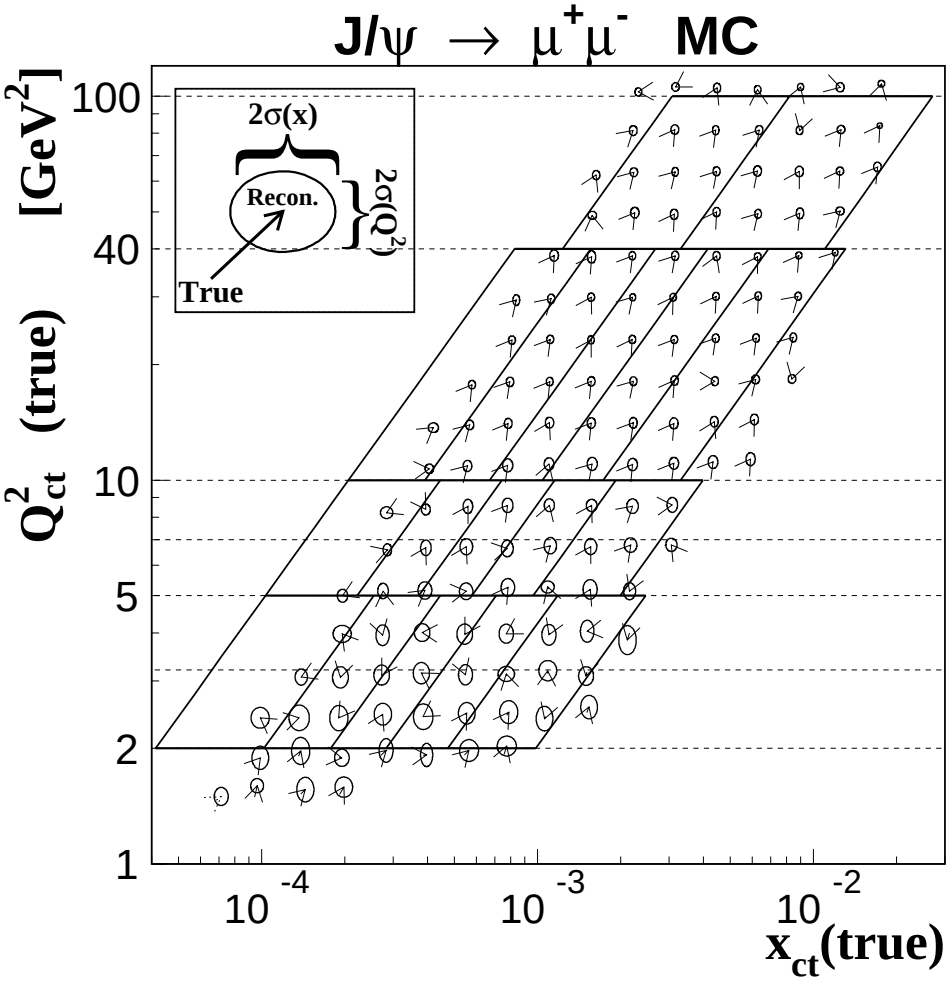

Figure 8.5: *Resolutions and migrations for the $J/\psi \to \mu^+\mu^-$ events are shown using ellipses and arrows, respectively. The arrows indicate a bias of the kinematics reconstruction. See the text for more details.*

where the QED normalization is changed. L indicates the integrated luminosity of the data. $\mathcal{A}_{l^+l^-}$ is the overall acceptance estimated with the J/ψ-MC as

$$\mathcal{A}_{l^+l^-} = \frac{Number\ of\ events\ reconstructed\ in\ the\ bin}{Number\ of\ events\ generated\ in\ the\ bin}, \tag{8.2}$$

where the radiative correction on the decay leptons is included in this overall acceptance. $\mathcal{B}_{l^+l^-}$ is the branching ratio of $J/\psi \to l^+l^-$: $\mathcal{B}_{e^+e^-} = 5.93 \pm 0.10\,\%$ and $\mathcal{B}_{\mu^+\mu^-} = 5.88 \pm 0.10\,\%$ [49]. f_{pd} is the fraction of events with proton dissociation, which is determined with the study of J/ψ photoproduction [2]: $21 \pm 9\,\%$ in 1996-1997 and $13 \pm 5\,\%$ in 1998-2000. Those values are consistent with the fractions for the dilepton production in the QED process estimated with `GRAPE-Dilepton`. `GRAPE-Dilepton` shows no Q^2-dependence of the fraction. $f_{\psi'}$ is the fraction of J/ψ candidates from $\psi'(\to J/\psi + X \to l^+l^- + X)$ production ($4 \pm 1\,\%$ [3]).

8.3.2 Radiative correction

The radiative cross section is related to the Born-level ep cross section, σ^{ep}_{Born}, as

$$\sigma^{ep}_{Born} \stackrel{\text{def}}{\equiv} \iint_{Bin} dQ^2 dW \frac{d^2\sigma^{ep}_{Born}}{dQ^2 dW} = \mathcal{C}_{Rad} \times \iint_{Bin} dQ^2_{ct} dW_{ct} \frac{d^2\sigma^{ep}_{Rad}}{dQ^2_{ct} dW_{ct}}, \tag{8.3}$$

where $\mathcal{C}_{Rad}$ is the radiative correction factor. This factor is estimated with the J/ψ-MC for each bin by calculating cross sections with and without the radiative correction using `HERACLES`. Any value of this factor is less than 4% away from unity in this analysis.

8.3.3 Combining the different samples

Data sets with different proton-beam energies, and different decay channels are combined at the level of the ep Born cross section. Using the information on the ratios of the cross sections between different samples predicted by MC, the statistical uncertainty in the cross-section measurement can be reduced. The detailed explanation is given in Appendix C. The resulting formula is

$$\sigma^{ep}_{Born} = \frac{N^{DATA}_{obs} - N^{MC}_{QED}}{\tilde{\boldsymbol{A}}}, \tag{8.4}$$

where $\tilde{\boldsymbol{A}}$ is the combined acceptance.

8.3.4 The $\gamma^* p$ total cross section

As shown in Eq.(2.17) in p.8, the relation between σ^{ep}_{Born} and $\sigma^{\gamma^* p \to J/\psi\, p}_{tot}$ is

$$\sigma^{ep}_{Born} = \iint_{Bin} dQ^2 dW \, \frac{2W}{s} \cdot \Gamma_{\rm T} \cdot \left(\frac{1+\epsilon\, R}{1+R} \right) \cdot \sigma^{\gamma^* p \to V p}_{tot}, \tag{8.5}$$

so that an assumption on the functional form of $\sigma^{\gamma^* p \to V p}_{tot}$ is needed in order to derive the $\gamma^* p$ cross section. The $\gamma^* p$ cross section at a fixed phase space point in the bin (Q^2_0, W_0), hereafter called a reference point, is obtained using the parameterization of Eq. (5.1) in p.41,

$$\sigma^{\gamma^* p \to J/\psi\, p}_{tot}(Q^2, W) = k \, \frac{W^\delta}{(Q^2 + M_{J/\psi})^n}, \tag{8.6}$$

where k is a constant in the bin. For the parameters of n and δ, the tuned values obtained in the J/ψ-MC tuning (§ 7.8) are used. The cross section measurement is equivalent to determining the value of k in each bin. Substituting Eq. (8.6) for Eq. (8.5), the formula to calculate the value of k is obtained,

$$k = \frac{\sigma^{ep}_{Born}}{\iint_{Bin} dQ^2 dW \, \frac{2W}{s} \cdot \hat{\Gamma}(Q^2, W, s) \cdot \frac{W^\delta}{(Q^2 + M_{J/\psi})^n}}, \tag{8.7}$$

where $\hat{\Gamma}$ is defined as

$$\hat{\Gamma} = \Gamma_{\rm T} \cdot \frac{1+\epsilon R}{1+R}. \tag{8.8}$$

For R, the parameterization (3.5) in p.11 is used with the ξ value obtained in the fit in § 7.8 (p.75). Then substituting Eq. (8.7) for Eq. (8.6), the formula to calculate the $\gamma^* p$ cross section is obtained,

$$\sigma^{\gamma^* p \to J/\psi\, p}_{tot}(Q^2_0, W_0) = \frac{\sigma^{ep}_{Born} \cdot \frac{W_0^\delta}{(Q^2_0 + M_{J/\psi})^n}}{\iint_{Bin} dQ^2 dW \, \frac{2W}{s} \cdot \hat{\Gamma}(Q^2, W, s) \cdot \frac{W^\delta}{(Q^2 + M_{J/\psi})^n}}. \tag{8.9}$$

8.4 Choice of Reference Points

A reference point (Q^2_0, W_0) in the bin is chosen as a point where the sensitivity of the errors on n and δ to the $\gamma^* p$ cross section is close to the minimum. Here the following quantity, referred as *uncertainty* hereafter, is calculated,

$$U(Q^2_0, W_0) = \max_{\substack{\delta-\Delta\delta<\delta'<\delta+\Delta\delta \\ n-\Delta n<n'<n+\Delta n}} \left| \frac{\sigma^{\gamma^* p}_{tot}(Q^2_0, W_0\,;\, n', \delta') - \sigma^{\gamma^* p}_{tot}(Q^2_0, W_0\,;\, n, \delta)}{\sigma^{\gamma^* p}_{tot}(Q^2_0, W_0\,;\, n, \delta)} \right|, \tag{8.10}$$

where n and δ are parameters in Eq. (8.6). The values of Δn and $\Delta\delta$ are the estimated errors for n and δ, respectively, in the fit (§ 7.8).

The top two-dimensional histogram in Figure 8.6 shows an example of the uncertainty as a function of the reference point $(Q_0^2,\ W_0)$ for the bin: $2 < Q^2 < 5\,\mathrm{GeV}^2$ and $45 < W < 65\,\mathrm{GeV}$. Such estimation has been performed for all of the bins. It has been found that any uncertainty is less than 0.5 % in the Q^2 range of $2 < Q^2 < 40\,\mathrm{GeV}^2$ and less than 1.0 % in $40 < Q^2 < 100\,\mathrm{GeV}^2$.

The W-ranges for the Q^2-slope measurement are determined so that the uncertainty is close to minimum at the fixed $W_0 = 90\,\mathrm{GeV}$. The resulting ranges are shown in Figure 8.7 and in § 8.1 (p.86). Any uncertainty is less than 1 % except for that of the highest Q^2 bin where the statistical error is larger than 20 %, and the uncertainty is 2.2 %.

8.5 Systematical Errors

The systematical errors, mainly originated from possible differences between the data and MC, are estimated changing the selection criteria and the J/ψ-MC parameterization by a reasonable size.

At first, cross sections are calculated with the nominal selection using the optimized selection criteria and parameterization for the J/ψ-MC. For each source of the systematical errors, the cross section is recalculated by changing the selection criteria or varying the parameter values of the J/ψ-MC parameterization. The size of each systematical error is represented as a shift of the central value of the cross section. The total systematical error is evaluated as a sum of the shifts in quadrature, separately for positive and negative directions:

$$\left(\Delta\sigma\right)_L^{Syst} = \sqrt{\sum_{\sigma_i<\sigma_0}(\sigma_i-\sigma_0)^2} \quad \text{and} \tag{8.11}$$

$$\left(\Delta\sigma\right)_U^{Syst} = \sqrt{\sum_{\sigma_i>\sigma_0}(\sigma_i-\sigma_0)^2}, \tag{8.12}$$

where $\left(\Delta\sigma\right)_L^{Syst}$ and $\left(\Delta\sigma\right)_U^{Syst}$ are the total systematical errors in the lower and upper sides, respectively, the subscript i is an index of the systematical error, σ_i is a corresponding cross section for the systematics check: i, and σ_0 is the nominal cross section. The estimated systematical uncertainties are listed below.

- **Parameterization of the J/ψ-MC**

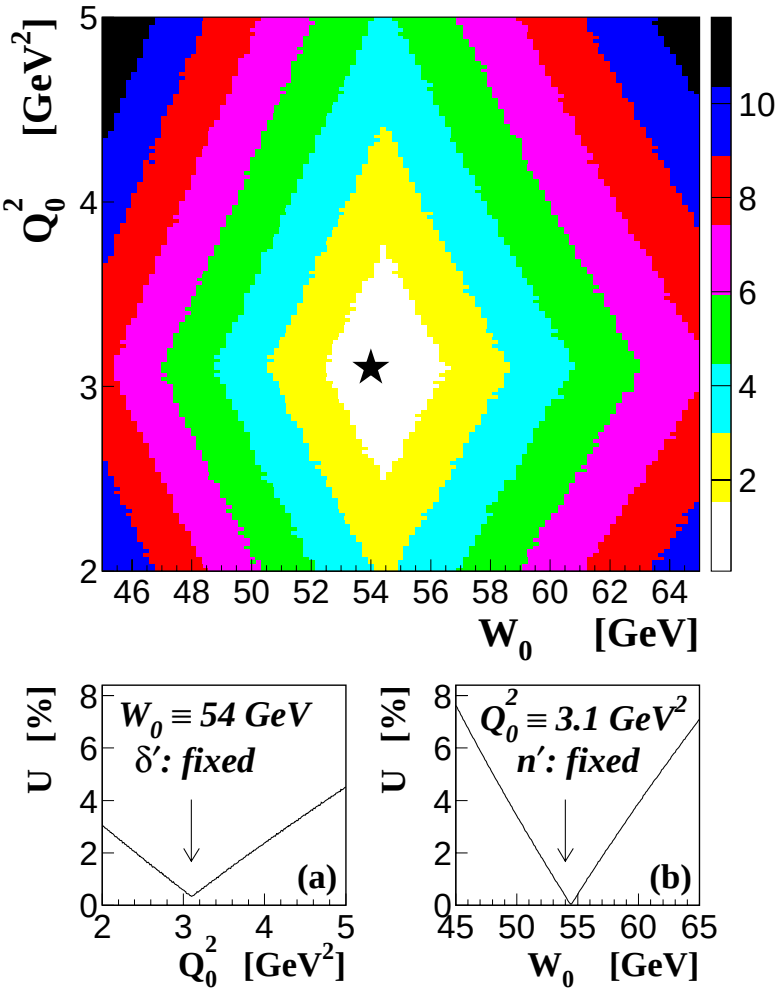

Figure 8.6: *Uncertainty of the parameterization on the $\gamma^* p$ cross section as functions of Q_0^2 and W_0 (the top two-dimensional histogram), and the chosen reference point in the bin (a star in the top) for the bin: $2 < Q^2 < 5\ GeV^2$ and $45 < W < 65\ GeV$. (a) Uncertainty as a function of Q_0^2 where W_0 is fixed at 54 GeV. (b) Uncertainty as a function of W_0 where Q_0^2 is fixed at 3.1 GeV.*

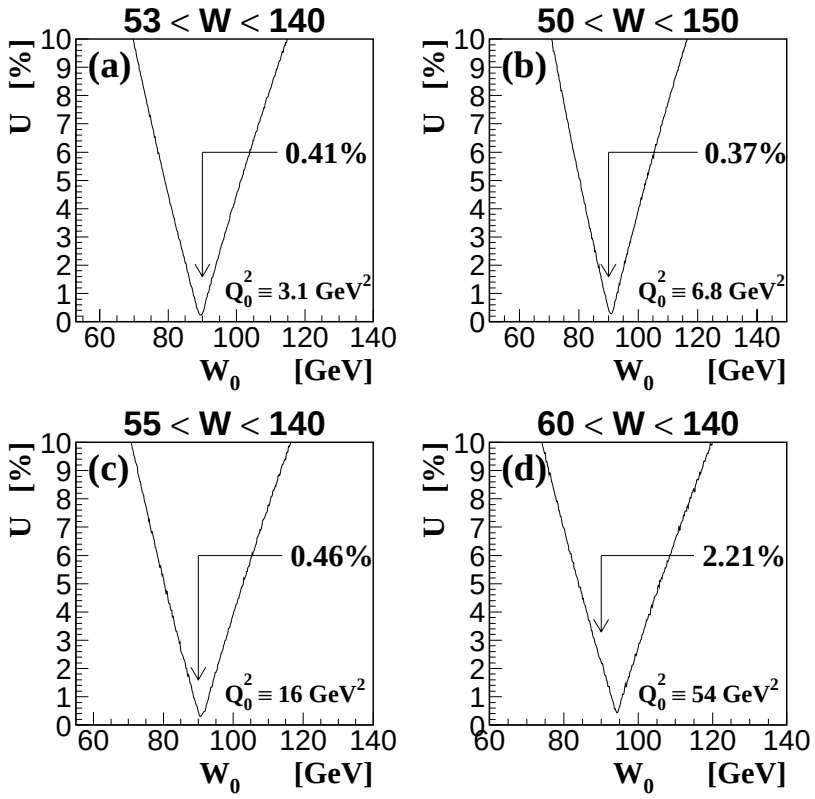

Figure 8.7: *Uncertainty of the parameterization on the $\gamma^* p$ cross section for the measurement of the Q^2-dependence in (a) $2 < Q^2 < 5\ GeV^2$, (b) $5 < Q^2 < 10\ GeV^2$, (c) $10 < Q^2 < 40\ GeV^2$, and (d) $40 < Q^2 < 100\ GeV^2$. Values in percentage indicate uncertainty at $W_0 = 90\ GeV$. The tuned W-ranges are shown at the top of the boxes. Any uncertainty is less than 1 % except for that of the highest Q^2 bin where the statistical error is larger than 20 %.*

The distributions of the J/ψ-MC are changed varying the parameter values of n and δ in Eq. 5.1 (p.41), b in Eq. 5.2 (p.42) and ξ in Eq.(3.5) around the optimized values obtained in § 7.8 (p.75) by two-sigma of the error of the fit.

- **Mass window**

  The nominal mass window with $a < M_{l^+l^-} < b$ is changed by ± 0.1GeV,

  the narrower case $(-0.1\,\mathrm{GeV})$: $a - (-0.1\,\mathrm{GeV}) < M_{l^+l^-} < b - 0.1\,\mathrm{GeV}$,

  the wider case $(+0.1\,\mathrm{GeV})$: $a - (+0.1\,\mathrm{GeV}) < M_{l^+l^-} < b + 0.1\,\mathrm{GeV}$.

  The value of 0.1 GeV is more than twice of the mass resolution with CTD tracks.

- **Pt cut**

  The minimum value for the transverse momentum of CTD-tracks is changed from 0.20 GeV down to 0.15 GeV or up to 0.30 GeV. The lower value is a minimum transverse momentum for the track reconstruction with an enough quality. Particles with a transverse momentum larger than 0.3 GeV can reach CAL unless the particle loses a large amount of energy in the inactive material before the CAL.

- **Elasticity threshold**

  The maximum allowed energy of cone-islands for the elasticity requirement is changed from 0.3 GeV to 0.4 GeV in order to check an influence from non-signal events with other particles.

- **SRTD position**

  The SRTD has an effect only on the reconstruction of Q^2_{ct}, so that its position is shifted only in the following two directions by the accuracy of the alignment,

  the inner-direction case $(-2\,\mathrm{mm})$ or

  the outer-direction case $(+2\,\mathrm{mm})$.

  In the former case, the four quadrants of the SRTD are shifted closer to the beam pipe and a lower Q^2_{ct} value is reconstructed, and vice versa in the latter case. The above shifts are done only for MC.

- **Track separation**

  CTD tracks for decay lepton candidates are required to be separated each other by the typical size of CTD cells: 5 cm in the $X - Y$ plane.

- **Outermost SL**

  CTD-tracks having SL2 as an outermost SL with hits are saved in order to check the effect from the possible difference between the data and MC on the efficiency of reconstructing hits in SL3.

- **Vertex-fitting**
  Events with only one vertex-fitted track are saved in order to check the efficiency of CTD-tracks to be fitted to the primary vertex.

- **Matching of a CTD-track to cone-islands**
  The matching condition is changed from the nominal one (§ 7.4.2, p.63).
  ▷ The maximum value for the closest approach of the decay lepton to cone-islands is changed from 30 cm down to 25 cm or up to 35 cm. The size of 5 cm is a typical resolution of the closet approach.
  ▷ The matching algorithm of merging all cone-islands within the specified closest approach is changed into a algorithm that a nearest one is selected, or that one with the largest energy is selected.

- **Energy cut for scattered electron**
  The minimum energy for scattered electrons is changed from 10 GeV down to 8 GeV.

- **QED background normalization**
  The normalization of the QED background estimated with `GRAPE-Dilepton` MC is changed by 10 % up or 10 % down, corresponding to the statistics of the sideband events.

- **Proton dissociation fraction**
  The fraction of the proton dissociative J/ψ production is changed according to the estimated errors [2] separately for data in 1996-97 and in 1998-00.

- **Luminosity measurement**
  The luminosity monitor measures an integrated luminosity with an precision better than 2 % [59]. Major errors from an experimental side originate from the simulation of the photon response (0.9 %) and the estimation of the acceptance (0.8 %) of the luminosity monitor. Minor errors come from the estimation of the fraction of multiple events (0.4 %) and the subtraction of the e-gas background (0.1 %). In a theoretical side, a dominant error is a cross section uncertainty in the higher order QED corrections (0.5 %). The result of the luminosity measurement using the luminosity monitor was further checked using the QED Compton process: $ep \to ep\gamma$ with the final state electron and photon detected with the RCAL, i.e. with an independent detector. A good agreement was obtained within a precision of 6 %. In this analysis, the size of 2 % is used as an error of the luminosity

measurement.

- **Leptonic branching ratios of J/ψ**
  The errors on the leptonic branching ratios, $\mathcal{B}_{e^+e^-} = 5.93 \pm 0.10\,\%$ and $\mathcal{B}_{\mu^+\mu^-} = 5.88 \pm 0.10\,\%$ [49] are taken into account.

- **Trigger efficiency**
  Trigger efficiencies are calculated for events taken with an independent trigger logic from one used in this analysis. For di-electron events, a trigger based on the electron-finding in the SLT is used. For di-muon events, a trigger using the BRMUON is used. In both cases, the estimated trigger efficiency is above 98 %, and consistent with the MC prediction. Therefore, the uncertainty related to the trigger efficiency is negligible.

- **EMC-fraction in the BCAL for di-electron events**
  EMC-fractions of cone-islands from decay electrons could become less than 0.9, especially in the BCAL module cracks. The EMC-fraction for di-electron events is checked, where one of the decay electrons of e^+ and $e-$ is tagged with HES, and the EMC-fraction corresponding to the other electron is measured. It is found that the fraction of events having the EMC-fraction less than 0.9 is 2.3±1.3 % from the data, which is consistent with the MC prediction of 1.8±0.1 %. Therefore, the uncertainty related to this check is negligible.

- **Cosmic muons**
  The contribution from cosmic muons in the di-muon events is checked by investigating the distribution of the three-dimensional opening angle at the primary vertex, $\theta_{opening}$. No contribution is found at $\theta_{opening} \sim 180^\circ$.

Figure 8.8 shows the fractional systematical errors for the bins defined in § 8.1 (p.85). Only the largest six sources are shown explicitly as (1)-(6). Any size of the total systematical errors is less than that of the corresponding statistical error.

Figure 8.9 and 8.10 show systematical errors on the W- and Q^2-slope parameters, δ and n in Eq.(5.1) in p.41, respectively. Figure 8.11 shows systematic errors on $R = \sigma_L^{\gamma^* p}/\sigma_T^{\gamma^* p}$. This measurement will be discussed in Chapter 9. There is no significant contribution seen from the systematical errors compared with the statistical ones.

Figure 8.12 and 8.13 show measured cross sections separately from the di-electron and di-muon channel. Only statistical errors are shown. For any bin, a difference is less than 2-sigma. The total difference is estimated with a quantity of $\chi^2/(number\ of\ points)$. The resulting values are 16.1/12 for Figure 8.12 and 5.4/6

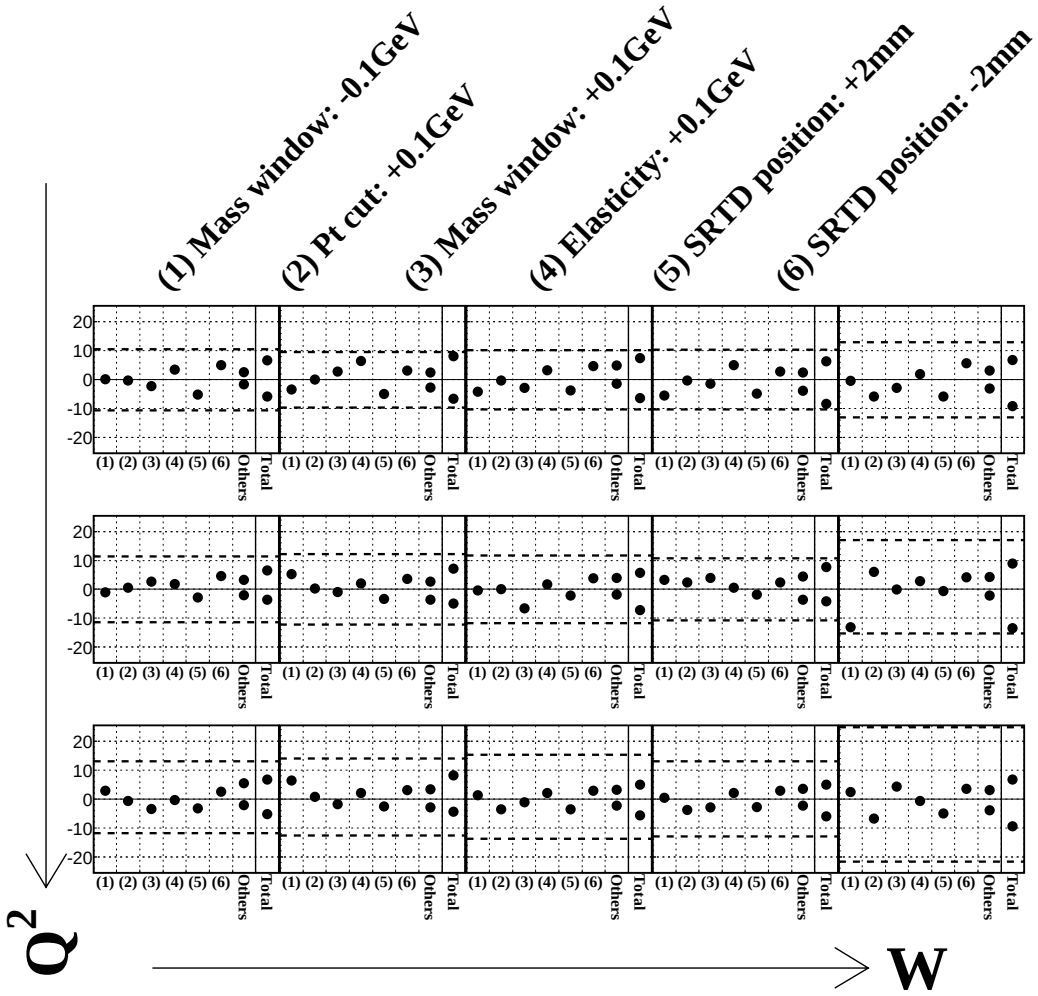

Figure 8.8: *Systematical errors on the cross-section values for the bins defined in § 8.1 (p.85). The unit in the vertical axis is %. The dashed-bold lines in the horizontal direction indicate a statistical error in the bin.*

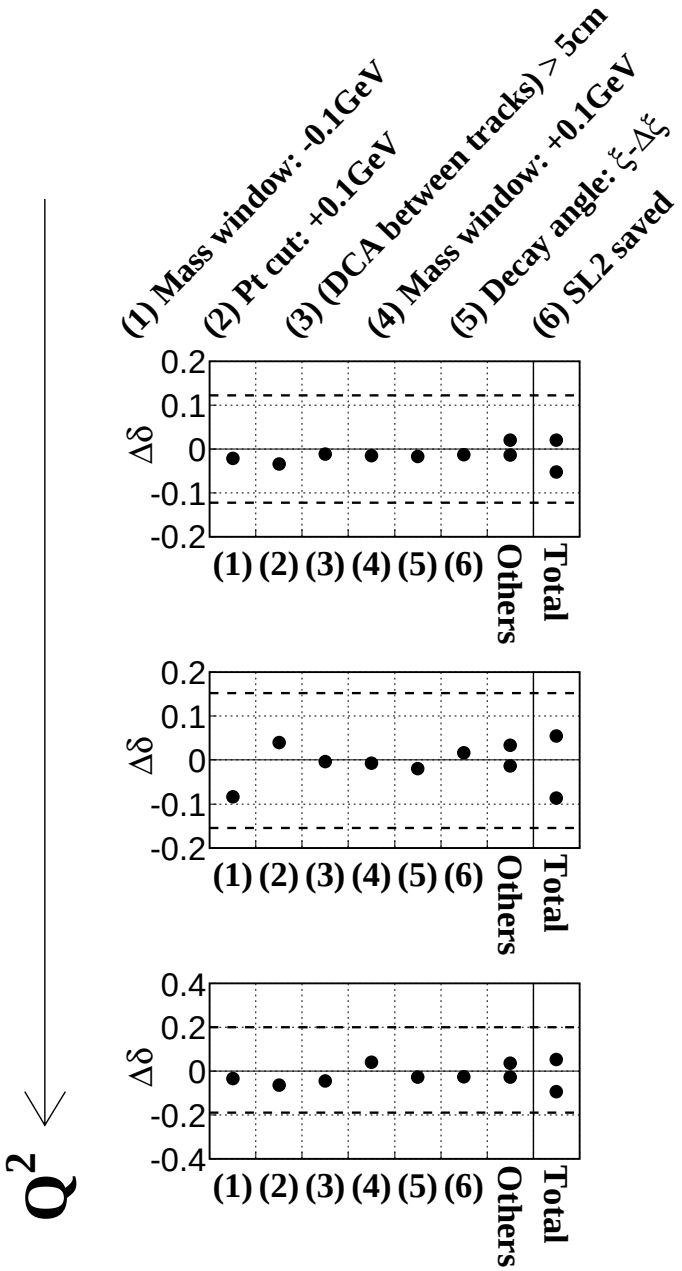

Figure 8.9: *Systematical errors on the W-slope parameter δ for the bins defined in § 8.1 (p.86). The dashed-bold lines in the horizontal direction indicate a statistical error in the bin.*

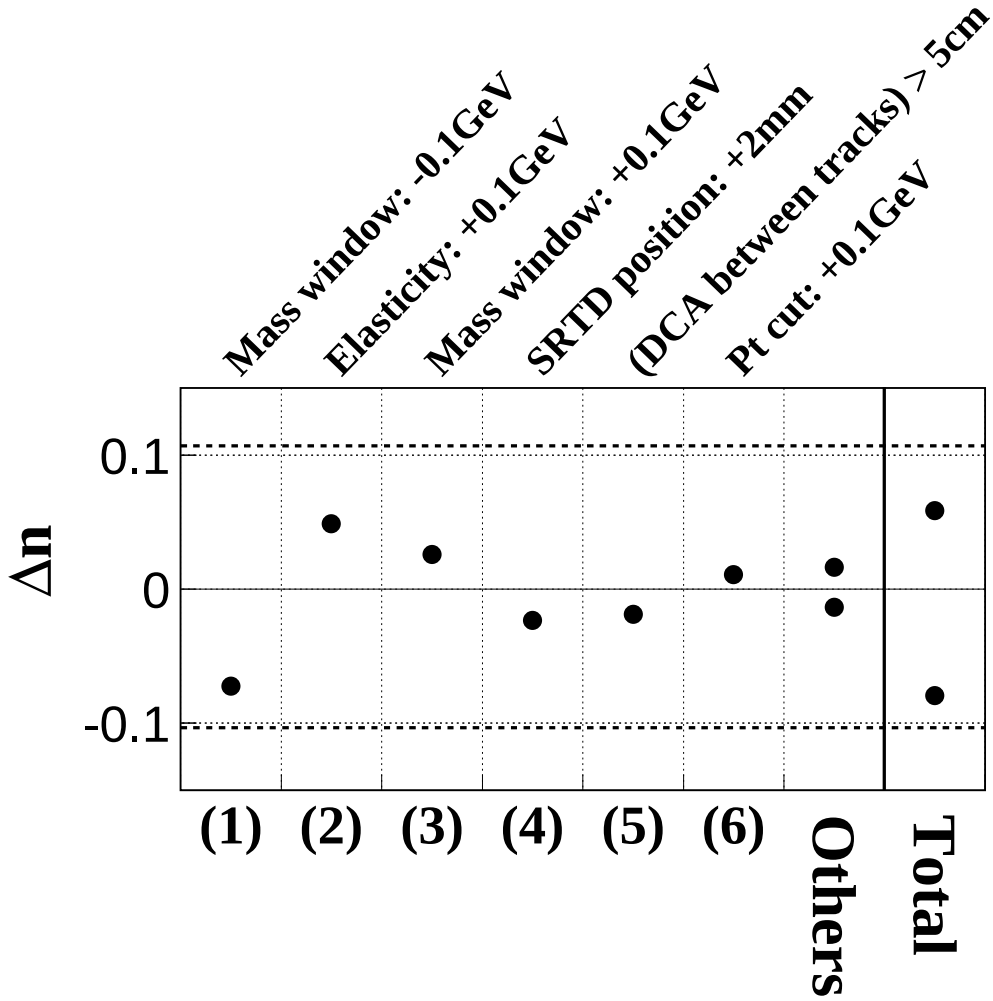

Figure 8.10: *Systematical errors on the Q^2-slope parameter n. The dashed-bold lines in the horizontal direction indicate a statistical error.*

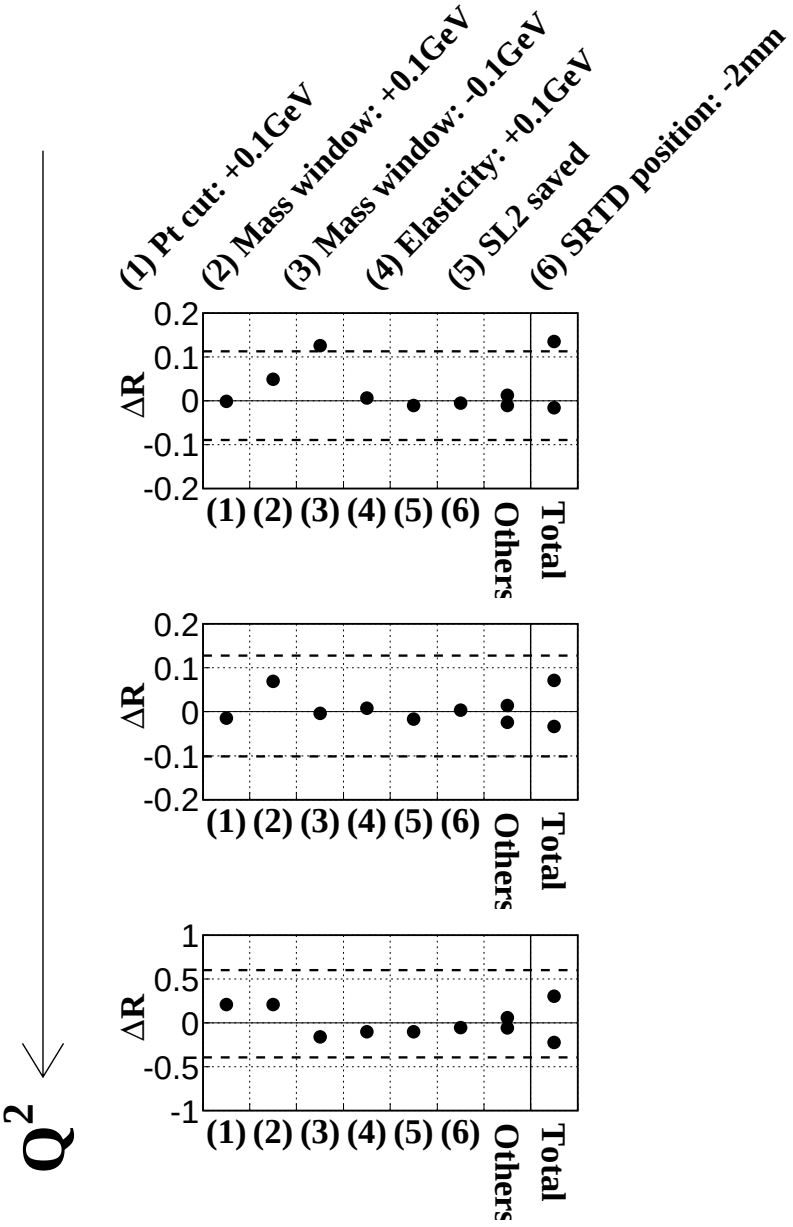

Figure 8.11: *Systematical errors on the* $R = \sigma_L^{\gamma^* p}/\sigma_T^{\gamma^* p}$. *The dashed-bold lines in the horizontal direction indicate a statistical error in the bin.*

for Figure 8.13. Those differences are within a level of the statistical fluctuation, so that the electron and muon channels are combined with no systematical error related to the difference between them.

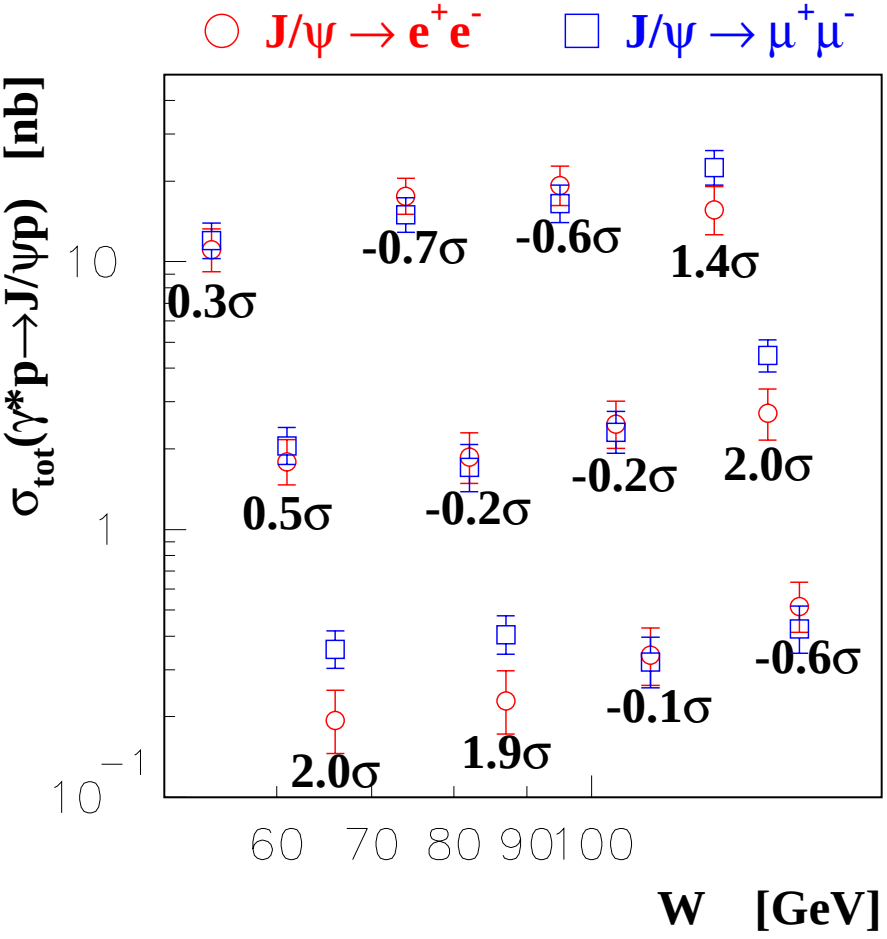

Figure 8.12: *Cross sections measured separately from the di-electron and from the di-muon channel for the W-slope measurement. The numbers below the plots are differences of the two divided by the combined error. Positive numbers mean a more cross section from the di-muon channel than from the di-electron.*

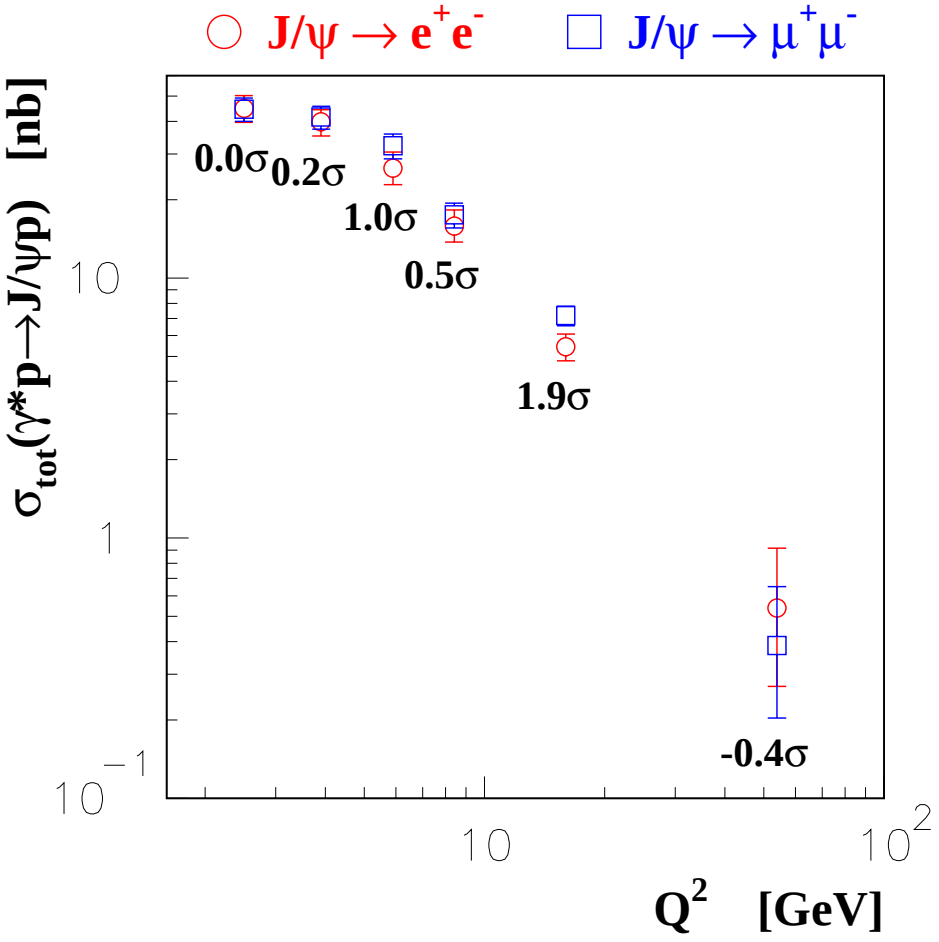

Figure 8.13: *Cross sections measured separately from the di-electron and di-muon channel for the Q^2-slope measurement. The numbers below the plots are differences of the two divided by the combined error. Positive numbers mean a more cross section from the di-muon channel than from the di-electron.*

Chapter 9

Results and Discussions

The final results of the cross-section measurement are presented in this chapter. On the plots of the cross section, vertical bars indicate a sum of statistical and systematical errors in quadrature, except for Figure 9.3 in which only statistical errors are taken into account. Statistical errors are shown as an interval between two small horizontal bars crossing the vertical one.

9.1 W-dependence

The W-dependence of the cross section is shown in Table 9.1 and Figure 9.1 at the Q^2 values of 3.1, 6.8, 16 and 54 GeV^2. This study has provided the first measurement of cross sections at $W \gtrsim 150$ GeV in vector-meson electroproduction. Also shown are the photoproduction results ($Q^2 = 0$) of ZEUS [2] and H1 [60] and the H1 electroproduction results [54]. For the H1 data in electroproduction, the cross sections at the Q^2 values of 3.5, 10.1 and 33.6 GeV^2 have been rescaled according to the Q^2-dependence from the H1 measurement.

The cross sections at the Q^2 values below 20 GeV^2 are fitted with a functional form of $\sigma_{tot}^{\gamma^* p \to J/\psi p}(W) \propto W^{\delta}$. The resulting δ values are

$$\begin{aligned}
\delta &= 0.69 \pm 0.12(stat.)\,^{+0.02}_{-0.05}(syst.) \quad \text{with } \chi^2/\mathrm{ndf} = 0.96/3 \quad \text{at } \mathrm{Q}^2 = 3.1\,\mathrm{GeV}^2, \\
\delta &= 0.70 \pm 0.15(stat.)\,^{+0.05}_{-0.09}(syst.) \quad \text{with } \chi^2/\mathrm{ndf} = 1.03/3 \quad \text{at } \mathrm{Q}^2 = 6.8\,\mathrm{GeV}^2, \\
\delta &= 0.59 \quad ^{+0.20}_{-0.19}(stat.)\,^{+0.05}_{-0.09}(syst.) \quad \text{with } \chi^2/\mathrm{ndf} = 0.96/3 \quad \text{at } \mathrm{Q}^2 = 16.0\,\mathrm{GeV}^2,
\end{aligned}$$

where systematical errors are not included in the χ^2 calculation. This is the first derivation of the W-slope from the ZEUS data. The cross sections are well-fitted with the above functional form, as in photoproduction [2], which is expected both by

the Regge theory and by the pQCD-based models. The results of the fit are shown in Figure 9.1 as a solid line together with the photoproduction result by ZEUS. Those δ values are also shown in the inset of Figure 9.1 as well as the H1 and ZEUS results. The obtained W-slopes in this analysis are similar to the photoproduction slope from ZEUS [2] $\left(0.65\pm0.09\right)$. Unlike the results on ρ^0 electroproduction [4], there is no indication for a strong increase of the W-slope as Q^2 increases.

The measured W-slopes are compared with the pQCD-based calculations from FKS using CTEQ4M [61] and MRT using CTEQ5M [20], as seen in the inset of Figure 9.1. The predictions from those theories show systematically steeper W-slopes. For the prediction from MRT using CTEQ5M, which is the case of the less δ values, the difference between the prediction and the data is quantified as $\chi^2/(number\ of\ points) = 6.9/3\,(stat. \oplus syst.)$. The tendency of the steep W-slopes remains with other gluon densities and with other potential models for the J/ψ wave function (Figure 3.9, p.21). On the other hand, the obtained δ values are significantly larger than that from the soft Pomeron exchange.

9.2 Q^2-dependence

The Q^2-dependence of the cross section at $W = 90\,\mathrm{GeV}$ is shown in Table 9.2 and Figure 9.2. The measured cross sections are fitted in the range of $Q^2 > 2\,\mathrm{GeV}^2$ with a functional form of $\sigma_{tot}^{\gamma^* p \to J/\psi\, p}(Q^2) \propto 1/(Q^2 + M_{J/\psi}^2)^n$. The resulting value is $n = 2.70\,^{+0.11}_{-0.10}(stat.)\,^{+0.06}_{-0.08}(syst.)$ with $\chi^2/ndf = 5.2/4\,(stat.\,only)$. This is the first derivation of the Q^2-slope from the ZEUS data. The obtained slope is significantly steeper than that predicted from the VDM ($n = 2$). The result of this fit is drawn as a solid line in Figure 9.2. The cross sections of this analysis are well-fitted with the above function. However, the extrapolation of the fit overshoots the cross sections in photoproduction measured by ZEUS [2] and H1 [60]. Another fit is performed in the range of $Q^2 < 10$ GeV^2, including the ZEUS photoproduction cross section [2], yielding $n = 2.00\,^{+0.11}_{-0.10}$ with $\chi^2/ndf = 6.4/3\,(stat. \oplus syst.)$. Therefore, the Q^2-dependence of the cross section over photo- and electroproduction can not be parameterized with a single value of the parameter: n.

The results are also compared with the predictions from FKS using CTEQ4M and MRT using CTEQ5M. Both models describe the Q^2-slope of this measurement well. Since the prediction from FKS on the cross section underestimates the magnitude, it is normalized to the cross section of the ZEUS photoproduction measurement [2], multiplying it by a factor of 1.6. The magnitude of the MRT prediction is taken from

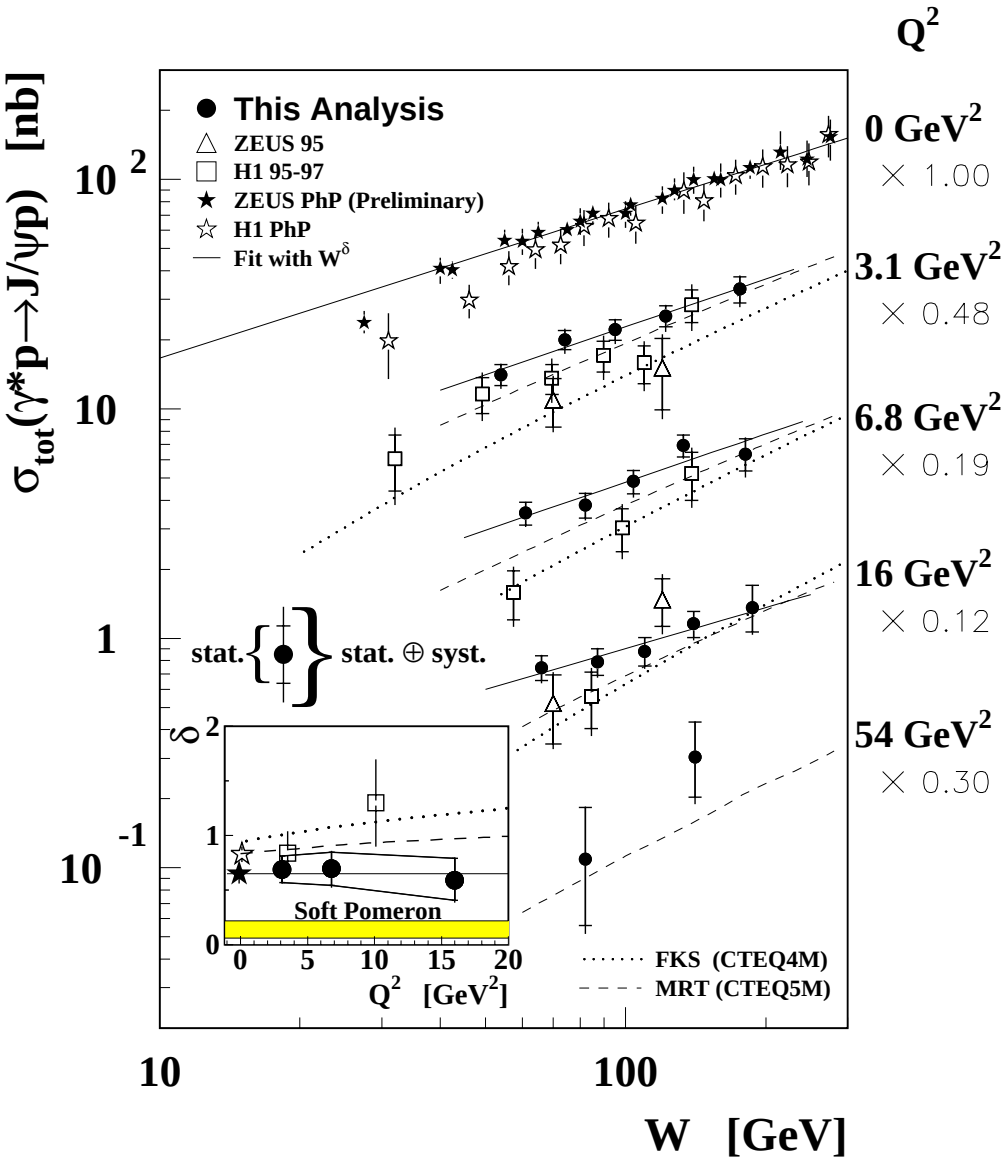

Figure 9.1: *The W-dependence of the cross section. The H1 cross sections at the Q^2 values of 3.5, 10.1 and 33.6 GeV^2 have been rescaled according to the Q^2-dependence from the H1 measurement. All of the cross sections have been scaled by a factor shown in the right margin at each Q^2 value. The solid lines are the results of the fit to the measurement of this analysis and the ZEUS photoproduction results using a functional form of W^δ. The resulting δ values are shown in the inset where the value for the ZEUS photoproduction (PhP) is drawn as a horizontal line. The predicted δ value from the soft Pomeron exchange is also put as a horizontal band. Superimposed are the pQCD-based calculations from Frankfurt et al. (FKS) using CTEQ4M (dotted lines) and from Martin et al. (MRT) using CTEQ5M (dashed lines). The normalizations are from those theories.*

Q_0^2 [GeV^2]	Q^2 range [GeV^2]	W_0 [GeV]	W range [GeV]	$\sigma_{tot}^{\gamma^* p \to J/\psi p}$ [nb]
3.1	$2-5$	54	$45-65$	$29.1 \pm 3.1 \,^{+1.9}_{-1.7}$
		74	$65-84$	$41.3 \pm 4.0 \,^{+3.4}_{-2.7}$
		95	$84-106$	$45.8 \pm 4.7 \,^{+3.4}_{-2.9}$
		122	$106-140$	$52.6 \pm 5.4 \,^{+3.3}_{-4.4}$
		176	$140-220$	$69.1 \pm 9.0 \,^{+4.7}_{-6.3}$
6.8	$5-10$	61	$50-72$	$18.3 \pm 2.1 \,^{+1.2}_{-0.7}$
		82	$72-93$	$19.9 \pm 2.4 \,^{+1.4}_{-1.0}$
		104	$93-116$	$25.2 \pm 3.0 \,^{+1.5}_{-1.8}$
		133	$116-150$	$36.2 \pm 3.9 \,^{+2.8}_{-1.5}$
		181	$150-220$	$33.2 \,^{+5.6\ +3.0}_{-5.0\ -4.5}$
16.0	$10-40$	66	$55-76$	$6.1 \pm 0.8 \,^{+0.4}_{-0.3}$
		87	$76-98$	$6.5 \pm 0.9 \,^{+0.5}_{-0.3}$
		110	$98-122$	$7.2 \pm 1.1 \,^{+0.4}_{-0.4}$
		140	$122-160$	$9.6 \pm 1.2 \,^{+0.5}_{-0.6}$
		187	$160-220$	$11.3^{+2.8\ +0.8}_{-2.4\ -1.1}$
54.0	$40-100$	82	$60-110$	$0.36 \,^{+0.24\ +0.06}_{-0.18\ -0.07}$
		141	$110-180$	$1.00 \,^{+0.43\ +0.10}_{-0.33\ -0.16}$

Table 9.1: *The W-dependence of the cross section. The first and second errors are statistical and systematical ones, respectively.*

Q_0^2 [GeV^2]	Q^2 range [GeV^2]	W_0 [GeV]	W range [GeV]	$\sigma_{tot}^{\gamma^* p \to J/\psi p}$ [nb]
2.5	$2.0 - 3.2$		$53 - 140$	$46.8 \pm 3.5 \,^{+3.2}_{-2.5}$
3.9	$3.2 - 5.0$		$53 - 140$	$41.8 \pm 3.1 \,^{+3.1}_{-3.0}$
5.9	$5.0 - 7.0$	90	$50 - 150$	$29.6 \pm 2.4 \,^{+1.7}_{-1.0}$
8.4	$7.0 - 10.0$		$50 - 150$	$17.3 \pm 1.4 \,^{+0.9}_{-0.5}$
16.0	$10 - 40$		$55 - 140$	$6.8 \pm 0.5 \,^{+0.4}_{-0.3}$
54.0	$40 - 100$		$60 - 140$	$0.46 \,^{+0.21\ +0.02}_{-0.16\ -0.07}$

Table 9.2: *The Q^2-dependence of the cross section. The first and second errors are statistical and systematical ones, respectively.*

its prediction, and is in a agreement with that from the data within 20 % differences. The Q^2 slope including the photoproduction measurement is well described by the FKS model, and not by the MRT one.

9.3 Ratio to ρ^0 Electroproduction

The Q^2-dependence of the cross section of J/ψ mesons is compared with that of the ρ^0 electroproduction measured by ZEUS [4]. Figure 9.3 shows the cross-section ratio at $W = 90\,\mathrm{GeV}$ as a function of Q^2. In the region of $Q^2 \gg M_V^2$, the different vector-meson cross sections are expected to show $\rho : \omega : \phi : J/\psi = 9 : 1 : 2 : 8$ according to the SU(4) flavor symmetry. In Figure 9.3, the measured ratio clearly indicates a rising behavior with Q^2 toward the SU(4) expectation: 8/9

The ratios of the cross sections of other vector mesons (ω, ϕ) with respect to the ρ^0 cross section as a function of Q^2 are summarized in [62]. The ratio for ϕ reaches the SU(4) expectation of 2/9 around the Q^2 value of $5\,\mathrm{GeV}^2$ which is about five times larger than M_ϕ^2. The result of this analysis supports an expectation of the same behavior also for the J/ψ, i.e., the ratio approaches the SU(4) value of 8/9 at $Q^2 \sim 50\,\mathrm{GeV}^2$, about five times larger than $M_{J/\psi}^2$.

9.4 Polarization of J/ψ mesons

Figure 9.4 shows the decay angular distributions of $\cos\theta_h$ and Ψ for the J/ψ meson in the Q^2 range: 2-5, 5-10 and 10-40 GeV^2. The vertical axes in Figure 9.4

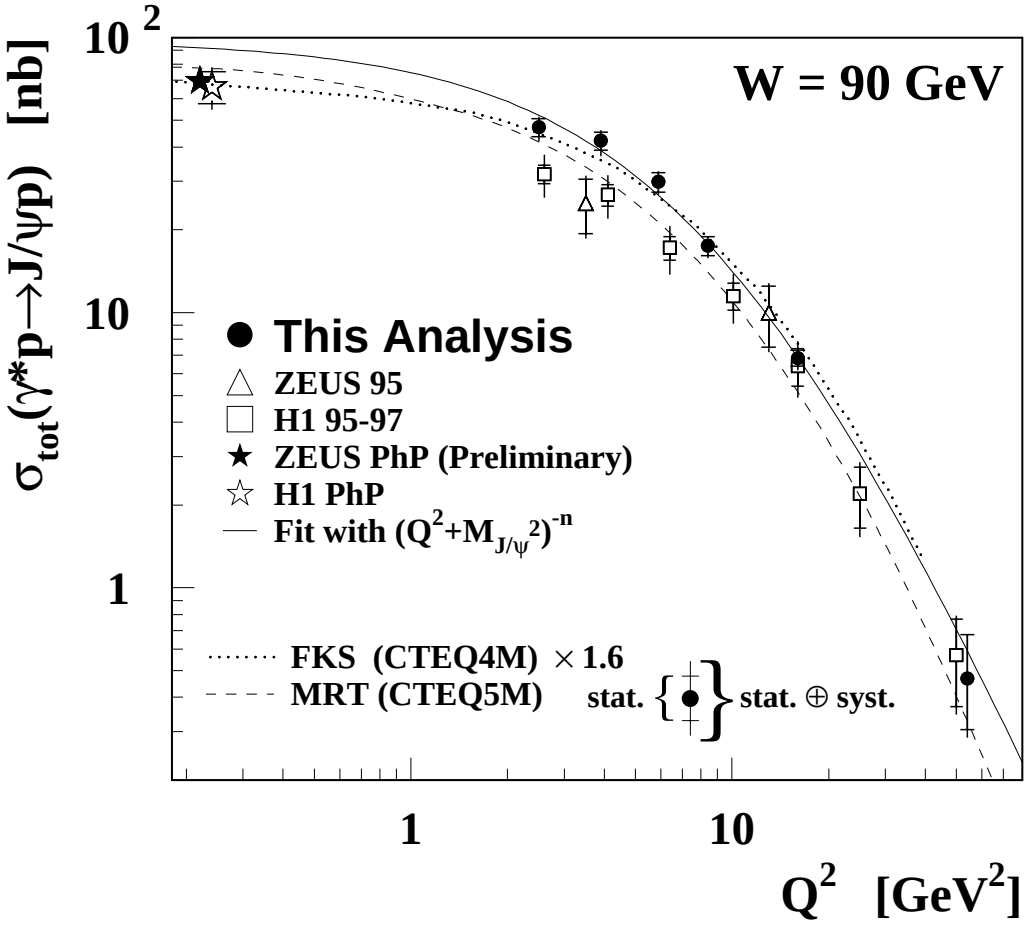

Figure 9.2: *The Q^2-dependence of the cross section. The solid line is a result of the fit to this measurement ($Q^2 > 2\,GeV^2$) using a functional form of $1/(Q^2 + M^2_{J/\psi})^n$. Superimposed are the pQCD-based calculations from Frankfurt et al. (FKS) using CTEQ4M (dotted lines) and from Martin et al. (MRT) using CTEQ5M (dashed lines). Since the prediction from FKS underestimates the magnitude, it is normalized (multiplied by about 1.6) to the ZEUS photoproduction measurement [2]. The magnitude of the MRT prediction is taken from its prediction.*

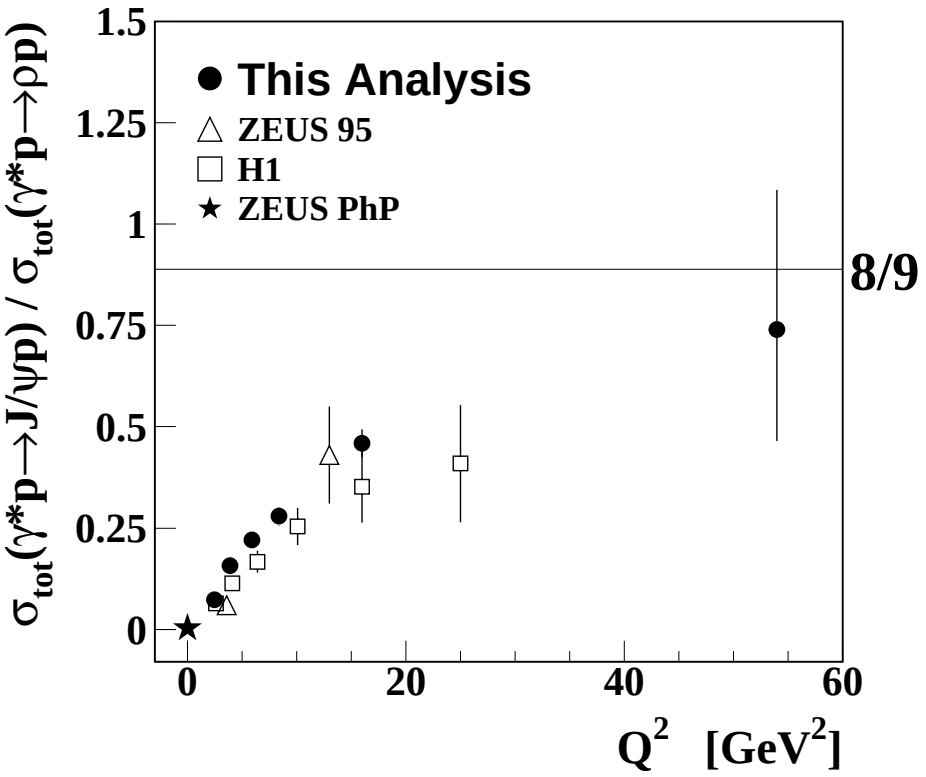

Figure 9.3: *Ratio to ρ^0 electroproduction cross section as a function of Q^2. Only the statistical errors are shown. See the text for more details.*

Q^2 range [GeV^2]	r^{04}_{00}	$r^{1}_{1\,-1}$
$2-5$	$0.05 \pm 0.09\,^{+0.11}_{-0.02}$	$0.43 \pm 0.10\,^{+0.03}_{-0.05}$
$5-10$	$0.05 \pm 0.10\,^{+0.06}_{-0.03}$	$0.32 \pm 0.10\,^{+0.03}_{-0.04}$
$10-40$	$0.51\,^{+0.11\,+0.07}_{-0.12\,-0.06}$	$0.24\,^{+0.12\,+0.08}_{-0.11\,-0.05}$

Table 9.3: *Spin density matrix elements: r^{04}_{00} and $r^{1}_{1\,-1}$. The first and second errors are statistical and systematical ones, respectively.*

indicate the ep cross section for the process: $ep \to epJ/\psi \to epl^+l^-$. The spin density matrix elements of r^{04}_{00} and $r^{1}_{1\,-1}$ are obtained by fitting the distributions of $\cos\theta_h$ and Ψ with a functional form in (3.25) and (3.28), respectively. The resulting values are shown in Table 9.3. The results of the fits are also shown in Figure 9.4 as a solid line. These results on r^{04}_{00} and $r^{1}_{1\,-1}$ are consistent with the relation (3.27) which holds on the assumptions of the SCHC and NPE. The previous analyses of the helicity angles in both photoproduction [63] and electroproduction [3] of ρ^0 mesons suggest that the SCHC holds to a good approximation.

Under the SCHC, the ratio of the longitudinal to transverse cross sections, $R = \sigma_L/\sigma_T$, is derived according to the formula (3.26). The resulting values are

$$R = 0.05\,^{+0.11}_{-0.09}(stst.)\,^{+0.15}_{-0.02}(syst.) \quad \text{at} \quad Q^2 = 3.1\,\text{GeV}^2, \tag{9.1}$$

$$R = 0.06\,^{+0.13}_{-0.10}(stst.)\,^{+0.08}_{-0.03}(syst.) \quad \text{at} \quad Q^2 = 6.8\,\text{GeV}^2, \tag{9.2}$$

$$R = 1.04\,^{+0.60}_{-0.39}(stst.)\,^{+0.42}_{-0.17}(syst.) \quad \text{at} \quad Q^2 = 16\,\text{GeV}^2. \tag{9.3}$$

The above values are shown in Figure 9.5 together with the H1 results [54]. The positive non-zero value of R at $Q^2 = 16$ GeV^2 from the H1 measurement has been confirmed, and R has proven to show a rising behavior with Q^2. The values of R are about one order of magnitude smaller than those measured in the ρ electroproduction at the same Q^2 [4]. However, the measured values are consistent with the fitted parameterization of R for ρ [4] (the upper dashed-dotted line) replacing the ρ mass by the J/ψ mass (the lower dashed-dotted line). This fact suggests the universality on the parameterization for R. The MRT calculation in (3.18) (p.19) shows a good agreement within the error of the measurement, and gives a better description than the naive pQCD prediction of $R = Q^2/M^2_{J/\psi}$.

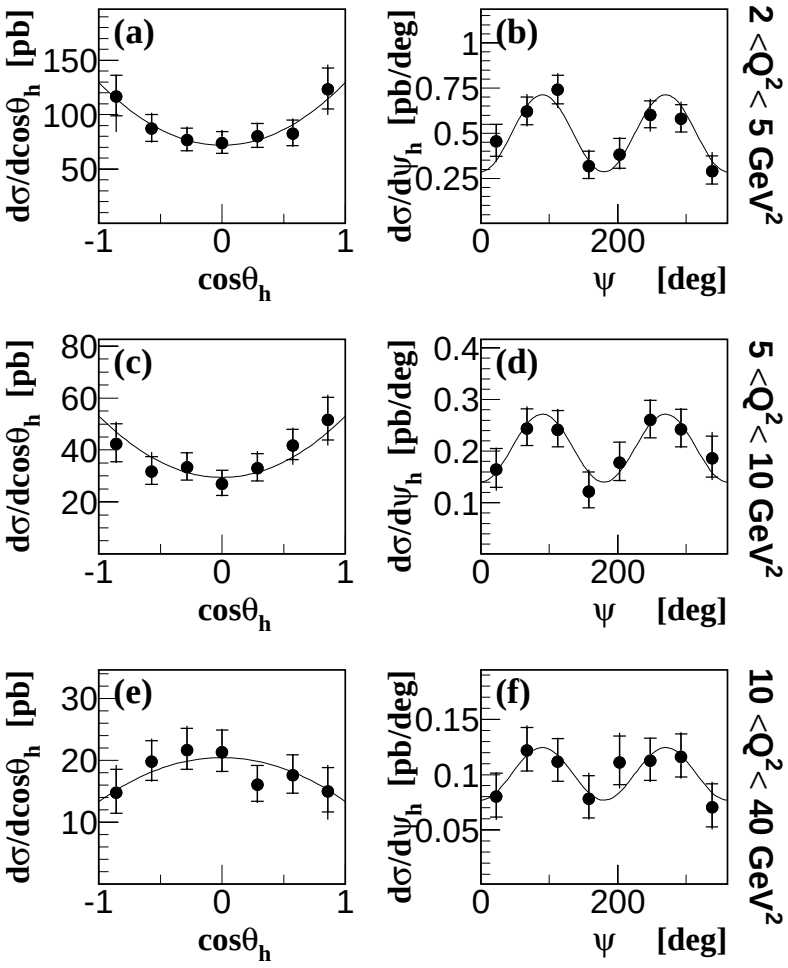

Figure 9.4: *Decay angular distributions of J/ψ mesons in the three Q^2 regions. The vertical axes indicate the ep cross sections for the process: $ep \to eJ/\psi\, p$, $J/\psi \to l^+l^-$.*

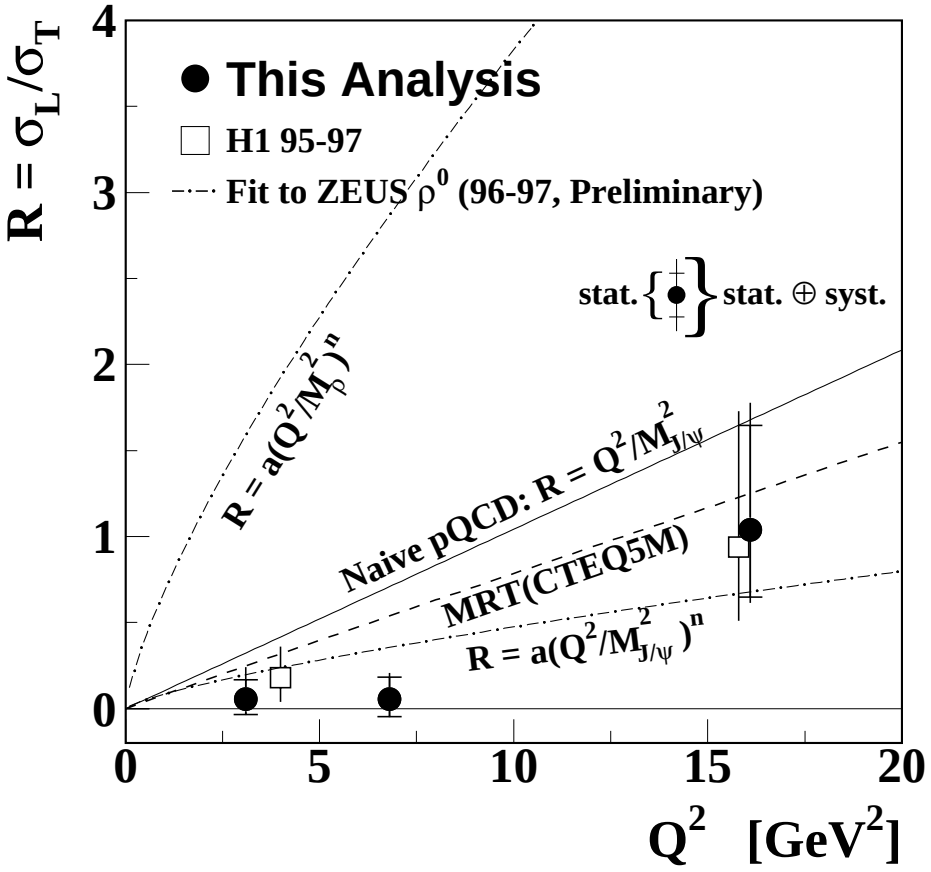

Figure 9.5: *Ratio of longitudinal to transverse cross section, $R = \sigma_L/\sigma_T$, as a function of Q^2. The parameter values are $a = 0.46$ and $n = 0.75$, which are extracted from the ZEUS results on ρ^0 electroproduction [4].*

9.5 Conclusions for the Test of the pQCD-based Predictions

Both the two pQCD-based models from FKS and MRT, which have different approaches to the J/ψ state, give a good description of the data in electroproduction on the Q^2-dependence of the cross section which is sensitive to the treatment of the J/ψ state. The MRT model also gives a good description on the ratio of $R = \sigma_L/\sigma_T$ as a function of Q^2 though the statistical errors of the measurement are large. On the other hand, the measured W-slopes of the cross section, which is related to the slope of the gluon density in the low-x regime of the proton, are less steeper than any prediction at any Q^2 value of the measurement, so that a better theoretical understanding is required. The absolute size of the measured cross section is fairly well reproduced with the MRT model.

Chapter 10

Summary and Conclusions

Exclusive electroproduction of J/ψ mesons at HERA has been studied, via its dilepton decay channels, using a ten-times more integrated luminosity than that used in the previous ZEUS results.

The W-dependence of the cross section has been measured at Q^2 values of 3.1, 6.8, 16.0 and 54.0 GeV^2. The measurement is first extended to the higher-W region ($W \gtrsim 150$ GeV), which helps an improvement on the W-slope measurement. The measured cross sections are well-fitted with a functional form of W^δ. The resulting δ values are $0.69 \pm 0.12(stat.)^{+0.02}_{-0.05}(syst.)$, $0.70 \pm 0.15(stat.)^{+0.05}_{-0.09}(syst.)$ and $0.59^{+0.20}_{-0.19}(stat.)^{+0.05}_{-0.09}(syst.)$ at $Q^2 =$ 3.1, 6.8 and 16.0 GeV^2, respectively. These values are significantly larger than that from the soft Pomeron exchange, and are consistent with the value measured in J/ψ photoproduction. The δ does not show a strong Q^2-dependence which is expected from the naive pQCD model. The improved pQCD-based calculations from FKS and MRT still predict larger δ values. This tendency cannot be improved with the change of the gluon density parameterization and of the model for the J/ψ state. A better theoretical understanding is required.

The Q^2-dependence of the cross section has been measured at $W = 90$ GeV. The measured cross sections are well-fitted with a functional form of $1/(Q^2 + M^2_{J/\psi})^n$, resulting in $n = 2.70^{+0.11}_{-0.10}(stat.)^{+0.06}_{-0.08}(syst.)$. The extrapolation of the fit, however, overshoots the photoproduction cross section, which means that exclusive J/ψ photo- and electroproduction cannot be parameterized with a single value of the parameter : n. The measured Q^2-slope is significantly steeper than that predicted by the VDM. The measured cross sections are compared with the predictions from the pQCD-based models. The absolute normalization of the predictions is lower by $\sim 60\%$

for the FKS calculation and by $\sim 20\%$ for the MRT calculation. The pQCD-based models provide a fairly well prediction on the Q^2-slope, especially the FKS model gives a good description on the slope over the photo- and electroproduction regime.

The helicity state of J/ψ mesons has been measured from the decay angular distribution. This measurement is consistent with the SCHC. Assuming the SCHC, the ratio of $R = \sigma_L/\sigma_T$ is extracted as a function of Q^2, resulting in $0.05\,^{+0.11}_{-0.09}(stst.)\,^{+0.15}_{-0.02}(syst.)$, $0.06\,^{+0.13}_{-0.10}(stst.)\,^{+0.08}_{-0.03}(syst.)$ and $1.04\,^{+0.60}_{-0.39}(stst.)\,^{+0.42}_{-0.17}(syst.)$ at $Q^2 =$ 3.1, 6.8 and 16.0 GeV^2, respectively. A rising behavior with Q^2 has been observed, which is consistent with the parameterization from the ρ^0 measurement once replacing the ρ^0 mass by the J/ψ mass. The MRT calculation shows a good agreement within the error of this measurement.

Acknowledgments

I am very thankful to Prof. S. Yamada for his supervision and giving me a chance into the field of particle physics. I am also grateful to Prof. K. Tokushuku for his many instructive comments and various supports throughout my research activities. Dr. M. Kuze gave me tutorials at DESY on how to analyze the data and how to present results. I do not know how to express my thanks for his kindness. Dr. Y. Yamazaki was not only my master but also my good friend both in my research activities and in my private life. I again do not know how to express my thanks for his kindness. I am very glad that I enjoyed research activities together with the other ZEUS-Japan members: R. Hamatsu, S. Kitamura, Y. Iga, T. Tsurugai, M. Inuzuka, K. Nagano, T. Fusayasu, T. Nishimura, T. Yamashita, T. Kohno, S. Kagawa, T. Tawara and the senior members who have already left ZEUS-Japan: S. Mine, I. Suzuki, K. Homma, K. Yamauchi, K. Umemori and T. Matsushita.

I was doing this analysis at DESY with R. Ciesielski. We had been through a lot together, in both good times and bad. I am very proud of having the same work with him. I cannot forget worthwhile advice from B. Mellado, which were always very instructive. This analysis was supported also by Prof. H. Abramowicz and Prof. A. Levy. I am deeply grateful to them. I also would like to thank A. Kreisel, A. Gabareen and other ZEUS members for the collaboration.

It was precious to have a discussion with M. Strikman and T. Teubner on the theoretical aspects of J/ψ production. I gratefully acknowledge their favors and giving me their model predictions.

I spent much time and energy in my doctor course on the development of MC event generators for HERA physics using the automatic calculation system `GRACE`. Prof. Y. Shimizu, a leader of the Minami-Tateya group, was kindly accepted me to the group. I will never forget the joint work in the previous southern prefab in KEK. I would like to give my thanks from the bottom of my heart to the members of the Minami-Tateya group: J. Fujimoto, T. Ishikawa, M. Jimbo, T. Kaneko, K. Kato, S. Kawabata, T. Kon, Y. Kurihara, M. Kuroda, T. Munehisa, N. Nakazawa,

H. Tanaka, K. Tobimatsu, T. Watanabe and F. Yuasa.

Finally I would like to express my gratitude to my parents, grandparents and grandaunts for their understanding and supports.

Bibliography

[1] J.J. Sakurai, Phys. Rev. Lett. **22** (1969) 981.

[2] ZEUS Collaboration, Paper contribution to XXXth International Conference on High Energy Physics ICHEP2000 (2000) Paper 437.

[3] ZEUS Collaboration, J. Breitweg et al., Eur. Phys. J. **C6** (1999) 603–627; H1 Collaboration, C. Adloff et al., Eur. Phys. J. **C13** (2000) 371–396.

[4] ZEUS Collaboration, Paper contribution to XXXth International Conference on High Energy Physics ICHEP2000 (2000) Paper 439.

[5] J.J. Sakurai, D. Schildknecht, Phys. Lett. **B40** (1972) 121.

[6] P.D.B. Collins, *An Introduction to Regge Theory and High Energy Physics* (Cambridge University Press, 1977).

[7] A. Donnachie, P.V. Landshoff, Phys. Lett. **B296** (1992) 227.

[8] ZEUS Collaboration, M. Derrick et al., Z. Phys. **C63** (1994) 391.

[9] H1 Collaboration, S. Aid at al., Z. Phys. **C69** (1995) 27.

[10] M.G. Ryskin, Z. Phys. **C57** (1993) 89–92.

[11] C. Collins, L. Frankfurt, M. Strikman, Phys. Rev. **D56** (1997) 2982–3006.

[12] E.M. Levin, A.D. Martin, M.G. Ryskin, T. Teubner, Z. Phys. **C74** (1997) 671.

[13] J.A. Crittenden, hep-ex/9704009 (1997) .

[14] L. Frankfurt, W. Koepf, M. Strikman, Phys. Rev. **D57** (1998) 512.

[15] S.J. Brodsky, L. Frankfurt, J.F. Gunion, A.H. Mueller, M. Strikman, Phys. Rev. **D50** (1994) 3134–3144.

[16] L. Frankfurt, W. Koepf, M. Strikman, Phys. Rev. **D54** (1996) 3194–3215.

[17] A.D. Martin, M.G. Ryskin, T. Teubner, Phys. Rev. **D62** (2000) 014022.

[18] A.D. Martin, M.G. Ryskin, T. Teubner, Phys. Rev. **D55** (1997) 4329–4337.

[19] E. Kuraev, L. Lipatov, V. Fadin, Sov. Phys. JETP **44** (1976) 443; **45** (1977) 199; Y. Balitskii, L. Lipatov,, Sov. J. Nucl. Phys. **28** (1978) 822.

[20] H.L. Lai et al., Eur. Phys. J. **C12** (2000) 375.

[21] M. Glück, E. Reya and A. Vogt, Eur. Phys. J. **C5** (1998) .

[22] A.D. Martin et al., Eur. Phys. J. **C14** (2000) 133.

[23] K. Schilling and G. Wolf, Nucl. Phys. **B61** (1973) 381–413.

[24] ZEUS Collaboration, The ZEUS Detector, Status Report 1993, 1993.

[25] B. Foster et al., Nucl. Inst. Meth. **A338** (1994) 254.

[26] R. Hall-Wilton et al., The CTD Tracking Resolution, ZEUS-Note 99-024, 1999.

[27] A. Andresen et al., Nucl. Instrum. Methods **A309** (1991) 101; M. Derrick et al., Nucl. Inst. Meth. **A309** (1991) 77; A. Bernstein et al., Nucl. Inst. Meth. **A336** (1993) 23.

[28] G. Abbiendi et al., Nucl. Inst. Meth. **A333** (1993) 342.

[29] ZEUS Collaboration, Proposal for a Small Angle Rear Tracking Detector for ZEUS, ZEUS-Note 93-016, 1993; A. Bamberger et al., The Small Angle Rear Tracking Detector for ZEUS, ZEUS-Note 95-095, 1995.

[30] F. Goebel, private communication, 2000.

[31] A. Bamberger et al., Nucl. Instrum. Methods **A450** (2000) 235–252.

[32] A. Kwiatkowski, H. Spiesberger, H.J. Mohring, Comput. Phys. Commun. **69** (1992) 155–172.

[33] E. Barberio and Z. Was, Comput. Phys. Commun. **79** (1994) 291–308.

[34] T. Abe, Comput. Phys. Commun. **136** (2001) 126–147; T. Abe, hep-ph/0012029; Homepage: `http://www.awa.tohoku.ac.jp/~tabe/grape/`; T. Abe and J. Fujimoto and T. Ishikawa and K. Kato and Y. Kurihara and T. Watanabe, in *Proceedings of the workshop on Monte Carlo Generators for HERA Physics*, ed. A. T. Doyle and G. Grindhammer and G. Ingelman and H. Jung, DESY, 1999, pp. 566–575.

[35] T. Ishikawa, T. Kaneko, K. Kato, S. Kawabata, Y. Shimizu, H. Tanaka, GRACE manual, KEK-report 92-19, 1993.

[36] F.W. Brasse et al., Nucl. Phys. **B110** (1976) 413.

[37] H. Abramowicz, A. Levy, The ALLM parameterization of $\sigma_{tot}(\gamma^* p)$ an update, DESY-97-251 (hep-ph/9712415), 1997.

[38] A. Mücke et al., Comput. Phys. Commun. **124** (2000) 290.

[39] J. Fujimoto, M. Igarashi, N. Nakazawa, Y. Shimizu and K. Tobimatsu, Prog. Theor. Phys. Suppl. **100** (1990) 285.

[40] H. Burkhardt, B. Pietrzyk, Phys. Lett. **B356** (1995) 398.

[41] T. Sjöstrand, Comput. Phys. Commun. **82** (1994) 74.

[42] R. Brun et al., GEANT 3.13, CERN DD/EE/84-1, 1987.

[43] A. Savin, Study of Calorimeter Noise in the 1996 data, ZEUS-Note 98-007, 1998.

[44] R. Sinkus, T. Voss, Nucl. Instr. Meth. **A391** (1997) 360–368.

[45] M. Wodarczyk, *Measurement of the F_2 structure function of the proton at HERA from 1996 and 1997 ZEUS Data*, Ph.D. thesis, University of Wisconsin, 1999.

[46] T. Doeker, A. Frey, M. Nakao, Electron Position Reconstruction — Update of the ELECPO routines, ZEUS-Note 94-123, 1994; Ch. Amelung, Electron Position Reconstruction in ZEUS: Further Update of the ELECPO Package, ZEUS-Note 96-093, 1996; Ch. Amelung, Another Update of the ELECPO Package, ZEUS-Note 97-053, 1997.

[47] J. Ng., W. Verkerke, An Overview of SRTD Analysis, ZEUS-Note 95-037, 1995.

[48] R. Deffner, *Measurement of the proton structure function F_2 at HERA using the 1996 and 1997 ZEUS Data*, Ph.D. thesis, University of Bonn, 1999.

[49] Particle Data Group, Eur. Phys. J. **C15** (2000) .

[50] B. Mellado, Elastic Photoproduction of $\Upsilon \to e^+e^-$, ZEUS-Note 99-055, 1999.

[51] A. Arbuzov et al., Comput. Phys. Commun. **94** (1996) 128–184.

[52] ZEUS Collaboration, M. Derrick et al., Phys. Lett. **B356** (1995) 601–616.

[53] Y. Yamazaki, private communication, 2000.

[54] H1 Collaboration, C. Adloff et al., Eur. Phys. J. **C10** (1999) 373–393.

[55] A. Akhundov et al., Fortsch. Phys. **44** (1996) 373.

[56] F. James, M. Roos, Comput. Phys. Commun. **10** (1975) 343–367.

[57] A. Quadt, O. Ruske, A New Method to Measure Vertex Distributions, ZEUS-Note 98-036, 1998.

[58] J.R. Goncalo, K. Long, A minimum bias vertex distribution for the 1998/99 e^-p data, ZEUS-Note 00-027, 2000.

[59] K. Olkiewicz and A. Eskreys, Off-line Luminosity Calculation in the ZEUS Experiment in 1997, 1998 and 1999, ZEUS-Note 99-044, 1999.

[60] H1 Collaboration, C. Adloff et al., Phys. Lett. **B483** (2000) 23–35.

[61] H.L. Lai et al., Phys. Rev. **D55** (1997) 1280.

[62] ZEUS Collaboration, J. Breitweg et al., Phys. Lett. **B487** (2000) 273–288.

[63] ZEUS Collaboration, M. Derrick et al., Z. Phys. **C69** (1995) 39–54; ZEUS Collaboration, M. Derrick et al., Z. Phys. **C73** (1997) 253–268; H1 Collaboration, S. Aid et al., Nucl. Phys. **B463** (1996) 3–32; ZEUS Collaboration, J. Breitweg et al., Eur. Phys. J. **C12** (2000) 393–410.

[64] ZEUS Collaboration, Status of the Uranium Calorimeter Reconstruction Software, ZEUS-Note 92-019, 1992.

[65] L.L. Wai, Ph.D. thesis, Columbia University, 1995.

[66] G.M. Briskin, *Diffractive Dissociation in ep Deep Inelastic Scattering*, Ph.D. thesis, Tel Aviv University, 1998.

Appendix A

Calorimeter Clustering Algorithms

A.0.1 Condensates

A condensate [64] is defined as a cluster of adjacent cells with energy deposits. In this algorithm, diagonally-adjacent cells are not merged, and adjacent cells over different sections, the EMC and HAC1 or the HAC1 and HAC2, are merged. A connection over a crack between the FCAL and BCAL or the BCAL and RCAL is not allowed.

A.0.2 Tower-islands

The algorithm to form *tower-islands* [65] is based on energy gradients. The tower-island clustering is performed tower-by-tower basis, i.e., cells in a tower are merged into one object. Each tower is connected to a neighboring tower which has the highest energy among the neighborhood. If the energy of the tower itself is higher than that of any neighborhood, the tower is called *a local maximum*. Towers belonging to one local maximum are merged into one tower-island. In this algorithm, diagonally-adjacent towers are merged, and a connection over a crack between the FCAL and BCAL or the BCAL and RCAL is allowed. A schematic view of the island clustering is shown in Figure A.1.

A.0.3 Cone-islands

The same algorithm as for tower-islands is used to form *cell-islands* [66] except for the unit of the clustering. The cell-island clustering is performed cell-by-cell

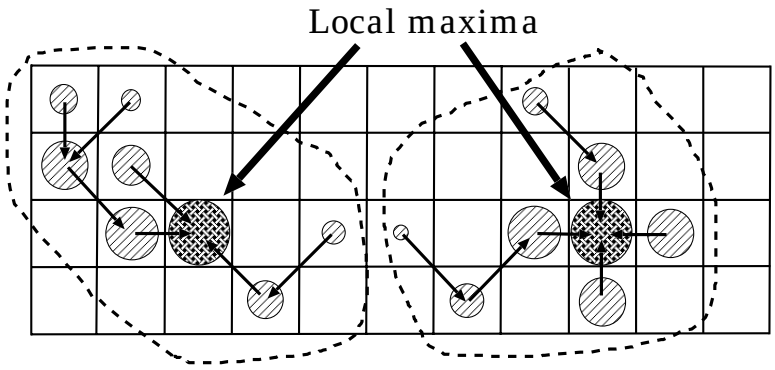

Figure A.1: *A schematic view of the island clustering based on energy gradients. The squares indicate a unit of clustering: towers for tower-islands or cells for cell-islands. The size of circles shows a size of the energy deposit in the unit. In this figure, two islands are formed, each of which is surrounded with a dashed line.*

basis. In this algorithm, a connection over a crack between the FCAL and BCAL or the BCAL and RCAL is allowed. However, a connection is not allowed between neither the EMC and HAC1 nor the HAC1 and HAC2. This is a pre-stage of the following cone-island clustering.

A cone-island [66] is defined as a cluster of cell-islands in a specified cone in the $\theta - \phi$ space. In this algorithm, cell-islands in the sections of the EMC and HAC, and the FCAL and BCAL or the BCAL and RCAL are merged if those are in the same cone. A proper primary vertex position is needed to be input in order to make a cone.

This clustering algorithm gives a good correspondence between a final state particle and a cluster in the CAL, especially for muons.

Appendix B

Detailed Description of the Trigger Logic

B.0.4 FLT (slot30)

All of the following conditions are required.

- Energy deposits in the RCAL with
  - ▷ $E_{REMC} \geq 2032\,MeV$ excluding the first inner ring
    OR
  - ▷ $E_{REMC} \geq 5000\,MeV$ including the first inner ring,

  where E_{REMC} indicates an energy in the REMC.

- At least one isolated electromagnetic cluster in the RCAL.

B.0.5 SLT (slot DIS6)

All of the following conditions are requied.

- Energy deposits in the CAL with
  - ▷ $E_{REMC} > 2.5\,GeV$ OR
  - ▷ $E_{BEMC} > 2.5\,GeV$ OR
  - ▷ $E_{FEMC} > 10\,GeV$ OR
  - ▷ $E_{FHAC} > 10\,GeV$,

  where E_{REMC}, E_{BEMC}, E_{FEMC} and E_{FHAC} indicate energies in the REMC, BEMC, FEMC and FHAC, respectively.

- $E - Pz + 2\,E_{lumi-\gamma} > 29\,\mathrm{GeV}$,
  where $E - Pz$ is calculated from energy deposits in CAL cells using the origin as a primary vertex: $(X_{VTX}, Y_{VTX}, Z_{VTX}) \equiv (0,0,0)$, and $E_{lumi-\gamma}$ indicates an energy measured with the LUMI-γ.

- The SLT vetos to reject events having an inconsistent timing with ep interactions. All of the following conditions are required.

  ▷ $|\mathtt{t_{RCAL}}| < 8\,\mathrm{ns}$,
  ▷ $|\mathtt{t_{FCAL}}| < 8\,\mathrm{ns}$,
  ▷ $|\mathtt{t_{FCAL}} - \mathtt{t_{RCAL}}| < 8\,\mathrm{ns}$,
  ▷ $|\mathtt{t_{global}}| < 8\,\mathrm{ns}$ and
  ▷ $|\mathtt{t_{up}} - \mathtt{t_{down}}| < 8\,\mathrm{ns}$,

  where $\mathtt{t_{FCAL}}$, $\mathtt{t_{RCAL}}$, $\mathtt{t_{global}}$, $\mathtt{t_{up}}$ and $\mathtt{t_{down}}$ are calorimeter timings calculated from cells in the FCAL, RCAL, CAL, the upper half of the CAL, and the lower half of the CAL, respectively.

B.0.6 TLT (slot DIS05) for the medium-W sample

All of the following conditions are required.

- $E - P_z + 2\,E_{lumi-\gamma} > 30\,\mathrm{GeV}$,
  where $E - Pz$ is calculated from energy deposits in CAL cells with the primary vertex position reconstructed using CTD tracks.

- Using at least one of the three different algorithms of electron finding, a scattered electron is required to be found with the following conditions:

  ▷ $E_e > 7\,\mathrm{GeV}$ AND
  ▷ $\left\{\ |X_e| > 12\,\mathrm{cm}\ \ \mathrm{OR}\ \ |Y_e| > 6\,\mathrm{cm}\ \right\}$ AND
  ▷ $E_{CAL} - E_{Fbp} - E_e < 30\,\mathrm{GeV}$,

  where E_e and (X_e, Y_e) are an energy and a position of the scattered electron, respectively, and E_{CAL} and E_{Fbp} are energies in the CAL and in the first inner ring of the FCAL, respectively.

- $E_{Fbp} < 5\,\mathrm{GeV}$.

- Number of CTD tracks should be from 2 to 5.

- Number of CTD tracks which are fitted to the reconstructed primary vertex should be greater than zero.

B.0.7 TLT (slot DIS06) for the high-W sample

All of the following conditions are required.

- $E - P_z + 2\,E_{lumi-\gamma} > 30\,\mathrm{GeV}$,
  where $E - Pz$ is calculated from energy deposits in CAL cells with the primary vertex position reconstructed using CTD tracks.
- Using at least one of the three different algorithms of electron finding, a scattered electron is required to be found with the following conditions:
  - ▷ $E_e > 4\,\mathrm{GeV}$ AND
  - ▷ $\left\{\ |X_e| > 12\,\mathrm{cm}\ \ \mathrm{OR}\ \ |Y_e| > 6\,\mathrm{cm}\ \right\}$.
- An energy measured with the FPC should be less than 20 GeV.

Appendix C

Combining Different Samples

Data sets with different proton-beam energies are combined at the level of the ep Born cross section at $\sqrt{s} = 318\,\mathrm{GeV}$ using the following correction factor for each bin:i,

$$\mathcal{C}_s \;=\; \frac{\sigma^{ep}_{Born}(i)_{\sqrt{s}=318\,\mathrm{GeV}}}{\sigma^{ep}_{Born}(i)_{\sqrt{s}=300\,\mathrm{GeV}}}. \tag{C.1}$$

The ep cross sections at $\sqrt{s} = 300\,\mathrm{GeV}$ are translated into ones at $\sqrt{s} = 318\,\mathrm{GeV}$, and quoted at $\sqrt{s} = 318\,\mathrm{GeV}$. The factor $\mathcal{C}_s$ is mainly determined from the difference between two photon fluxes at different $\sqrt{s}$ values, and almost independent of the form of the total cross section. This is checked using Eq.(8.6) in p.94. Substituting Eq.(2.17) and Eq.(8.6) for Eq.(8.3), numerical values of $\mathcal{C}_s$ in each bin are found to be from 1.004 up to 1.034. The uncertainty of $\mathcal{C}_s$ on the parameter values of n and δ in Eq.(8.6) is also estimated. Calculating the quantity:

$$\mathcal{C}_s(i)_{n=n',\delta=\delta'} - \mathcal{C}_s(i)_{n=n'',\delta=\delta''}$$

with different values of n', δ', n'' and δ'' in the parameter range: $1.0 < n < 5.0$ and $0.1 < \delta < 2.0$, it is found to be less than 0.003 in all of the bins. Therefore, the model dependence is small and negligible.

Taking a large statistics limit, the expectation value for the number of J/ψ candidates can be expressed as follows for each proton-beam energy and each channel

from Eqs. (8.1), (8.3) and (C.1),

$$(N_{obs}^{DATA} - N_{QED}^{MC})_{e^+e^-}^{96-97} = \frac{\sigma_{Born}^{ep} \cdot L_{96-97} \cdot \mathcal{A}_{e^+e^-}^{96-97} \cdot \mathcal{B}_{e^+e^-}}{\mathcal{C}_{Rad}^{96-97}\mathcal{C}_s\left(1 - f_{pd}^{96-97}\right)\left(1 - f_{\psi'}^{e^+e^-}\right)}, \quad \text{(C.2)}$$

$$(N_{obs}^{DATA} - N_{QED}^{MC})_{\mu^+\mu^-}^{96-97} = \frac{\sigma_{Born}^{ep} \cdot L_{96-97} \cdot \mathcal{A}_{\mu^+\mu^-}^{96-97} \cdot \mathcal{B}_{\mu^+\mu^-}}{\mathcal{C}_{Rad}^{96-97}\mathcal{C}_s\left(1 - f_{pd}^{96-97}\right)\left(1 - f_{\psi'}^{\mu^+\mu^-}\right)}, \quad \text{(C.3)}$$

$$(N_{obs}^{DATA} - N_{QED}^{MC})_{e^+e^-}^{98-00} = \frac{\sigma_{Born}^{ep} \cdot L_{98-00} \cdot \mathcal{A}_{e^+e^-}^{98-00} \cdot \mathcal{B}_{e^+e^-}}{\mathcal{C}_{Rad}^{98-00}\left(1 - f_{pd}^{98-00}\right)\left(1 - f_{\psi'}^{e^+e^-}\right)}, \quad \text{(C.4)}$$

$$(N_{obs}^{DATA} - N_{QED}^{MC})_{\mu^+\mu^-}^{98-00} = \frac{\sigma_{Born}^{ep} \cdot L_{98-00} \cdot \mathcal{A}_{\mu^+\mu^-}^{98-00} \cdot \mathcal{B}_{\mu^+\mu^-}}{\mathcal{C}_{Rad}^{98-00}\left(1 - f_{pd}^{98-00}\right)\left(1 - f_{\psi'}^{\mu^+\mu^-}\right)}, \quad \text{(C.5)}$$

where "96-97" and "98-00" denote the data taking periods of 1996-1997 and of 1998-2000, respectively. Summing up both sides of the above equations, the formula to calculate the ep Born cross section combining all the data sets is obtained:

$$\sigma_{Born}^{ep} = \frac{N_{obs}^{DATA} - N_{QED}^{MC}}{\tilde{\boldsymbol{A}}}, \quad \text{(C.6)}$$

where $\tilde{\boldsymbol{A}}$ is the combined acceptance defined as

$$\begin{aligned}\tilde{\boldsymbol{A}} &= \frac{L_{96-97}}{\mathcal{C}_{Rad}^{96-97}\mathcal{C}_s\left(1 - f_{pd}^{96-97}\right)}\left(\frac{\mathcal{A}_{e^+e^-}^{96-97}\mathcal{B}_{e^+e^-}}{1 - f_{\psi'}^{e^+e^-}} + \frac{\mathcal{A}_{\mu^+\mu^-}^{96-97}\mathcal{B}_{\mu^+\mu^-}}{1 - f_{\psi'}^{\mu^+\mu^-}}\right) \\ &+ \frac{L_{98-00}}{\mathcal{C}_{Rad}^{98-00}\left(1 - f_{pd}^{98-00}\right)}\left(\frac{\mathcal{A}_{e^+e^-}^{98-00}\mathcal{B}_{e^+e^-}}{1 - f_{\psi'}^{e^+e^-}} + \frac{\mathcal{A}_{\mu^+\mu^-}^{98-00}\mathcal{B}_{\mu^+\mu^-}}{1 - f_{\psi'}^{\mu^+\mu^-}}\right). \quad \text{(C.7)}\end{aligned}$$

Statistical errors in the lower and upper sides, $\left(\Delta\sigma_{Born}^{ep}\right)_L^{Stat}$ and $\left(\Delta\sigma_{Born}^{ep}\right)_U^{Stat}$ respectively, are defined as

$$\left(\Delta\sigma_{Born}^{ep}\right)_L^{Stat} = \frac{\left(\Delta N_{obs}^{DATA}\right)_L^{Stat}}{\tilde{\boldsymbol{A}}} \quad \text{and} \quad \text{(C.8)}$$

$$\left(\Delta\sigma_{Born}^{ep}\right)_U^{Stat} = \frac{\left(\Delta N_{obs}^{DATA}\right)_U^{Stat}}{\tilde{\boldsymbol{A}}}, \quad \text{(C.9)}$$

where $\left(\Delta N_{obs}^{DATA}\right)_L^{Stat}$ and $\left(\Delta N_{obs}^{DATA}\right)_U^{Stat}$ indicate statistical errors, in the lower and upper sides respectively, for the number of events observed in the signal window, which is assumed to obey the Poisson distribution.

List of Figures

List of Tables